Behavior of the AB_2 Type Compounds at High Pressures and High Temperatures

Leo Merrill*

Department of Chemistry, Brigham Young University, Provo, Utah 84602

Data on the polymorphic phase transformations of known compounds and new synthetic compounds of the type AB_2 have been compiled and evaluated. All available pressure studies have been included and referenced. Pressure-temperature phase diagrams showing first order solid-solid phase boundaries and/or melting curves showing the best fit to the experimental data are included. For some materials which can be produced only by chemical synthesis techniques at high pressures and high temperatures, reaction-product diagrams have been employed to estimate the region of thermodynamic stability. Crystallographic data of all the known phases of each material have been tabulated and evaluated. This review covers 168 compounds and 332 phases including the room temperature atmospheric pressure phase for each compound when it exists.

Key words: AB_2-type compounds; calibration; critically evaluated data, crystallographic data; experimental melting curves; p, T phase diagrams; polymorphism; solid-solid phase boundaries; high pressure; high temperature.

Contents

*Present address: Christensen, Inc., Diamond Technology Center, 2532 South 3270 West, Salt Lake City, Utah 84119.

List of Tables

List of Figures

1. Introduction

This review of the behavior of the AB_2-type compounds is the third in a series of papers on the subject of material phases at high pressures and high temperatures. The two preceding papers were concerned with the pressure-temperature induced modifications and the phase diagrams for the elements [64] and AB-type compounds [172]. This paper will follow a similar format and will emphasize thermodynamic parameters of the solid-state equilibrium phase boundaries and melting curves. For most of the high pressure phases discussed within the context of this review, crystallographic data are reported. The results of the crystallographic investigations are evaluated and the numerical data are presented in table 2.

In comparing this review to the previous two it will be noted that there are fewer phase diagrams even though more compounds are discussed. The materials studied may be classified in three principal groups in regard to the preparation of the high pressure phases.

1. Materials whose kinetics are relatively rapid not allowing high pressure phases to be retained metastably at atmospheric pressure: In such compounds P, T phase boundaries are measured in situ by differential thermal analysis or by the detection of discontinuities in certain physical or transport properties such as measurement of compression or electrical resistance respectively. Crystallographic data of high pressure phases must be collected at pressure.

2. Materials whose kinetics are relatively sluggish allowing high pressure-high temperature phases produced to be retained metastably at atmospheric pressure and room temperature: High pressure phases in this category may be produced by static or dynamic pressure experiments. The crystallographic data is collected at room temperature atmospheric pressure conditions. For this type of material it is much more difficult to obtain a phase diagram. Generally, what one attempts to do is to obtain enough points on a reaction product diagram to make a reasonable evaluation of the phase diagram. The limitation is that this procedure has been carried out for very few materials. Another problem is based on the objective of the experiment. Some researchers desire only to produce the new phase and unfortunately are not concerned about its stability field. Another limitation for the reviewer is the limited number of experimental data for good intercomparison.

3. Compounds which hitherto did not exist: This type of compound especially typified by various series such as the rare earth di-antimonides RSb_2: R = Dy, Ho, Er, Tm, Lu, Y), the cubic rare earth iron Laves phases RFe_2 R = Pr, Nd, Sm, Gd, Tb, Ho, Yb, Lu), and numerous di-chalcogenide compounds. For this class of compounds which can only be synthesized at high pressure, the successful synthesis may be due to one of the following factors [15].

(a) The size ratio of the atoms might be unfavorable at 1 bar and the differential compressibilities may be such that at higher pressure the radius ratios will improve. This point of view apparently holds for the rare earth di-tellurides. This series RTe_{2-x} was known for R = La, Ce, Pr, Nd, Sm, Gd, Tb, Dy and Yb. With high pressure synthesis the added members YTe_{2-x}, $HoTe_{2-x}$, $ErTe_{2-x}$ were also synthesized. Since Te is more compressible than the RE component, the radius ratio $r(R)/r(Te)$ for the smaller rare earth elements should be comparable to that of the larger rare earth element.

(b) At atmospheric pressure the vapor pressure of one component in the system might be too high at the synthesis temperature, and very high pressure would be necessary to contain it.

(c) Pressure might alter the phase diagram such as occurs in the Ni-C system [247] making possible the synthesis of diamond in a region where diamond and Ni-liquid coexist, which is not part of the normal atmospheric pressure phase (T,x) diagram. Such phenomena are most likely to occur in P, T, x diagrams.

Since the majority of the compounds discussed in this report fall into the classification (2) and (3) above relatively few phase diagrams are possible. These data range from a single data point to fairly extensive reaction product diagrams. A few of the characteristic reaction product diagrams have been included but those with fewer than 5 data points have been omitted.

The scope of this review includes 168 AB_2-type compounds representing some 332 separate phases. A fairly complete compilation of crystallographic data for these phases has been included in Appendix A (Table 1: (Crystallographic Data for AB_2-Type Compounds)). The pressure (kbar) and temperature (°C) headings of columns 2 and 3, respectively, of the crystallographic tables refer to the pressure-temperature conditions under which the data were analyzed. The temperature and pressure at which a particular phase was prepared or its stability can be found in the text. Those phases for which either the crystal system and/or unit cell dimensions are not known are indicated by an asterisk in the particular column.

Discussions of pressure calibration can be found in previous reports by Decker et al. [91] and Merrill [172]. Table 1 contains a list of the presently accepted best values of the fixed pressure transition points for the recommended pressure calibration standards up to 80 kbar. The recommended SI unit of pressure is the pascal (newton/meter^2). Since the bar (10^5 pascal) has been used almost exclusively in the high pressure literature as the unit of pressure, the units "bar" and "kbar" have been used throughout this report. For ease in converting to GPa (giga pascal) from kbar use the following conversion: 1 GPa = 10 kbar.

TABLE 1. Pressure fixed points

Transition	Pressure (kbar) at RT	Reference
Hg(L-I)	7.57(0 °C)	172
Hg(L-I)	12.55(25 °C)	172
Bi(I-II)	25.5	172
Tl(II-III)	36.7	172
Ba(I-II)	55.3	172
Bi(III-V)	76.7	172

Table 2 CRYSTALLOGRAPHIC DATA

COMPOUND	Pressure (kbar)	Temperature (^{o}C)	Crystal System	Structure Type	a (Å)	b (Å)	c (Å)	Angle (^{o})	Z	Space Group	Density (g /cm^{3})	Ref.
Antimonides												
$LaSb_2$(I)	N	R	Orthorhombic	$LaSb_2$	6.314	6.175	18.56		8	Cmca	7.00	258
$CeSb_2$(I)	N	R	Orthorhombic	$LaSb_2$	6.295	6.124	18.21		8	Cmca	7.25	183a
$PrSb_2$(I)	N	R	Orthorhombic	$LaSb_2$	6.230	6.063	17.89		8	Cmca	7.56	96
$NdSb_2$(I)	N	R	Orthorhombic	$LaSb_2$	6.207	6.098	18.08		8	Cmca	7.53	260
$SmSb_2$(I)	N	R	Orthorhombic	$LaSb_2$	6.151	6.051	17.89		8	Cmca	7.83	260
$GdSb_2$(I)	N	R	Orthorhombic	$LaSb_2$	6.157	5.986	17.83		8	Cmca	8.10	96
$GdSb_2$(II)	N	R	Orthorhombic	$HoSb_2$	3.373	5.986	7.926		2	C222	8.52	66
$TbSb_2$(I)	N	R	Orthorhombic	$LaSb_2$	6.123	5.969	17.72		8	Cmca	8.25	96
$TbSb_2$(II)	N	R	Orthorhombic	$HoSb_2$	3.359	5.817	7.887		2	C222	8.67	66
$DySb_2$(II)	N	R	Orthorhombic	$HoSb_2$	3.350	5.802	7.862		2	C222	8.82	66
$HoSb_2$(II)	N	R	Orthorhombic	$HoSb_2$	3.343	5.790	7.842		2	C222	8.94	66
$ErSb_2$(II)	N	R	Orthorhombic	$HoSb_2$	3.337	5.780	7.820		2	C222	9.04	66

Table 2 CRYSTALLOGRAPHIC DATA (Continued)

COMPOUND	Pressure (kbar)	Temperature (°C)	Crystal System	Structure Type	a (Å)	b (Å)	c (Å)	Angle (°)	Z	Space Group	Density (g /cm^3)	Ref.
Antimonides(Cont'd)												
$TmSb_2$(II)	N	R	Orthorhombic	$HoSb_2$	3.330	5.768	7.807		2	C222	9.13	66
$LuSb_2$(II)	N	R	Orthorhombic	$HoSb_2$	3.321	5.752	7.780		2	C222	9.35	66
YSb_2(II)	N	R	Orthorhombic	$HoSb_2$	3.362	5.823	7.876		2	C222	7.16	66
Arsenides												
$CdAs_2$(I)	N	R	Tetragonal		7.96		4.67		4	$I4_122$	5.8	68
$CdAs_2$(II)			*									77
Mn_2As(I)	N	R	Tetragonal	Cu_2Sb	3.769		6.278		2	P4/mmm	6.88	93
Mn_2As(II)	N	R	Tetragonal	Fe_2P	6.363		3.678		3	P62m	7.13	126
$NiAs_2$(I)	N	R	Orthorhombic	Anomalous marcasite	4.78	5.78	3.53		2	Pnnm	7.10	273
$NiAs_2$(II)	N	R	Cubic	Pyrite	5.77				4	Pa3	7.21	179
$SiAs_2$	N	R	Cubic	Pyrite	6.023				4	Pa3	5.41	94
$ZnAs_2$(I)	N	R	Monoclinic		9.28	7.68	8.03	102.3	8	$P2_1/c$	5.1	221
$AnAs_2$(II)			*									77
Borides												
SmB_2	N	R	Hexagonal	AlB_2	3.310		4.019		1	P6/mmm	14.04	65

Table 2 CRYSTALLOGRAPHIC DATA (Continued)

COMPOUND	Pressure (kbar)	Temperature (°C)	Crystal System	Structure Type	a (Å)	b (Å)	c (Å)	Angle (°)	Z	Space Group	Density (g /cm^3)	Ref.
Carbides												
TbC_2(I)	N	R	Tetragonal	CaC_2	3.692		6.210		2	I4/mmm	7.18	149
TbC_2(II)	N	R	Orthorhombic		13.45	27.28	7.16		64		7.40	149
DyC_2(I)	N	R	Tetragonal	CaC_2	3.666		6.162		2	I4/mmm	7.48	149
DyC_2(II)	N	R	Orthorhombic		13.55	26.97	7.10		64		7.64	149
HoC_2(I)	N	R	Tetragonal	CaC_2	3.644		6.139		2	I4/mmm	7.70	149
HoC_2(II)	N	R	Orthorhombic		13.07	27.02	7.53		64		7.55	149
ErC_2(I)	N	R	Tetragonal	CaC_2	3.617		6.059		2	I4/mmm	7.96	149
ErC_2(II)	N	R	Orthorhombic		13.28	27.24	7.02		64		8.00	149
TmC_2(I)	N	R	Tetragonal	CaC_2	3.602		6.012		2	I4/mmm	8.21	149
TmC_2(II)	N	R	Orthorhombic		13.25	26.55	7.36		64		7.92	149
YbC_2(I)	N	R	Tetragonal	CaC_2	3.649		6.133		2	I4/mmm	8.01	149
YbC_2(II)			*									149
LuC_2(I)	N	R	Tetragonal	CaC_2	3.563		5.964		2	I4/mmm	8.73	149
LuC_2(II)	N	R	Orthorhombic		12.40	27.30	6.87		64		9.09	149
YC_2(I)	N	R	Tetragonal	CaC_2	3.665		6.169		2	I4/mmm	4.53	149
YC_2(II)	N	R	Orthorhombic		13.42	27.64	7.13		64		4.54	149

Table 2 CRYSTALLOGRAPHIC DATA (Continued)

COMPOUND	Pressure (kbar)	Temperature (°C)	Crystal System	Structure Type	a (Å)	b (Å)	c (Å)	Angle (°)	Z	Space Group	Density (g /cm^3)	Ref.
Halides												
BaF_2(I)	N	R	Cubic	CaF_2	6.196				4	Fm3m	4.89	95
BaF_2(II)	N	R	Orthorhombic	$\alpha PbCl_2$	4.039	6.705	7.911		4	Pbnm	5.49	89
BeF_2(I)	N	R	Hexagonal	αQuartz	4.74		5.15		3	$P3_121$	2.34	373
BeF_2(II)	N	R	Tetragonal	αCristobalite	6.60		6.74		8	$P4_12_1$	2.13	273
BeF_2(III)	N	R	Cubic	βCristobalite	7.16				8	Fd3m	1.70	273
BeF_2(IV)	N	R	Monoclinic	Coesite	6.88	11.92	6.88		16	C2/c	2.55	85
CaF_2(I)	N	R	Cubic	CaF_2	5.462				4	Fm3m	3.18	95
CaF_2(II)	N	R	Orthorhombic	$\alpha PbCl_2$	3.581	5.959	7.009		4	Pbnm	3.77	219
CdF_2(I)	N	R	Cubic	CaF_2	5.388				4	Fm3m	6.39	95
CdF_2(II)	N	R	Orthorhombic	$\alpha PbCl_2$	3.368	5.690	6.454		4	Pbnm	8.08	219
CoF_2(I)	N	R	Tetragonal	Rutile	4.54		3.32		2	$P4_2/mnm$	4.70	95
CoF_2(II)	N	R	Cubic	CaF_2	4.91				4	Fm3m	5.44	7
EuF_2(I)	N	R	Cubic	CaF_2	5.808				4	Fm3m	6.49	219
EuF_2(II)	N	R	Orthorhombic	$\alpha PbCl_2$	3.803	6.324	7.435		4	Pbnm	7.06	219
MnF_2(I)	N	R	Tetragonal	Rutile	4.873		3.310		3	$P4_2/mnm$	3.92	95
MnF_2(II)	N	R	Orthorhombic		5.03	5.03	5.28		4		4.62	132
MnF_2(III)	N	R	Orthorhombic	$\alpha PbCl_2$	3.25	5.54	6.88		4	Pbnm	4.98	132
MnF_2(IV)	N	R	Orthorhombic	αPbO_2	4.96	5.80	5.359		4	Pnab	3.99	6

Table 2 CRYSTALLOGRAPHIC DATA (Continued)

COMPOUND	Pressure (kbar)	Temperature (°C)	Crystal System	Structure Type	a (Å)	b (Å)	c (Å)	Angle (°)	Z	Space Group	Density (g /cm^3)	Ref.
Halides (Cont'd)												
MnF_2(V)	40	400	Cubic	CaF_2	5.192				4	Fm3m	4.41	133
NiF_2(I)	N	R	Tetragonal	Rutile	4.51		3.30		2	$P4_2/mnm$	4.78	78
NiF_2(II)	130-150	R	Cubic	CaF_2	4.84				4	Fm3m	5.66	7
PbF_2(I)	N	R	Cubic	CaF_2	5.939				4	Fm3m	7.77	95
PbF_2(II)	N	R	Orthorhombic	$\alpha PbCl_2$	3.899	6.442	7.651		4	Pbnm	8.48	219
SrF_2(I)	N	R	Cubic	CaF_2	5.794				4	Fm3m	4.28	95
SrF_2(II)	N	R	Orthorhombic	$\alpha PbCl_2$	3.804	6.287	7.469		4	Pbnm	4.67	219
ZnF_2(I)	N	R	Tetragonal	Rutile	4.711		3.132		2	$P4_2/mnm$	4.94	95
ZnF_2(II)	110	R	Monoclinic	ZrO_2	5.29	4.96	5.05		4		5.27	131
ZnF_2(III)	80	300	Cubic	CaF_2	4.92				4	Fm3m	5.77	131
ZnF_2(IV)	N	R	Orthorhombic	$\alpha PbCl_2$	4.683	5.658	5.166		4	Pbnm	5.01	131
$FeCl_2$(I)	N	R	Rhombohedral	CdI_2	3.598		17.536		3	$R\bar{3}m$	3.25	257
$FeCl_2$(II)	6.4	R	Rhombohedral	$FeBr_2$	3.585		5.735		1	R3m	3.30	257
$HgCl_2$(I)	N	R	Orthorhombic	$\alpha PbCl_2$	5.963	12.735	4.325		4	Pbnm	5.45	95
$HgCl_2$(II)			*		*							19
$HgCl_2$(III)	90	R	*		*							19

Table 2 CRYSTALLOGRAPHIC DATA (Continued)

COMPOUND	Pressure (kbar)	Temperature (°C)	Crystal System	Structure Type	a (Å)	b (Å)	c (Å)	Angle (°)	Z	Space Group	Density (g /cm^3)	Ref.
Halides (Cont'd)												
$HgBr_2$(I)	N	R	Orthorhombic	$HgBr_2$(C24)	6.798	12.445	4.624		4	$Bb2_1m$	6.08	95
$HgBr_2$(II)	1.7	R	*		*							19
$HgBr_2$(III)	23	R	*		*							19
$HgBr_2$(IV)	38.7	R	*		*							19
$ZnBr_2$(I)	N	R	Rhombohedral	$CdCl_2$	3.92		18.73		3	$R\bar{3}m$	4.50	95
$ZnBr_2$(II)	25	R	Tetragonal		10.83		21.66		32		4.71	171
$ZnBr_2$(III)	80	R	Hexagonal	CdI_2	3.65		5.73	1	1	$P\bar{3}m1$	5.65	171
HgI_2(I)	N	26	Tetragonal		4.39		12.38		2	$P4_2/nmc$	6.33	95
HgI_2(II)	N	130	Orthorhombic	$HgBr_2$(C24)	7.32	13.76	4.67		4	$A2_1mc$	6.41	95
HgI_2(III)	6	R	*		*							252
HgI_2(IV)	5	375	*		*							18
HgI_2(V)	75	R	Hexagonal		4.22		23.70		4	$P\bar{3}c1$	8.25	173
GeI_2(I)	N	R	Hexagonal		4.13		6.79		1	$P\bar{3}m1$	5.37	95
GeI_2(II)	20	R	*		*							52

Table 2 CRYSTALLOGRAPHIC DATA (Continued)

COMPOUND	Pressure (kbar)	Temperature (°C)	Crystal System	Structure Type	a (Å)	b (Å)	c (Å)	Angle (°)	Z	Space Group	Density (g /cm^3)	Ref.
Oxides												
AgO_2(I)	N	R	Cubic	Cuprite	4.728				2	Pn3m	7.28	95
AgO_2(II)	115	1400	Hexagonal	CdI_2	3.072		4.941		1	$C\bar{3}m$	9.53	130
CrO_2	N	R	Tetragonal	Rutile	4.419		2.915		2	$P4_2/mnm$	4.90	196
H_2O(Ih)	N	-162	Hexagonal		4.499		7.324		4	$P6_3/mmc$	0.93	138
H_2O(Ih)	N	10	Hexagonal		4.519		7.362		4	$P6_3/mmc$	0.917	138
H_2O(Ic)	N	-162	Cubic		6.35				8	Fd3m	0.93	138
H_2O(Ic)	N	-130	Cubic		6.352				8	Fd3m	0.933	138
H_2O(II)	N	-162	Rhombohedral		7.79			113.1		$R\bar{3}$	1.18	138
H_2O(II)	3	-38	Rhombohedral		7.73			113.0		$R\bar{3}$	1.18	138
H_2O(III)	2	-22	Tetragonal		6.674		6.97		12	$P4_12_12$	1.15	138
H_2O(IV)	5	-6									1.29	138
H_2O(low V)	N	-162	Monoclinic		9.22	7.54	10.35	109.2	28	A2/a	1.23	138
H_2O(high V)	5	-50	Monoclinic		9.08	7.42	10.20	109	28	A2/a	1.28	138
H_2O(low VI)	N	-162	Orthorhombic		6.27	6.27	5.79		10	Pn3m	1.37	138
H_2O(high VI)	8	-50	Tetragonal		6.17		5.70		10	$P4_2/nmc$	1.38	138
H_2O(VII)	25	25	Cubic		3.40				2	Pn3n	1.52	138
H_2O(VIII)	N	-162	Tetragonal		4.80		6.99		8	$I4_1/amd$	1.49	138
H_2O(VIII)	25	-50	Tetragonal		4.65		6.79		8	$I4_1/amd$	1.63	138
H_2O(IX)	N	-162	Tetragonal		6.73		6.83		12	$P4_12_12$	1.16	138

Table 2

CRYSTALLOGRAPHIC DATA (Continued)

COMPOUND	Pressure (kbar)	Temperature (°C)	Crystal System	Structure Type	a (Å)	b (Å)	c (Å)	Angle (°)	Z	Space Group	Density (g /cm^3)	Ref.
Oxides (Cont'd)												
GeO_2(I)	N	R	Hexagonal	αQuartz	4.972		5.698		3	$P3_121$	4.28	95
GeO_2(II)	N	R	Tetragonal	Rutile	4.395		2.850		2	$P4_2/mnm$	6.28	95
GeO_2(III)	N	R	Orthorhombic	αPbO_2					4	Pnab		215
GeO_2(IV)	N	R	Hexagonal	Fe_2N	2.729		4.312		1	P312 or P31m		
HfO_2(I)	N	R	Monoclinic		5.25	5.18	5.12	99.2	4	$P2_1/c$	10.3	95
HfO_2(II)	N	1920	Tetragonal		5.14		5.25		4	$I4_1/amd$	10.03	26
HfO_2(III)	N	R	Orthorhombic		5.056	5.006	5.224		4	$P2_12_12_1$	10.58	26
HfO_2(IV)	N	2750	Cubic	CaF_2	5.30				4	Fm3m	9.39	95
MnO_2(I)	N	R	Tetragonal	Rutile	4.386		2.856		2	$P4_2/mnm$	5.27	95
MnO_2(II)	N	R	Orthorhombic	$\alpha PbCl_2$	4.46	9.32	2.85		4	Pbnm	4.87	95
MnO_2(III)	140	R	*		*							79
MnO_2(IV)	N	R	Cubic		9.868				32		4.81	79
PbO_2(I)	N	R	Tetragonal	Rutile	4.955		3.332		2	$P4_2/mnm$	9.56	95
PbO_2(II)	N	R	Orthorhombic	αPbO_2	5.497	5.951	4.948		4	Pnab	9.81	95
PbO_2(III)	N	R	Cubic	CaF_2	5.349				4	Fm3m	10.34	249
PtO_2(I)	N	R	Hexagonal		3.08		4.19		1	P6/mmm	11.1	95
PtO_2(II)	N	R	Orthorhombic	Disordered Rutile	4.487	4.536	3.137		2	Pnn2 or Pnnm	11.8	223
RhO_2	N	R	Tetragonal	Rutile	4.486		3.088		2	$P4_2/mnm$	7.16	223

Table 2 CRYSTALLOGRAPHIC DATA (Continued)

COMPOUND	Pressure (kbar)	Temperature (°C)	Crystal System	Structure Type	a (Å)	b (Å)	c (Å)	Angle (°)	Z	Space Group	Density (g /cm^3)	Ref.
Oxides (Cont'd)												
SiO_2(I)	N	R	Rhombohedral	αQuartz	4.913		5.394		3	$P3_121$	2.65	219
SiO_2(II)	N	R	Hexagonal	βQuartz	5.01		5.47		3	$P6_222$	2.52	95
SiO_2(IIIa)	N	R	Orthorhombic	αTridymite	9.88	17.1	16.3		64		2.32	95
SiO_2(IIIb)	N	R	Hexagonal	βTridymite	5.03		8.22		4		2.21	95
SiO_2(IVa)	N	R	Tetragonal	αCristobalite	4.97		6.92		4	$P4_12_1$	2.34	219
SiO_2(IVb)	N	R	Cubic	βCristobalite	7.13				8	Fd3m	2.20	95
SiO_2(V)	N	R	Monoclinic	Coesite	7.17	7.17	12.38	120	16	C2/c	2.90	199
SiO_2(VI)	N	R	Tetragonal	Stishovite	4.179		2.665		2	$P4_2/mnm$	4.29	242
SiO_2(VII)	N	R	Tetragonal	Keatite	7.456		8.604		12	$P4_12_12$	4.39	219
SiO_2(VIII)	N	R	Orthorhombic	αPbO_2	4.30	4.70	4.50		4	Pnab	4.27	109
SiO_2(IX)	N	R	Hexagonal	Fe_2N	2.561		4.112		1	$P\bar{3}12$ or $P\bar{3}1m$	4.27	160
SnO_2(I)	N	R	Tetragonal	Rutile	4.67		3.14		2	$P4_2/mnm$	7.26	95
SnO_2(II)	N	R	Orthorhombic	αPbO_2	4.719	5.714	5.228		4	Pban	7.11	248
SnO_2(III)	250	R	Cubic	CaF_2	4.925				4	Fm3m	8.38	159
TeO_2(I)	N	R	Orthorhombic	Brookite	5.59	11.75	5.50		8	Pbca	5.83	95
TeO_2(II)	N	R	Tetragonal	Rutile	4.79		3.77		2	$P4_2/mnm$	6.09	95
TeO_2(III)	N	R	Tetragonal	Paratellurite	4.810		7.613		4	$P4_12_12$	6.01	95
TeO_2(IV)	10.1	R	Orthorhombic		4.728	4.823	7.581		4	$P2_12_12_1$	6.13	272

Table 2 CRYSTALLOGRAPHIC DATA (Continued)

COMPOUND	Pressure (kbar)	Temperature (°C)	Crystal System	Structure Type	a (Å)	b (Å)	c (Å)	Angle (°)	Z	Space Group	Density (g /cm^3)	Ref.
Oxides (Cont'd)												
TiO_2(I)	N	R	Tetragonal	Anatase	3.73		9.37		4	$I4_1/amd$	4.05	95
TiO_2(II)	N	R	Orthorhombic	Brookite	5.456	9.182	5.143		8	Pbca	4.12	95
TiO_2(III)	N	R	Tetragonal	Rutile	4.589		2.954		2	$P4_2/mnm$	4.24	95
TiO_2(IV)	N	R	Orthorhombic	αPbO_2	4.532	5.513	4.896		4	Pnab	4.34	155
TiO_2(V)	N	R	Cubic		4.455				4	Fm3m	6.14	156
TiO_2(VI)	250	R	Hexagonal		9.22		5.685		16		5.07	159
ZrO_2(I)	N	R	Monoclinic		5.164	5.255	5.297	99.2	4	$P2_1/c$	5.77	95
ZrO_2(II)	N	R	Tetragonal		5.071		5.27		4	$P4_2/nmc$	6.03	95
ZrO_2(III)	35	800	Orthorhombic		5.110	5.076	5.267		4	$P2_12_12_1$	5.99	27
ZrO_2(IV)	N	2330	Cubic		5.256				4		5.64	95
$Zn(OH)_2$(I)	N	R	Orthorhombic	C31	8.53	5.16	4.92		4	$P2_12_12_1$	3.05	95
$Zn(OH)_2$(II)	N	R	Orthorhombic		6.73	7.33	8.47		8		3.16	11
$Zn(OH)_2$(III)	N	R	Hexagonal		3.11		7.80		3		2.40	11
$Zn(OH)_2$(IV)	N	R	*		*							11
$Zn(OH)_2$(V)	N	R	Hexagonal	CdI_2	3.194		4.714		1	$C\bar{3}m$	3.96	11

Table 2 CRYSTALLOGRAPHIC DATA (Continued)

COMPOUND	Pressure (kbar)	Temperature (^{o}C)	Crystal System	Structure Type	a (Å)	b (Å)	c (Å)	Angle (^{o})	Z	Space Group	Density (g /cm^{3})	Ref.
Phosphides												
GeP_2	N	R	Cubic		5.619				4		5.04	188
$NbP_{1.70}$	N	R	Tetragonal	PbFCl	3.339		7.649		2		5.65	126a
SiP_2	N	R	Cubic	Pyrite	5.7045				4	Pa3	3.22	94
$VP_{1.75}$	N	R	Tetragonal	PbFCl	6.3237		7.2671		8	$P\bar{4}m2$	4.81	126a
ZnP_2(I)	N	R	Monoclinic		8.85	7.29	7.56	102	8	$P2_1/c$	3.55	95
ZnP_2(II)	N	R	Tetragonal		5.08		18.59		8	$P4_12_12$ or $P4_32_12$		
ZnP_2(III)	N	R	Cubic		5.322				4		3.55	189
CoP_2	N	R	Monoclinic	Arsenopyrite	5.610	5.591	5.64	116.8	4	$P2_1/c$	5.09	93

Table 2 CRYSTALLOGRAPHIC DATA (Continued)

COMPOUND	Pressure (kbar)	Temperature (°C)	Crystal System	Structure Type	a (Å)	b (Å)	c (Å)	Angle (°)	Z	Space Group	Density (g /cm^3)	Ref.
Germanides and Silicides												
$BaGe_2$(I)	N	R	Orthorhombic		9.05	6.83	11.65		8	Pnma or $Pna2_1$	5.21	102
$BaGe_2$(II)	N	R	Tetragonal	$\alpha ThSi_2$	4.755		14.73		4	$I4_1/amd$	5.63	102
$BaSi_2$(I)	N	R	Orthorhombic		8.92	6.75	11.57		8	Pnma or $Pna2_1$	3.69	95
$BaSi_2$(II)	N	R	Rhombohedral		4.047		5.330		1	$P\bar{3}m1$	4.25	100
$CaSi_2$(I)	N	R	Rhombohedral		3.855		30.6		6	$R\bar{3}m$	2.46	169
$CaSi_2$(II)	N	R	Tetragonal	$\alpha ThSi_2$	4.283		13.54		4	$I4_1/amd$	2.47	169
$EuSi_2$	N	R	Tetragonal	$\alpha ThSi_2$	4.304		13.65		4	$I4_1/amd$	5.47	101
$SrSi_2$(I)	N	R	Cubic		6.535				4		3.42	95
$SrSi_2$(II)	N	R	Tetragonal	$\alpha ThSi_2$	4.430		13.83		4	$I4_1/amd$	3.51	101

Table 2 CRYSTALLOGRAPHIC DATA (Continued)

COMPOUND	Pressure (kbar)	Temperature (°C)	Crystal System	Structure Type	a (Å)	b (Å)	c (Å)	Angle (°)	Z	Space Group	Density (g /cm^3)	Ref.
Sulfides												
Ag_2S(I)	N	R	Monoclinic	Acanthite	7.87	6.91	4.23	99.6	4	$P2_1/n$	7.25	95
Ag_2S(II)	N	189	Cubic	Argentite	4.870				2	$Im\bar{3}m$	7.12	95
Ag_2S(III)	N	600	Cubic	High Argentite	6.269				4		6.68	95
Ag_2S(IV)	20	R	*		*							76
BiS_2	N	R	*	d-values: 3.11(100), 2.97(60), 2.62(65), 1.88(70), 1.81(70), 1.504(60)								
CS_2(I)	N	-114	Orthorhombic		6.455	5.596	8.939		4	Cmca	1.566	10
CS_2(I)	N	-214	Orthorhombic		6.215	5.404	9.280		4	Cmca	1.623	10
CS_2(I)	20	R	Orthorhombic		6.16	5.38	8.53		4	Cmca	1.79	263
Cu_2S(I)	N	R	Orthorhombic		13.491	27.323	11.881		96	Ab2m	5.79	95
Cu_2S(II)	N	152	Hexagonal	Chalcocite	3.961		6.722		2	$P6_3/mmc$	5.74	95
Cu_2S(III)	N	456	Cubic		5.725				4	F . .	5.63	95
$Cu_{1.96}S$(I)	N	R	Tetragonal		3.996		11.287		4	$P4_32_12$	5.86	95
$Cu_{1.96}S$(II)	N	220	Cubic		~ 5.6							76
CuS_2	N	R	Cubic	Pyrite	5.796				4	Pa3	4.44	32

Table 2 CRYSTALLOGRAPHIC DATA (Continued)

COMPOUND	Pressure (kbar)	Temperature (°C)	Crystal System	Structure Type	a (Å)	b (Å)	c (Å)	Angle (°)	Z	Space Group	Density (g /cm^3)	Ref.
Sulfides (Cont'd)												
GeS_2(I)	N	R	Orthorhombic	C44	11.66	22.34	6.86		24	Fdd2	3.03	95
GeS_2(II)	N	R	Tetragonal		5.480		9.143		4	$I\bar{4}2d$	3.30	198
H_2S(I)	N	-120	*		*							240
H_2S(II)	N	-160	*		*							240
H_2S(III)	N	-175	*		*							240
H_2S(IV)	6	-140	*		*							240
H_2S(V)	8	-120	*		*							9
IrS_2(I)	N	R	Orthorhombic	$IrSe_2$	19.78	5.624	3.565		8	Pnam	8.59	121
IrS_2(II)	N	R	Cubic	Pyrite	5.68				4	Pa3	9.22	179
MoS_2(I)	N	R	Rhombohedral	3R	3.15		12.30		2	$P6_3/mmc$	4.98	95
MoS_2(II)	20	R	*		*							54
NbS_2(I)	N	R	Hexagonal	2H	3.31		11.89		2	$P6_3/mmc$	4.62	95
NbS_2(II)	N	R	Rhombohedral	$CdCl_2$	3.33		17.80		3	$R\bar{3}m$	4.57	95
NbS_2(III)	N	R	Hexagonal	4H-$TaSe_2$	3.33		23.8		4	$P6_3/mmc$	4.56	151
PdS_2(I)	N	R	Orthorhombic		5.54	7.53	5.46		4	Pbca	4.95	95
PdS_2(II)	N	R	Orthorhombic		5.51	7.16	5.56		4		5.16	180
SiS_2(I)	N	R	Orthorhombic		5.60	9.55	5.53		4	Ibam	2.06	95
SiS_2(II)	N	R	Tetragonal		5.420		8.718		4	$I\bar{4}2d$	2.37	198

Table 2 CRYSTALLOGRAPHIC DATA (Continued)

COMPOUND	Pressure (kbar)	Temperature (^{o}C)	Crystal System	Structure Type	a (Å)	b (Å)	c (Å)	Angle (^{o})	Z	Space Group	Density (g /cm^{3})	Ref.
Sulfides (Cont'd)												
SrS_2	N	R	Tetragonal	$CuAl_2$	6.095		7.616		4	I4/mcm	3.56	139
ZnS_2	N	R	Cubic	Pyrite	5.954				4	Pa3	5.56	33
Rare Earth Sulfides												
LaS_2(I)	N	R	Tetragonal		8.23		8.13		8	P4/nmm	4.90	31
LaS_2(II)	N	R	Cubic		8.20				8		4.90	104
CeS_2(I)	N	R	Tetragonal		8.115		8.115		8		5.08	31
CeS_2(II)	N	R	Cubic		8.12				8		5.67	105
PrS_2	N	R	Cubic		8.08				8		5.16	104
NdS_2	N	R	Cubic		8.011				8		5.38	104
GdS_2(I)	N	R	Tetragonal	LaS_2	7.796		7.196		8		6.72	107
GdS_2(II)	N	R	Cubic		7.882				8		6.96	262
TbS_2(I)	N	R	Tetragonal	LaS_2	7.754		7.864		8		6.27	262
TbS_2(II)	N	R	Cubic		7.845				8		6.14	262

Table 2

CRYSTALLOGRAPHIC DATA (Continued)

COMPOUND	Pressure (kbar)	Temperature (°C)	Crystal System	Structure Type	a (Å)	b (Å)	c (Å)	Angle (°)	Z	Space Group	Density (g /cm^3)	Ref.
Rare Earth Sulfides (Cont'd)												
DyS_2(I)	N	R	Tetragonal	LaS_2	7.696		7.861		8		6.47	104
DyS_2(II)	N	R	Cubic		7.809				8		6.32	262
YS_2(I)	N	R	Tetragonal	LaS_2	7.720		7.846		8		4.348	104
YS_2(II)	N	R	Cubic		7.797				8		4.289	262
HoS_2(I)	N	R	Tetragonal	LaS_2	7.649		7.839		8		6.645	202
HoS_2(II)	N	R	Cubic		7.784				8		6.45	262
ErS_2(I)	N	R	Tetragonal	LaS_2	7.636		7.811		8		6.75	202
ErS_2(II)	N	R	Cubic		7.745				8		6.62	262
TmS_2(I)	N	R	Tetragonal	LaS_2	7.610		7.784		8		6.86	262
TmS_2(II)	N	R	Cubic		7.745				8		6.66	262
YbS_2(I)	N	R	Tetragonal	LaS_2	7.578		7.767		8		7.06	262
YbS_2(II)	N	R	Cubic		7.722				8		6.84	262
LuS_2(I)	N	R	Tetragonal	LaS_2	7.560		7.751		8		7.17	262
LuS_2(II)	N	R	Cubic		7.687				8		6.99	262

Table 2 CRYSTALLOGRAPHIC DATA (Continued)

COMPOUND	Pressure (kbar)	Temperature (°C)	Crystal System	Structure Type	a (Å)	b (Å)	c (Å)	Angle (°)	Z	Space Group	Density (g /cm^3)	Ref.
Selenides												
Ag_2Se(I)	N	R	Orthorhombic		4.344	7.111	7.790		4	P222	8.14	82
Ag_2Se(II)	N	173	Cubic		4.993				2	Im3m	7.86	82
$BiSe_2$	N	R	*		*							229
$CdSe_2$	N	R	Cubic	Pyrite	6.615				4	Pa3	6.20	33
Cu_2Se(I)	N	R	Tetragonal		8.12		11.17		16		7.09	95
Cu_2Se(II)	N	170	Cubic	Sphalerite	5.852				4	$F\bar{4}3m$	6.83	95
Cu_2Se(III)	32	R	*		*							76
$CuSe_2$(I)	N	R	Orthorhombic	Marcasite	5.017	6.198	3.741		2	Pnnm	6.32	95
$CuSe_2$(II)	N	R	Cubic	Pyrite	6.123				4	Pa3	6.41	33
$FeSe_2$(I)	N	R	Orthorhombic	Marcasite	4.799	5.714	3.557		2	Pnnm	7.28	95
$FeSe_2$(II)	N	R	Cubic	Pyrite	5.783				4	Pa3	7.34	32
$MoSe_2$	N	R	Rhombchedral	3R	3.292		19.392		3		6.94	253
$ZnSe_2$	N	R	Cubic	Pyrite	6.615				4	Pa3	5.124	33
$NdSe_2$(I)	N	R	Hexagonal	2H	3.45		12.54		2	$P6_3/mmc$	7.75	95
$NdSe_2$(II)	N	R	Rhombchedral	3R	3.45		18.88		3	$R\bar{3}m$	7.73	95
$NdSe_2$(III)	N	R	Hexagonal	$4H_p$	3.349		25.188		4	$P6_3/mmc$	7.77	95
$NdSe_2$(IV)	N	R	Hexagonal	$4H_o$	3.46		24.8		4	$P6_3/mmc$	7.80	98

Table 2 CRYSTALLOGRAPHIC DATA (Continued)

COMPOUND	Pressure (kbar)	Temperature (°C)	Crystal System	Structure Type	a (Å)	b (Å)	c (Å)	Angle (°)	Z	Space Group	Density (g /cm^3)	Ref.
Selenides (Cont'd)												
$SmSe_2$	N	R	Tetragonal	$LaTe_2$	4.110		8.275		2	P4/nmm	7.32	13
$TmSe_2$	N	R	Tetragonal	$LaTe_2$	3.961		8.188		2	P4/nmm	8.45	261
$YbSe_2$	N	R	Tetragonal	$LaTe_2$	3.970		8.151		2	P4/nmm	8.56	261
$LuSe_2$	N	R	Tetragonal	$LaTe_2$	3.939		8.147		2	P4/nmm	8.86	261
Tellurides												
Ag_2Te(I)	N	R	Monoclinic		8.13	4.48	8.09	112.9	4	$P2_1/n$	8.40	14
Ag_2Te(II)	N	155	Cubic	Disordered(fcc)	6.64				4	F. .	7.79	95
Ag_2Te(III)	24	R	Tetragonal		8.92		6.09		8		9.41	14
Ag_2Te(IV)	40	R	Tetragonal		8.68		6.09		8		9.91	14
Ag_2Te(V)	30	300	*		*							14
Ag_2Te(VI)	N	825	Cubic		5.29				2	I. .	7.70	95
$AuTe_2$(I)	N	R	Monoclinic	Calaverite	7.18	4.40	5.07	90.0	2	C2/m	9.38	273
$AuTe_2$(II)	N	R	Orthorhombic	Krennerite	16.51	8.80	4.45		8	Pma	9.29	273
$AuTe_2$(III)	20	R	Tetragonal	Two possible unit cells	5.25 6.13		5.48 3.72		2 2		9.94 10.74	2 2
$CuTe_2$	N	R	Cubic	Pyrite	6.60				4	Pa3	7.36	34

Table 2 CRYSTALLOGRAPHIC DATA (Continued)

COMPOUND	Pressure (kbar)	Temperature (°C)	Crystal System	Structure Type	a (Å)	b (Å)	c (Å)	Angle (°)	Z	Space Group	Density (g /cm^3)	Ref.
Tellurides (Cont'd)												
$CoTe_2$(I)	N	R	Orthorhombic	Marcasite	5.319	6.319	3.897		2	Pnnm	7.96	95
$CoTe_2$(II)	N	R	Hexagonal	CdI_2	3.784		5.403		1	$P\bar{3}m1$	7.74	95
$CoTe_2$(III)	N	R	Cubic	6.310					4	Pa3	8.31	32
$FeTe_2$(I)	N	R	Orthorhombic	Marcasite	5.340	6.26	3.849		2	Pnnm	7.98	95
$FeTe_2$(II)	N	R	Cubic	Pyrite	6.292				4	Pa3	8.29	32
$NiTe_2$(I)	N	R	Hexagonal	CdI_2	3.385		5.255		2	$P\bar{3}m1$	7.73	95
$NiTe_2$(II)	N	R	Cubic	Pyrite	6.374				4	Pa3	8.05	34
Rare Earth Tellurides												
YTe_{2-x}	N	R	Tetragonal	Cu_2Sb	4.291		8.912		2	P4/nmm	6.96	60
											(6.19)[a]	
$HoTe_{2-x}$	N	R	Tetragonal	Cu_2Sb	4.264		8.872		2	P4/nmm	8.65	60
											(7.86)[a]	
$ErTe_{2-x}$	N	R	Tetragonal	Cu_2Sb	4.248		8.865		2	P4/nmm	8.77	60
											(7.98)[a]	60
$TmTe_{2-x}$	N	R	Tetragonal	Cu_2Sb	4.240		8.831		2	P4/nnm	8.87	60
											(8.07)[a]	60
$LuTe_{2-x}$	N	R	Tetragonal	Cu_2Sb	4.322		8.807		2	P4/nnm	9.10	60
											(8.29)[a]	60

( )[a] - calculated for x = 0.3

Table 2 CRYSTALLOGRAPHIC DATA (Continued)

COMPOUND	Pressure (kbar)	Temperature (°C)	Crystal System	Structure Type	a (Å)	b (Å)	c (Å)	Angle (°)	Z	Space Group	Density (g /cm^3)	Ref.
Mixed Cation Transition Metal Chalcogenides												
$Cd_{0.04}Cu_{0.96}S_2$	N	R	Cubic	Pyrite	5.089				4	Pa3	4.24	34
$Cd_{0.35}Mn_{0.65}S_2$	N	R	Cubic	Pyrite	6.055				4	Pa3	4.16	34
$Cr_{0.39}Co_{0.61}S_2$	N	R	Cubic	Pyrite	5.558				4	Pa3	4.66	92a
$Cu_{0.76}Fe_{0.24}S_2$	N	R	Cubic	Pyrite	5.702				4	Pa3	4.51	34
$Mn_{0.25}Cu_{0.75}S_2$	N	R	Cubic	Pyrite	5.869				4	Pa3	4.12	34
$Ni_{0.50}Fe_{0.50}S_2$	N	R	Cubic	Pyrite	5.545				4	Pa3	4.69	34
$Zn_{0.50}Cd_{0.50}S_2$	N	R	Cubic	Pyrite	6.125				4	Pa3	4.42	34
$Zn_{0.20}Cu_{0.80}S_2$	N	R	Cubic	Pyrite	5.825				4	Pa3	4.62	34
$Zn_{0.35}Mn_{0.65}S_2$	N	R	Cubic	Pyrite	6.055				4	Pa3	4.16	34
$Cd_{0.06}Cu_{0.94}Se_2$	N	R	Cubic	Pyrite	6.146				4	Pa3	6.42	34
$Cd_{0.48}Mn_{0.52}Se_2$	N	R	Cubic	Pyrite	6.511				4	Pa3	5.71	34

Table 2 CRYSTALLOGRAPHIC DATA (Continued)

COMPOUND	Pressure (kbar)	Temperature (°C)	Crystal System	Structure Type	a (Å)	b (Å)	c (Å)	Angle (°)	Z	Space Group	Density (g /cm^3)	Ref.
Mixed Cation Transition Metal Chalcogenides (Cont'd)												
$Mn_{0.56}Cu_{0.44}Se_2$	N	R	Cubic	Pyrite	6.293				4	Pa3	5.77	34
$Ni_{0.60}Fe_{0.40}Se_2$	N	R	Cubic	Pyrite	5.890				4	Pa3	7.01	34
$Zn_{0.32}Cd_{0.68}Se_2$	N	R	Cubic	Pyrite	6.510				4	Pa3	6.15	34
$Zn_{0.40}Cu_{0.60}Se_2$	N	R	Cubic	Pyrite	6.186				4	Pa3	6.23	34
$Zn_{0.50}Mn_{0.50}Se_2$	N	R	Cubic	Pyrite	6.360				4	Pa3	5.63	34
$Mn_{0.67}Cu_{0.33}Te_2$	N	R	Cubic	Pyrite	6.838				4	Pa3	6.50	34
$Zn_{0.50}Mn_{0.50}Te_2$	N	R	Cubic	Pyrite	6.874				4	Pa3	6.45	34

Table 2 CRYSTALLOGRAPHIC DATA (Continued)

COMPOUND	Pressure (kbar)	Temperature (°C)	Crystal System	Structure Type	a (Å)	b (Å)	c (Å)	Angle (°)	Z	Space Group	Density (g /cm^3)	Ref.
Alloy and Intermetallic Compounds												
$AuAl_2$	N	R	Cubic	CaF_2	6.00				4	Fm3m	7.12	95
$AuGa_2$	N	R	Cubic	CaF_2	6.075				4	Fm3m	9.97	95
$AuIn_2$(I)	N	R	Cubic	CaF_2	6.515				4	Fm3m	10.25	95
$AuIn_2$(II)	N	R	*		*							211
$LaCo_2$	N	R	Cubic	$MgCu_2$	7.449				8	Fd3m	8.25	204
$LaOs_2$(I)	N	R	Cubic	$MgCu_2$	7.743				8	Fd3m	14.86	63
$LaOs_2$(II)	N	R	Hexagonal	$MgZn_2$	5.419		9.083		4	$P6_3/mmc$	14.92	63
$CeOs_2$(I)	N	R	Cubic	$MgCu_2$	7.593				8	Fd3m	15.80	63
$CeOs_2$(II)	N	R	Hexagonal	$MgZn_2$	5.355		8.816		4	$P6_3/mmc$	15.78	63
$SmRu_2$(I)	N	R	Cubic	$MgCu_2$	7.577				8	Fd3m	10.81	62
$SmRu_2$(II)	N	R	Hexagonal	$MgAn_2$	5.298		8.939		4	$P6_3/mmc$	10.81	62
$NdRu_2$(I)	N	R	Cubic	$MgCu_2$	7.612				8	Fd3m	10.47	62
$NdRu_2$(II)	N	R	Hexagonal	$MgZn_2$	5.323		9.004		4	$P6_3/mmc$	10.44	62
$MnAu_2$(I)	N	R	Tetragonal	CaC_2	3.363		8.592		2	I4/mmm	15.33	95
$MnAu_2$(II)	N	R	Tetragonal		*							62

Table 2

CRYSTALLOGRAPHIC DATA (Continued)

COMPOUND	Pressure (kbar)	Temperature (°C)	Crystal System	Structure Type	a (Å)	b (Å)	c (Å)	Angle (°)	Z	Space Group	Density (g /cm^3)	Ref.
Iron Compounds												
$PrFe_2$	N	R	Cubic	$MgCu_2$	7.467				8	Fd3m	8.06	61
$NdFe_2$	N	R	Cubic	$MgCu_2$	7.452				8	Fd3m	8.21	61
$SmFe_2$	N	R	Cubic	$MgCu_2$	7.415				8	Fd3m	8.54	61
$GdFe_2$	N	R	Cubic	$MgCu_2$	7.394				8	Fd3m	8.84	61
$TbFe_2$	N	R	Cubic	$MgCu_2$	7.354				8	Fd3m	9.07	61
$HoFe_2$	N	R	Cubic	$MgCu_2$	7.303				8	Fd3m	9.43	61
$YbFe_2$	N	R	Cubic	$MgCu_2$	7.239				8	Fd3m	9.97	61
$LuFe_2$	N	R	Cubic	$MgCu_2$	7.229				8	Fd3m	10.08	61
Magnesium Compounds												
Mg_2Si(I)	N	R	Cubic	CaF_2	6.404				4	Fm3m	1.94	95
Mg_2Si(II)	N	R	Orthorhombic	Ni_2Si	4.48	5.94	8.22		4	Pmnb	2.34	219
Mg_2Ge(I)	N	R	Cubic	CaF_2	6.378				4	Fm3m	3.10	95
Mg_2Ge(II)	N	R	Orthorhombic	Ni_2Si	4.57	5.96	8.50		4	Pmnb	3.47	219

Table 2 CRYSTALLOGRAPHIC DATA (Continued)

COMPOUND	Pressure (kbar)	Temperature (°C)	Crystal System	Structure Type	a (Å)	b (Å)	c (Å)	Angle (°)	Z	Space Group	Density (g /cm^3)	Ref.
Magnesium Compounds (Cont'd)												
Mg_2Sn(I)	N	R	Cubic	CaF_2	6.765				4	Fm3m	3.60	95
Mg_2Sn(II)	N	R	Orthorhombic	Ni_2Si	4.82	6.25	9.14		4	Pmnb	4.03	219
Manganese Compounds												
$SmMn_2$(I)	N	R	Cubic	$MgCu_2$	7.79				8	Fd3m	7.31	153a
$SmMn_2$(II)	N	R	Hexagonal	$MgZn_2$	5.501		8.968		4	$P6_3/mmc$	7.35	97a
$GdMn_2$(I)	N	R	Cubic	$MgCu_2$	7.724				8	Fd3m	7.70	264a
$GdMn_2$(II)	N	R	Hexagonal	$MgZn_2$	5.447		8.893		4	$P6_3/mmc$	7.76	97a
$TbMn_2$(I)	N	R	Cubic	$MgCu_2$	7.620				8	Fd3m	8.07	264a
$TbMn_2$(II)	N	R	Hexagonal	$MgZn_2$	5.390		8.786		4	$P6_3/mmc$	8.07	97a
$DyMn_2$(I)	N	R	Cubic	$MgCu_2$	7.573				8	Fd3m	8.33	264a
$DyMn_2$(II)	N	R	Hexagonal	$MgZn_2$	5.356		8.744		4	$P6_3/mmc$	8.32	97a
$HoMn_2$(I)	N	R	Cubic	$MgCu_2$	7.507				8	Fd3m	8.63	264a
$HoMn_2$(II)	N	R	Hexagonal	$MgZn_2$	5.316		8.672		4	$P6_3/mmc$	8.59	97a
$YBMn_2$	N	R	Hexagonal	$MgZn_2$	5.233		8.561		4	$P6_3/mmc$	9.25	97a
YMn_2(I)	N	R	Cubic	$MgCu_2$	7.678				8	Fd3m	5.83	95
YMn_2(II)	N	R	Hexagonal	$MgZn_2$	5.404		8.848		4	$P6_3/mmc$	5.87	97a

2. Antimonides

In a series of rare earth compounds RX_2 where the rare earth element R is varied, it is common to find that compounds can be prepared for only a certain range of the elements of the rare earth series. Prior to synthesis studies conducted at high pressure, for example, rare earth diantimonides were known for the lighter rare earths. The first rare earth diantomonide discovered was $LaSb_2$ by Vogel and Klose [258]. In 1966, Olcese [183a] reported $CeSb_2$ and in 1967 $YbSb_2$, $NdSb_2$, and $SmSb_2$ were reported by Wang and Steinfink [260] Wang and Steinfink [260] attempted the synthesis of the antimonides of Gd, Dy, Ho, and Er but were unsuccessful. By single crsytal x-ray diffraction techniques $LaSb_2$, $CeSb_2$, $NdSb_2$, and $SmSb_2$ were found to have an orthorhombic structure [26] designated the $LaSb_2$-type. In this structure it was found that the SB-Sb bond distance was short, suggesting that beyond a certain limit the structure would become unstable.

High pressure high temperature synthesis studies by Eatough and Hall [96] have extended the $LaSb_2$-type structure to include $PrSb_2$, $GdSb_2$ and $TbSb_2$. The synthesis of these diantimonides takes place at approximately 35 kbar and 1200 °C to 1500 °C. A new high pressure phase referred to as the $HoSb_2$-type was discovered by Eatough and Hall [96] which extends the diantimonide series to include the heavier rare earth elements. Synthesis of the $HoSb_2$-type rare earth diantimonide has been reported for $GdSb_2$, $TbSb_2$, $DySb_2$, $HoSb_2$, $TmSb_2$, $LuSb_2$ and YSb_2. The range of pressure and temperature for the synthesis of this series is 40–60

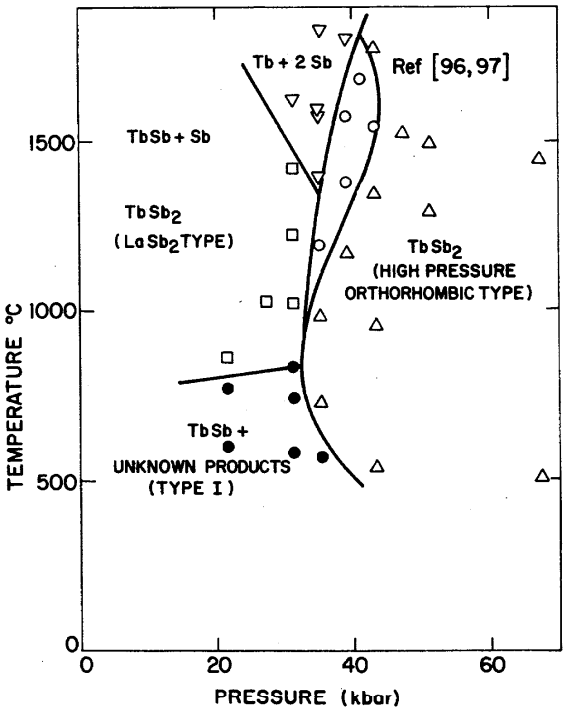

FIGURE 2. Reaction product diagram for Tb + 2Sb.

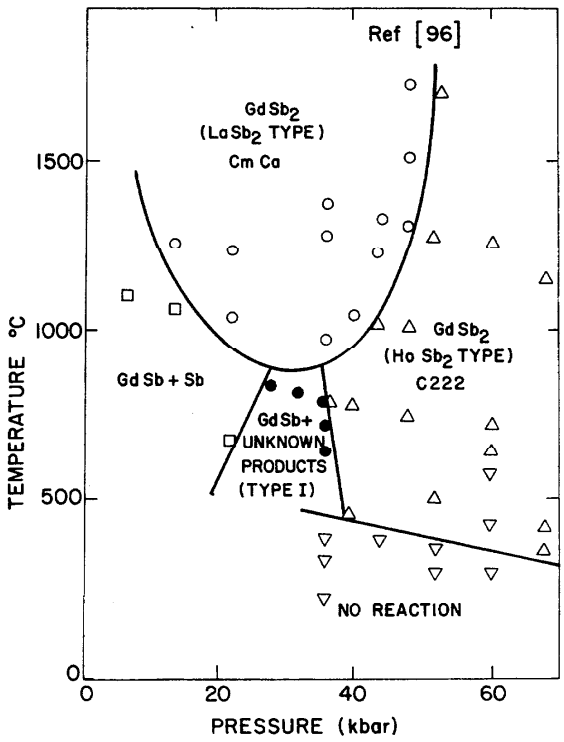

FIGURE 1. Reaction product diagram for Gd + 2Sb.

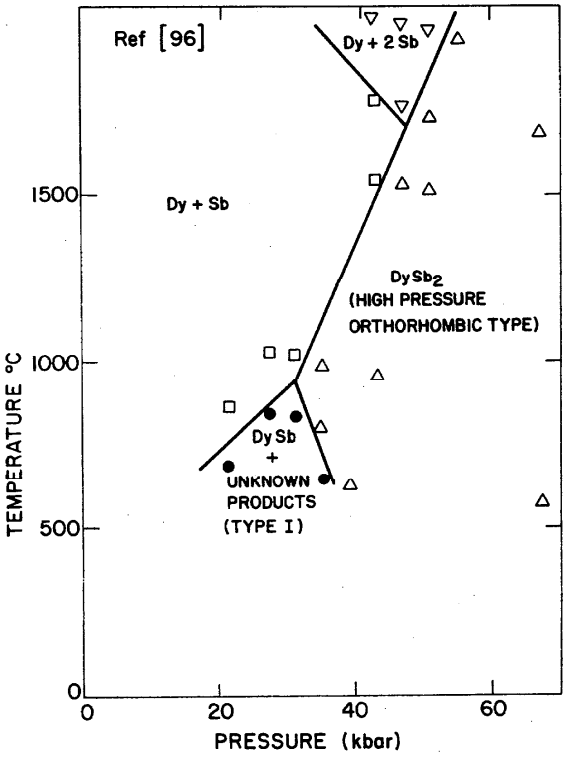

FIGURE 3. Reaction product diagram for Dy + 2Sb.

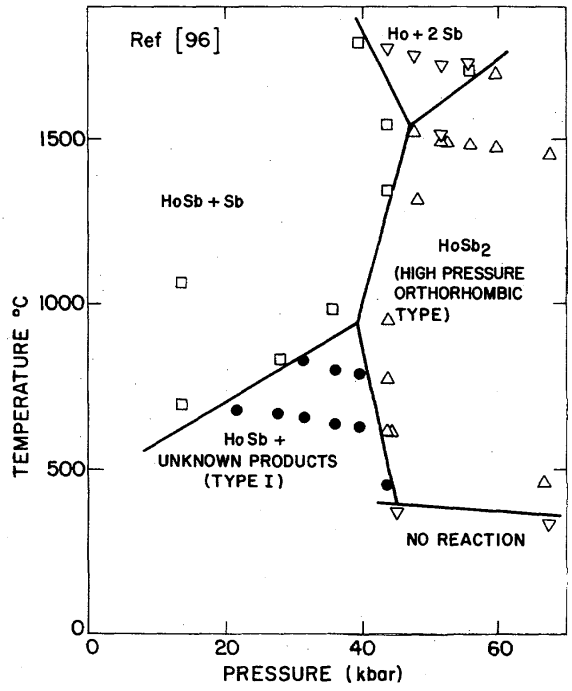

FIGURE 4. Reaction product diagram for Ho + 2Sb.

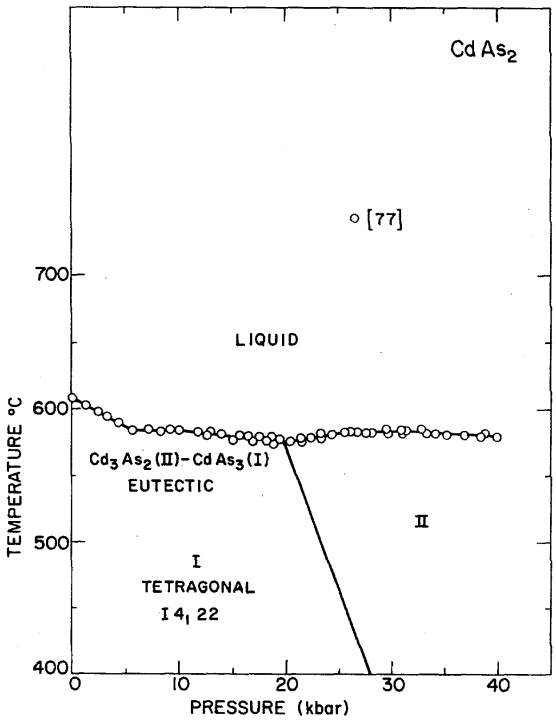

FIGURE 5. Phase diagram for $CdAs_2$.

kbar and 500–1500 °C. The approximate stability fields of these phases are shown in figures 1 through 4. The crystallographic data on the $HoSb_2$-type structure is based on powder diffraction studies. Eatough and Hall [96] indexed it as orthorhombic and Johnson [127] proposed the structure whose space group is C222.

The $HoSb_2$-type structure ($Z = 2$) is made up of hexagonal layers of Ho and Sb atoms with a layer stacking sequence Ho-Sb(1)-Sb(2). These layers are stacked in such a way that the expected hexagonal symmetry is reduced to orthorhombic (pseudohexagonal). The Sb atoms of one layer are lined up over the midpoint of the lines connecting the hexagonal array of Ho atoms in an adjacent layer. If the Sb atoms were situated over the center of alternate triangles of Ho, the CdI_2-type structure would be obtained. The $HoSb_2$-type structure results in a 10 percent increase in Sb-Sb bond length over the $LaSb_2$-type structure but a 20 percent decrease in R-R bond length.

The crystallographic unit cell dimensions of the high pressure $HoSb_2$-type compounds prepared by Eatough and Hall [96,97] have been recalculated by Cannon [66] using the structure proposed by Johnson [108] and the original x-ray data of Eatough and Hall [96,97]. The calculations of Cannon [66] confirm that Johnson's $HoSb_2$-type structure fits the experimental data much better than that proposed by Eatough and Hall [96,97] and is probably correct.

3. Arsenides

3.1. $CdAs_2$

The $CdAs_2$ phase diagram (fig. 5) has been investigated by Clark and Pistorius [77]. $CdAs_2$ was prepared by direct synthesis of stoichiometric quantities of the elements in evacuated quartz ampoules which were heated to 850 °C and cooled slowly. Measurements of the resistance (four wire method) of a sliver of $CdAs_2$ as a function of pressure in a Bridgman anvil device reveal a phase transition at approximately 60 kbar at 25 °C. The resistance dropped by a factor of 30 in separate experiments. At higher temperatures the transition was observed by means of DTA (using Chromel-Alumel thermocouples) at constant temperature while the pressure was cycled through the transition. The $CdAs_2$(I)-$CdAs_2$(II) phase boundary has an approximate slope of -10 K/kbar. It intersects the melting curve at 19.8 kbar and 579.5 °C.

The melting curve of $CdAs_2$ was studied to 45 kbar. The melting of $CdAs_2$(I) yielded sharp and strong DTA signals. The melting curve drops with pressure with an initial slope of -1.6 K/kbar from 621 °C at atmospheric pressure to the triple point at 19.8 kbar and 579.5 °C. Melting of the denser $CdAs_2$(II) phase initially rises with pressure with a slope of 1.8 K/kbar, passes through a broad maximum at ~30 kbar and 591.5 °C and then falls with increasing pressure. Upon decreasing pressure the $CdAs_2$(II) melting curve could be followed to ~5 kbar below the triple point. No metastable extension of the $CdAs_2$(I) melting curve could be observed on the up cycle.

The DTA signals of the$CdAs_2$(I) melting curve exhibit interesting metastable behavior on the decreasing temperature cycle. The phase boundary initially drops with pressure from 610 °C at atmospheric pressure to 589.5 °C, at 5.9 kbar, where the slope of the curve sharply changes from -4.2 K/kbar to 10.4 K/kbar. The initial part of the curve is attribut-

ed to the Cd_3As_2-$CdAs_2$ eutectic at 610 °C at atmospheric pressure (56 at. percent As). The abrupt change in the slope at 589.5 °C and 8.4 kbar is due to the $CdAs_2$(I)-As eutectic.

Each phase boundary in this work was based on several separate runs. For melting curve determinations, the results are believed to be within ± 0.5 kbar and ± 0.5 K. In the determinations of the $CdAs_2$(I)-$CdAs_2$(II) boundary the accuracy of the pressures are estimated to be within ± 2 kbar. Experimental corrections described by Pistorius and Clark (194) and Richter and Pistorius [201] have been applied.

$CdAs_2$(I) is tetragonal, space group $I4_122 - D_{10}^4$ with Cd atoms in 4(b) positions and As atoms in 8(f) positions. The structure of $CdAs_2$(II) has not been determined.

3.2. Mn_2As

Both Cr_2As and Mn_2As have been prepared at atmospheric pressure with the Cu_2Sb-type structure. In addition, Cr_2As was synthesized with the Fe-P-type structure by quenching from high temperature. The Fe_2P-type phase of Mn_2As could not be prepared in this manner but was synthesized from samples subjected to simultaneous high temperature and high pressure [126].

The Cu_2Sb-type of Mn_2As was prepared by slowly heating stoichiometric mixtures of the elements to 700 °C in evacuated silica tubes. The samples were afterwards held at 1100 °C for a few hours and then quenched in water. The Fe_2P-type modification of Mn_2As formed at a temperature of 1200 °C and pressure of 65 kbar held for 2 hours. The product was allowed to cool to 1100 °C and quenched to room temperature under pressure.

The crystallography of Fe_2P-type Mn_2As was determined by standard single crystal techniques. The hexagonal unit cell dimensions are $a = 6.363$ Å, $c = 3.678$ Å, $z = 3$ and $\rho_c = 7.13$ g/cm^3. The space group in $P\bar{6}2m$. Mn_2As(II) is antiferromagnetic with a Neel temperature of 50 ± 10 K.

3.3. $NiAs_2$

The pyrite-type crystal structure is exhibited by a wide variety of compounds, many of which are of interest because of their varied electrical and magnetic properties. The pyrite structure (space group Pa3) is in general a densely packed arrangement and therefore tends to be formed when synthesis is attempted between the transition metals and groups Va or VIa elements at high pressure.

Nickel diarsenide crystallizes in an anomalous marcasite structure which differs from the normal marcasite by small angular distortions about the cation octahedra. Since the marcasite structure has a less dense packing arrangement, a transformation to the pyrite structure should be induced by the action of high pressure.

The pyrite phase of $NiAs_2$ was prepared by Munson [179] from the reaction of a mixture of powdered Ni and As in a 1:1.22 mole ratio. The sample in the high pressure chamber was held at a temperature of 1400 °C and a pressure of 65 kbar of a period of one half hour. The presence of the pyrite-type $NiAs_2$ was confirmed by powder x-ray examination. Cubic $NiAs_2$ is gray with unit cell dimension $a = 5.77$ Å and densities $\rho_e = 7.15$ g/cm^3 and $\rho_c = 7.21$ g/cm^3.

3.4. $SiAs_2$

Silicon diarsenide has been synthesized with the pyrite-type crystal structure, space group Pa3. This is the only known phase of $SiAs_2$ and requires elevated pressure for its preparation. Successful syntheses were carried out [94] from 45 and 65 kbar at 1300 °C with reaction times of one hour, then cooled slowly to 1100 °C at the rate 50 °C/h quenched. The crystal structure and space group of $SiAs_2$ were verified by single crystal techniques.

Silicon atoms are located in special positions 4(a), while arsenic atoms occupy eightfold position 8(c) for which $x = 0.384$. The unit cell data are $a = 6.023$ Å, $z = 4$, and $\rho_c = 5.41$ g/cm^3. $SiAs_2$, along with SiP_2, $GeAs_2$, GeP_2, unusual due to the fact that they are the only examples of pyrite type compounds of nonmetallic elements. They are also unusual in that silicon is octahedrally coordinated. The unit cell dimension of $PtAs_2$ and $PdAs_2$ ($a = 5.965$ Å and 5.985 Å, respectively) are very close to that of $SiAs_2$ and the bond distances of $SiAs_2$ are within experimental error equal to their counterparts in $PtAs_2$ and $PdAs_2$.

3.5. $ZnAs_2$

The phase diagram of $ZnAs_2$ has been studied by Clark and Pistorius [77] in a piston-cylinder device by means of differential thermal analysis using chromel-alumel thermocouples. The $ZnAs_2$ samples were prepared by direct synthesis of stoichiometric quantities of the elements.

The melting curve of $ZnAs_2$(I) is nearly linear with a slope of -4.7 K/kbar and terminates at the triple point which is located at 19 kbar, 679 °C. The melting curve of

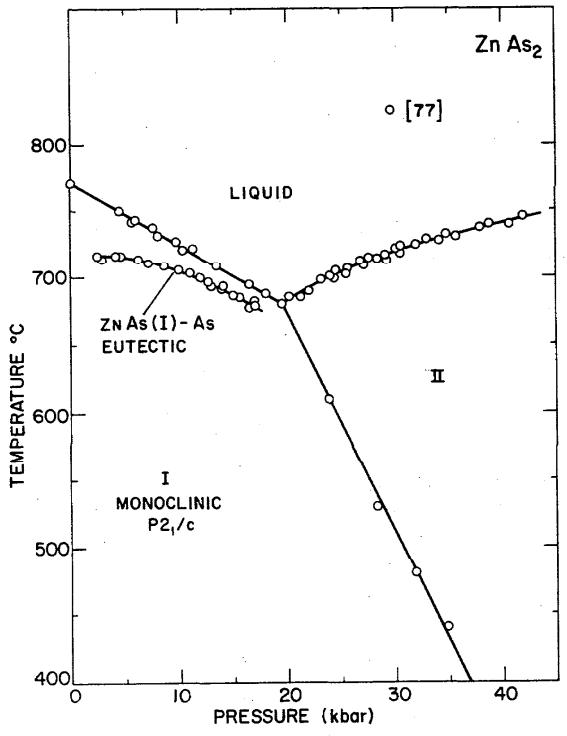

FIGURE 6. Phase diagram for $ZnAs_2$.

$ZnAs_2$(II) rises with pressure with an initial slope of + 4.0 K/kbar and considerable curvature. The $ZnAs_2$(II) melting curve was determined up to 45 kbar. The experimental uncertainties of the melting point determinations are estimated to be ± 0.5 kbar and ± 0.5 K. (fig. 6).

Resistance measurements in a Bridgman anvil device at 25 °C showed no polymorphic transitions up to an estimated pressure of 110 kbar. At higher temperatures the $ZnAs_2$(I)-$ZnAs_2$(II) phase boundary was observed by means of DTA at constant temperature while the pressure was cycled across the transition. Using this technique the phase boundary was traced from the triple point (679 °C) down to 450 °C. A linear extrapolation of this phase boundary intersects the room temperature pressure axis at approximately 70 kbar. The failure to detect the transition by electrical resistance methods may be due to poor kinetics associated with this transition at room temperature.

Along the $ZnAs_2$(I) melting curve metastable behavior is observed not identical to that noted in $CdAs_2$(I). The metastable phase boundary is due to the $ZnAs_2$(I)-As eutectic. No $ZnAs_2$(II)-As eutectic was observed at pressures above the triple point. However, signals due to the $ZnAs_2$(I)-As reappeared upon lowering the pressure past the triple point.

$ZnAs_2$(I) is primitive monoclinic, space group $P2_1/c$ (C_{2h}^5). The structure of $ZnAs_2$(II) has not been determined.

4. Borides

4.1. SmB_2

Rare earth borides of the composition RB_2 have been prepared at atmospheric pressure for all the heavier rare earth members from gadolinium through lutetium including yttrium and scandium. These diborides are isomorphous and have the AlB_2-type structure (C32). This structure is hexagonal (P6/mmm) and consists of alternating layers of metal and boron atoms. Previous attempts to synthesize the diborides with rare earth component larger than gadolinium have been unsuccessful. Cannon et al. [65] suggested that since the compressibilities of the lanthanides are greater than that of boron, then pressure would tend to make the lanthanides behave like the smaller ones.

Of the seven lanthanid elements which are larger than gadolinium, simultaneous high pressure-high temperature conditions were successful in synthesizing one new diboride phase, SmB_2. SmB_2 was prepared from a stoichiometric ratio of the elements reacted at 65 kbar and 1140–1240 °C for 75 minutes. The AlB_2-type cell of SmB_2 has the dimensions $a = 3.310$ Å and $c = 4.019$ Å. Intensity data from the powder x-ray diffraction patterns indicate that the samarium atom in SmB_2 is flattened in the c-crystallographic direction.

5. Carbides

The heavy rare earth dicarbides have been shown to exist in both cubic and hexagonal modifications and have been studied extensively [46,237,238]. In LuC_2 a transformation was observed to proceed from cubic to a low order symmetry which was tentatively identified as tetragonal with an unusually large unit cell. High pressure studies of the lanthanum dicarbides were carried out in an attempt to synthesize this lattice type. The normal stable modification of the lanthanum dicarbides of (Tb, Dy, Ho, Er, Tm, Yb, Lu, Y:C_2) is body centered tetragonal CaC_2-type, space group I4/mmm.

Dicarbides of the rare earth metals were prepared by arc melting the elements together in a helium atmosphere. Synthesis of the possible high pressure phases were carried out the in the pressure range 15–34 kbar and temperature range 850 and 1200 °C and time intervals of 5 to 30 minutes [176a]. While all of the dicarbides listed above could be made successfully by high pressure techniques, three of them, LuC_2, YbC_2 and TmC_2 were prepared by high temperature annealing techniques. Th powder diffraction patterns of the high pressure phase were complex containing very many lines. The data were fit to the orthorhombic crystal system with a large unit cell size ($Z = 64$). There is no sequential trend of the density with increasing atomic number of the rare earth metal which casts some doubt on the orthorhombic crystal system.

6. Germanides

6.1. $BaGe_2$

At atmospheric pressure $BaGe_2$ crystallizes in an orthorhombic Pnma (or $Pna2_1$) structure made of isolated Ge_4 tetrahedra. At a pressure of 40 kbar and temperature of 1000 °C $BaGe_2$(I) transforms to a tetragonal modification of the α-$ThSi_2$-type which can be retained metastably at atmospheric pressure [102]. $BaGe_2$(II) is isomorphous with the high pressure phase of $CaSi_2$ and $SrSi_2$, while the high pressure form of $BaSi_2$ is rhombohedral (space group P3ml). In the presence of air and moisture $BaGe_3$(II) decomposes and when heated to 350 °C it reverts to the atmospheric pressure form. The decrease in volume in the $GaGe_2$-$BaGe_2$(II) transition amounts to 8 percent. The tetragonal unit cell dimensions of $BaGe_2$(II) are $a = 4.755$ Å, $c = 14.73$ Å with $Z = 4$ and $\rho_c = 5.63$ g/cm^3.

In the $BaSi_2$(I)-$BaSi_2$(II) transformation the isolated Si_4 tetrahedra change so as to appear to lie in wavy Si-layers. Actually the Si_4 tetrahedra in $BaSi_2$(II) may be described as corner shared in a two dimensional array involving only the silicon atoms in the basal plane of the tetrahedra. In contrast to $BaSi_2$(II) the Si-layers in $BaGe_2$(II) are made up to planar Si_4 groups in which the adjacent layers are rotated by 90°. The coordination polyhedra in $BaSi_2$(II) (rhombohedral) and $BaGe_2$(II) (tetragonal) are very similar. The number of nearest neighbors in each in 9 (6 barium and 3 silicon or germanium, respectively).

7. Metal Halides

7.1. BaF_2

Under the influence of pressure the fluorite phase of BaF_2 transforms irreversibly to the α-$PbCl_2$-type structure. The transformation was accomplished at 400 °C and 30 kbar [212]. No further transitions were observed up to 150 kbar. The evidence for the α-$PbCl_2$ phase is based upon 1 bar x-ray data. In an investigation of pressure-induced color centers in BaF_2, Minomura and Drickamer [174] observed that the light was cut off in a 5 kbar range near 30 kbar. This was

interpreted to be due to the occurrence of a polymorphic phase transitions. Samara [212] measured the capacitance of BaF_2 up to 30 kbar and detected a sharp discontinuity at 26.8 kbar in a liquid pressure medium. There is a significant hysteresis associated with this transition. For example, it has the value of 18 kbar at 22 °C and 12.5 kbar at 150 °C. The average slope dP/dT is 2.6×10^{-2} kbar/K.

The transition is BaF_2 is from the cubic-fluorite structure to the orthorhombic α-$PbCl_2$ phase. Both phases contain four molecules per unit cell. In the α-$PbCl_2$ structure, each Ba has nine fluorine neighbors, but the distances are not all equal. The volume change at the transition is about 11 percent. The orthorhombic unit cell data is $a = 4.035$ Å, $b = 6.676$ Å, $c = 7.879$ Å and $Z = 4$.

In the work of Dandekar and Jamieson [89] the α-$PbCl_2$ phase formed from the simultaneous action of pressure and temperature was retained at 1 bar. The experiments of Samara [212] from room temperature up to 150 °C indicate the transition is readily reversible.

7.2. BeF_2

The normal phase of BeF_2 which is isomorphous with quartz, transforms to a new modification having the coesite-type structure at a pressure of 22 kbar and a temperature of 450 °C [85].

7.3. CaF_2

The high pressure transformation of CaF_2 from the cubic fluorite structure to the α-$PbCl_2$-type structure has been reported by Seifert [186] and German et al. [94a]. Seifert [186] reported the CaF_2(I)-CaF_2(II) transformation in the region above 100 kbar in a piston-anvil apparatus while German et al. [94a] employing shock techniques reported a pressure of 100 kbar at − 150 °C. This transformation represents an increase in coordination number from eight to nine and an increase in density of 18.6 percent, based upon atmospheric pressure volumes of both phases.

7.4. CoF_2

CoF_2 undergoes a polmorphic modification from the rutile to a distorted fluorite structure [7]. The transition is sluggish and occurs in the range 130–150 kbar at room temperature. The distortion of the fluorite structure is manifested by a small deviation from the cubic by a c/a ratio less than 1.01. The superlattice reflections (200), (311) and (310) appear in the powder x-ray diffraction pattern.

7.5. EuF_2

EuF_2 which crystallizes in the CaF_2-type crystal structure at atmospheric pressure and room temperature, transforms to the orthorhombic $PbCl_2$-type structure at 114 kbar and 400 °C. The high pressure modification, EuF_2(II), has unit cell dimensions $a = 3.803$ Å, $b = 6.324$ Å and $c = 7.435$ Å. The $PbCl_2$-type phase of EuF_2(II) can be retained metastably at atmospheric pressure undergoing an overall volume reduction of 10 percent with respect to the normal volume of EuF_2(I) [219].

7.6. MnF_2

X-ray investigation of MnF_2 at high pressure and high temperature reveal at least five polymorphic modifications. On the basis of simple crystal chemistry considerations, the ratio of atomic radii is close to the upper limit of stability for the rutile structure and a polymorphic modification of MnF_2 with coordination number eight would be a reasonable assumption [6]. In the early pressure experiments on MnF_2, a new phase was discovered which is an analogue of the α-PbO_2-type crystal structure also having the coordination number six (6). This investigation was carried out with quenched phases which made it possible to study the product only after its removal from the pressure chamber. In later studies [133], which permitted x-ray examination of the sample while under pressure, it was shown that the α-PbO_2-type modification of MnF_2 did not form in the high pressure region on the loading cycle, but was a metastable phase which was formed on the unloading cycle and retained at atmospheric pressure. In another experiment it was shown that the α-PbO_2-type phase of MnF_2 used as the starting material transforms to the rutile-type structure at approximately 30 kbar and room temperture [133].

In experiments in which rutile-type MnF_2 is used as the starting material three additional polymorphic modifications are observed at high pressure and temperature. NaCl was used as an internal pressure calibrant with an accuracy of $\pm$ 2 kbar for pressure up to 40 kbar and $\pm$ 3 kbar for pressure greater than 40 kbar. The error in temperature calibration was stated to be less than or equal to $\pm$ 5 percent. At room temperature and $P = 33 \pm 4$ kbar MnF_2(I) [256] transforms to a distorted fluorite phase MnF_2(II) which is stable up to approximately 150 kbar. At 70 kbar MnF_2(II) was initially indexed as tetragonal with unit cell parameters $a = 5.18$ Å, $c = 5.01$ Å, $Z = 4$ and $\rho_c = 4.59$ g/cm^3. Subsequent studies have never revealed the presence of additional x-ray reflections consistent with an orthorhombic unit cell with $a = b = 5.03$ Å, $c = 5.28$ Å, $Z = 4$ and $\rho_c = 4.62$ g/cm^3 [132]. It is assumed that this structure is the same as orthorhombic ZrO_2 [132] which is also a high pressure polymorph with very nearly the same lattice constants. The observed h, k, l of this ZrO_2 phase are consistent with space group $P2_12_12_1$, however, only powder data are available and the structure has not been solved.

At approximately 150 kbar and room temperature another polymorph, MnF_2(III) is formed with an increase in density of 6 percent at the MnF_2(II)-MnF_2(III) phase boundary [133]. This new phase can be indexed on the assumption of an orthorhombic unit cell with $a = 3.25$ Å, $b = 5.54$ Å, $c = 6.88$ Å, $Z = 4$ and $\rho_c = 4.98$ g/cm^3. The h, k, l reflections observed in the x-ray diffraction pattern of MnF_2(III) are in agreement with space group Pmnb (D_{2h}^{16}) and may be isomorphic with the orthorhombic $PbCl_2$ structure. A similar transition is observed in CaF_2, CdF_2, SrF_2 and BaF_2 at high pressure and room temperature.

The investigation of the polymorphism of MnF_2 was extended to the temperature range up to 400 °C and to a maximum pressure of 80 kbar [133]. In this study a cubic modification MnF_2(V) with the fluorite structure was confirmed by simultaneous x-ray techniques. At 40 kbar and

400 °C the lattice constant of MnF_2(V) is $a = 5.192$ Å.

The pressure-temperature phase diagram of MnF_2 has a triple point with coordinates at 33 kbar and 210 °C. These values are obtained from an extrapolation of the phase boundaries due to the experimental difficulty of obtaining data in the region of the triple point. In order to determine where the MnF_2(I)-MnF_2(II) phase boundary intersects the temperature axis, a differential thermal analysis of MnF_2 was made at 1 bar. At 710 ± 5 °C a thermal arrest was detected which apparently corresponds to the rutile-fluorite phase boundary [133].

7.7. NiF_2

NiF_2 undergoes a polymorphic modification from the rutile to a distorted fluorite structure [7]. The transition temperature decreased from 600 °C at 20 kbar to 375 °C at kbar. The distortion of the fluorite structure is manifested by a small deviation from the cubic by a c/a ratio of less than 1.01. The superlattice reflections (020), (311) and (310) appear in the powder x-ray diffraction pattern.

7.8. PbF_2

In addition to the eight-coordinated cubic fluorite phase, PbF_2 can also exist at normal conditions in the orthorhombic $PbCl_2$-type structure which is a quasi nine coordinated phase. In both phases there are four atoms per unit cell, but there is a 10 percent increase in density when going from the cubic to the orthorhombic symmetry. The orthorhombic phase should be the stable one at high pressure and such a transition was reported by Schmidt and Vedam [216] to occur at 4.8 kbar at 295 °C. Samara [213] reported that the transition exhibits strong kinetic effects and initiated between 3.93 and 4.75 kbar at room temperature depending on how long the pressure is held constant in the vicinity of the transition. The 3.93 kbar point was determined by increasing the pressure and holding it constant.

Kessler et al. [144] reported the Raman spectrum of PbF_2(II) and confirmed that the structure is orthorhombic $PbCl_2$-type. Unit cell data [216] are $a = 3.897$ Å, $b = 6.441$ Å, $c = 7.648$ Å, $Z = 4$ and $\rho_c = 8.48$ g/cm^3. From neutron powder diffraction data Boldrini and Loopstra [43] determined the atomic positions and the crystal structure of PbF_2(II).

7.9. SrF_2

SrF_2 crystallizes in the fluorite-type structure at normal temperature and pressure. Seifert [219] reported a pressure induced transformation in SrF_2 above 55 kbar to the orthorhombic α-$PbCl_2$-type structure.

7.10. ZnF_2

In some respects the phase diagram of ZnF_2 is similar to that of MnF_2. One notable correspondence is the existence of ZnF_2(II) which is isostructural with α-PbO_2 [129] and is only found in samples quenched from the high pressure, high temperature conditions $P = 50$ kbar and $T = 1500$ °C. This phase reverts to ZnF_2(I) after 2 hours at 400 °C. The transition ZnF_2(I)-ZnF_2(II) is accompanied by a color change from white to dark gray.

In an x-ray diffraction investigation of ZnF_2 at room temperature up to 130 kbar, a reversible phase transition was observed to take place from the rutile-type structure to a nonclinic phase ZnF_2(III) which is apparently isostructural with the monoclinic phase of ZrO_2. The transition started at 70–80 kbar and was complete at 110 kbar. The unit cell parameters are $a = 5.29$ Å, $b = 4.196$ Å, $c = 5.05$ Å, $\beta = 79.4°$ and $Z = 4$ [131].

Further x-ray investigations at 300 °C in the region 70–80 kbar revealed a cubic phase, ZnF_2(IV) which has the CaF_2-type structure [131]. In all the experiments in which rutile was formed, the quenched product after removal from the pressure cell always showed a mixture of the rutile and α-PbO_2 type phases. Kabalkina and Popova [129] suggested that the α-PbO_2 phase represents an intermediate structure during the transformation from fluorite to rutile.

7.11. $FeCl_2$

Anhydrous ferrous chloride $FeCl_2$ exhibits a number of interesting properties and has been extensively studies. It simulates an anisotropic ferromagnet and has a tricritical point. It is quite compressible, has low sound velocities and a strong magnon-phonon coupling. As a result of magnetic studies at high pressure a phase transition has been detected at 5.8 kbar and room temperature [257].

The low pressure form of $FeCl_2$ is rhombohedral and crystallizes in a close packed layer structure in which hexagonal sheets of iron ions are separated by two layers of chlorine ions. The halide ions have nearly a cubic close packing arrangement. The symmetry is primitive rhombohedral, space group R3m and has unit cell data $a = 3.598$ Å, $c = 17.536$ Å, $Z = 6$ and $\rho = 3.25$ g/cm^3 indexed on the more convenient triple hexagonal unit cell. The stacking sequence for the close packed chlorine ions is BAC...BAC with the repeat distance encompassing six chlorine planes along the "c" axis.

At approximately 5.8 kbars the phase transition involved a crystallographic change in which the new c axis $c^* = 1/3c$. The sequence of the chlorine layers is CB...CB in the high pressure phase which has the $FeBr_2$ structure, space group P3m.

7.12. $HgCl_2$

Bridgman (51,52) detected a solid-solid transition in $HgCl_2$ at room temperature near 20 kbar. The $HgCl_2$(I)-$HgCl_2$(II) phase boundary was measured more precisely by Kalliomaki and Meisalo [135] from 270 °C at 6 kbar at 140 °C at 11 kbar.

The melting curve of $HgCl_2$ was originally determined up to 22 kbar by Darnell and McCollum [88] in a piston cylinder apparatus. A second melting determination by Bardoll and Tokheide [18] up to a maximum pressure of 6 kbar resulted in a melting temperature 12 percent higher than found by Darnell and McCollum [88]. The discrepancy is probably accounted for by a difference in pressure calibration. The cell of Darnell and McCollum used solid pressure transmitting medium while Bardoll and Tokheide used argon. Due to the inherent greater accuracy, the latter method

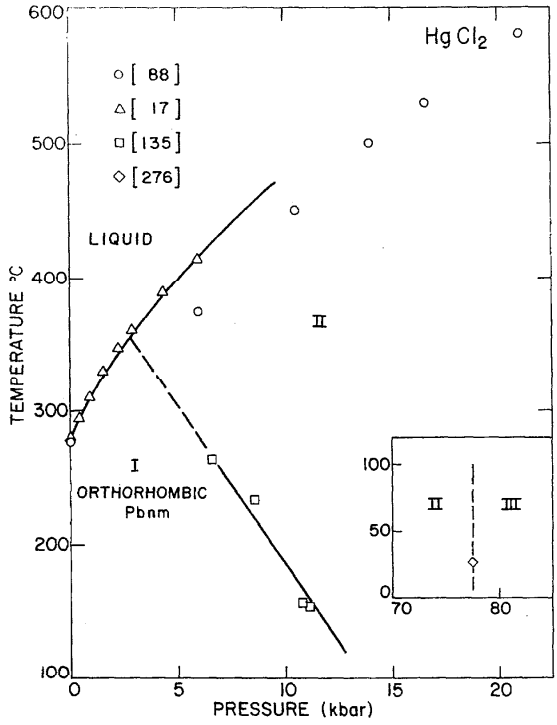

FIGURE 7. Phase diagram for $HgCl_2$.

is preferred.

The melting curve determinations [17,88] of $HgCl_2$ gave no evidence for the existence of a triple point. Extrapolating the $HgCl_2$(I)-$HgCl_2$(II) phase boundary to the melting curve indicates there should be a triple point at about 348 °C and 2.6 kbar.

A second solid-solid phase transition at room temperature was found at about 90 kbar by Zahner and Drickamer [276]. This boundary was followed to about 300 °C by Kalliomaki and Meisalo [135] where the transition pressure had decreased to 45 kbar. The phase diagram of $HgCl_2$ is presented in figure 7.

7.13. $SrCl_2$

Strontium dichloride which crystallizes in the cubic (Fm3m) symmetry when prepared at 1 bar pressure undergoes a transformation to an orthorhombic structure under the influence of high pressure and high temperature [55]. Since $BaCl_2$ has a high temperature cubic phase isostructural with $SrCl_2$(I) and a low temperature orthorhombic (Pbnm) phase, it was proposed $SrCl_2$(II) might have a similar orthorhombic phase at high pressure.

The synthesis of $SrCl_2$(II) was carried out in the region of 58 kbar and 800 °C. X-ray diffraction analysis confirms that the high pressure phase is orthorhombic with unit cell dimensions $a + 7.548$ Å, $b + 8.979$ Å and $c = 4.411$ Å. The space group was determined to the Pnam on the basis of powder diffraction data. These data suggest that $SrCl_2$(II) may be isostructural with orthorhombic $BaCl_2$ since their space groups represent the same symmetry with different axial designations. The calculated density of $SrCl_2$(II) is 3.52 g/cm^3 compared to 3.10 g/cm^3 for the cubic phase, an increase of approximately 12 percent. There is no experimental data on the $SrCl_2$(I)-$SrCl_2$(II) phase boundary.

7.14. $SrCl_2 \cdot 6H_2O$

The hexahydrate of $SrCl_2$ melts incongruently at 61.34 °C and atmospheric pressure according to the relation $SrCl_2 \cdot 6H_2O = SrCl_2 \cdot 2H_2O + 4H_2O$. Pistorius [191a] investigated the melting curve up to 30 kbar and found it to be a linear function of the pressure expressed by the equation $T(°C) = 61.34 + 5.3\ P(kbar)$.

A pressure induced transformation was detected at 32 kbar and 22 °C by a discontinuity in the electrical resistance trace [191a]. This behavior was reversible and the phase boundary was determined at a number of points between 22 and 170 °C. The phase boundary between $SrCl_2 \cdot 6H_2O$(I) and $SrCl_2 \cdot 6H_2O$(II) is a linear function of pressure $T = 15.5\ P - 470(°C)$. The invariant point $SrCl_2 \cdot 6H_2O$(I)-$SrCl_2 \cdot 6H_2O$(II)-$SrCl_2 \cdot 2H_2O$ is located at $P = 53 \pm 5$ kbar and $T = 345 \pm 30$ °C. Pressures are considered accurate to ± 5 percent and temperatures are within ± 5 °C.

7.15. $HgBr_2$

Bridgman [52] detected 3 polymorphic transitions along the 50 °C isotherm at 1.7, 23 and 38.7 kbar in $HgBr_2$ and studied their temperature dependence up to 160 °C. Bridgman [52] also measured the melting curve of $HgBr_2$ up to 6 kbar. The $HgBr_2$(I)-$HbBr_2$(I) phase boundary was determined from 200 °C to the triple point at 303 °C and 3 kbar by Bardoll and Tokheide [19]. The intersection of the $HbGr_2$(I)-

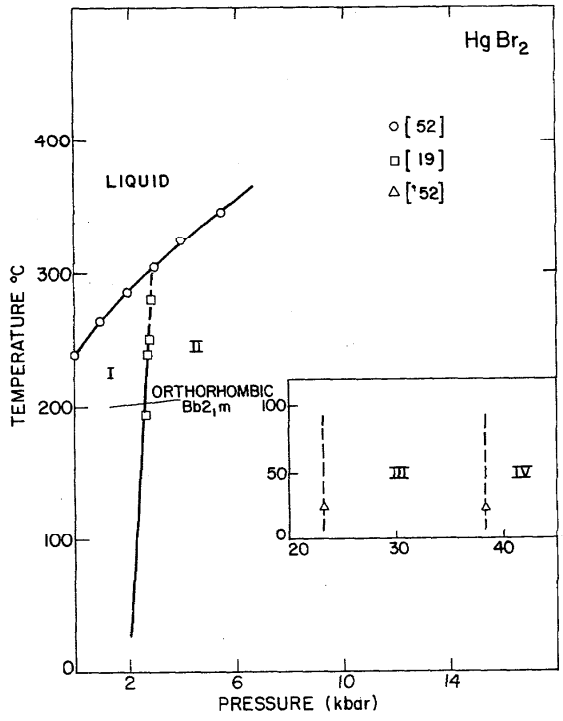

FIGURE 8. Phase diagram for $HgBr_2$.

$HgBr_2$(II) phase boundary with the melting curve requires a triple point at 3 kbar and 300 °C. These data are summarized in figure 8.

7.16. $ZnBr_2$

Polymorphic transitions in $ZnBr_2$ were reported by Bridgman [52] who observed a discontinuity in the high pressure behavior above 25 kbar. The anomalies were attributed to a crystallographic transformation but it was noted that there was some irregularity in the data which suggested the possibility of two closely spaced transitions.

The structure of $ZnBr_2$ under normal temperature and pressure conditions has not been resolved in detail. Oswald [189a] suggests a large unit cell with 32 molecules. The symmetry assignment is $I4_1/acd$ and there is an almost cubic bimolecular pseudocell.

Meisalo and Kalliomaki [171] examined the high temperature and high pressure regions of $ZnBr_2$ by means of a polarizing microscope and x-ray diffraction techniques. Investigation in the region 100–200 °C at atmospheric pressure failed to confirm the existence of a high temperature phase suggested by Bridgman [52]. At elevated pressures two polymorphic modifications were observed. The first transition ($ZnBr$(I)-$ZnBr_2$(II)) at about 15 kbar was sluggish at room temperature but much more rapid at high temperatures. The second transition ($ZnBr_2$(II)-$ZnBr_2$(III)) occurs at 33 kbar at room temperature and has a relatively large volume discontinuity. These two phase boundaries meet at a triple point at 30 kbar and 125 °C. Above the triple point the $ZnBr_2$(I)-$ZnBr_2$(II) transition is rapid and easily detected.

The x-ray data for $ZnBr_2$(II) at 25 kbar [171] can be indexed to a tetragonal unit cell with $a = 10.83$ Å and $c = 21.66$ Å with $c/a = 2$ suggesting a cubic pseudocell. This is based upon 12 reflections from powder data. The x-ray data for $ZnBr_2$(III) at 80 kbar [171] was indexed on a hexagonal unit cell with $a = 3.65$ Å and $c = 5.73$ Å, which is roughly in agreement with a CdI_2 layered structure.

7.17. GeI_2

Compressibility studies by Bridgman [52] suggest the possibility of a phase transformation in GeI_2 at approximately 18 kbar and room temperature.

7.18. HgI_2

The first high pressure investigation of HgI_2 was performed by Bridgman [48] in 1915. This work consisted of a determination of the pressure-temperature dependence of the α(red)-β (yellow) phase boundary by dilatometric techniques. At room temperature HgI_2(I) (β-form) crystallizes in a tetragonal structure which transforms into the orthorhombic structure of HgI_2(II) (α-form) at 120 °C and atmospheric pressure. Bridgman determined that the HgI_2(I)-HgI_2(II) phase boundary went through a maximum at 5 kbar and 180 °C. Tonkov and Tikhomirova [252] who extended Bridgman's measurements to lower temperatures and higher pressure found evidence for a new high pressure phase HgI_2(II) by DTA techniques. In this work temperatures were recorded with chromel-alumel thermocouples (accuracy ± 3 °C) and pressures with a mangain resistance manometer with an accuracy of ± 100 bars. The HgI_2(I)-HgI_2(III) phase boundary was recorded on both isobaric as well as isothermal cycles. This phase boundary has not been corroborated independently by any other investigator. Brasch et al. [45] claim their research confirms that the HgI_2(III)-HgI_2(II) transition at approximately 13 kbar and room temperature is the same as the α(red)→β (yellow) transition observed at 127 °C and atmospheric pressure. X-ray examination of HgI_2 by Miller [173] up to a maximum pressure of 120 kbar reveal three polymorphic modifications. According to these data the α(red) tetragonal form is stable up to 13 kbar. The β yellow orthorhombic phase is stable between 13 and 75 kbar. At approximately 75 kbar a new phase appears [173] which can be indexed hexagonal with space group $P\bar{3}cl$, $Z = 4$ and unit cell dimensions $a = 4.22$ Å and $c = 23.70$ Å.

The melting curve of HgI_2 has been investigated by 3 different groups [18,88,252] Tonkov and Tikhomirova [252] measured the melting curve up to 20 kbars by DTA techniques and present evidence for a high temperature phase which exists between 254 °C and the melting point (332 °C) at atmospheric pressure. Later investigations by Darnell and McCollum [88] and Bardoll and Tokheide [18,19] do not confirm the existence of this high temperature phase and furthermore place the melting curve approximately on the lower boundary of Tonkov and Tikhomirova's high temperature phase. The melting curve of Bardoll and Tokheide agrees very well with that of Darnell and McCollum up to approximately 3.5 kbar. At this point Bardoll and Tokheide report a triple point (338 °C, 3260 bars) between the liquid HgI_2(II) and HgI_2(IV), the latter a new high temperature

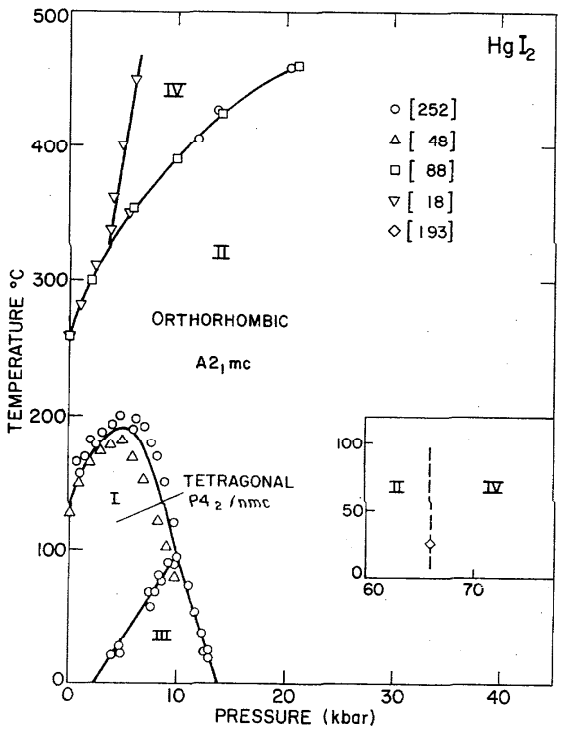

FIGURE 9. Phase diagram for HgI_2.

phase. The liquid-HgI_2(IV) phase boundary was followed to only 6 kbar. In the region above the triple point up to 20 kbar it appears that Darnell and McCallum may have determined the HgI_2(II)-HgI_2(IV) phase boundary. The HgI_2 phase diagram is illustrated in figure 9.

8. Oxides

8.1. Ag_2O

Ag_2O(I), the cuprite form of Ag_2O transforms to a CdI_2-type modification in the range 115–125 kbar and 1400 ± 200°C. The high pressure phase, Ag_2O(II), was quenched and retained metastably at room temperature and atmospheric pressure. The atmospheric pressure values of the hexagonal unit cell dimensions of Ag_2O(II) are $a = 3.072$ Å, $c = 4.941$ Å, with $Z = 1$ and $\rho_e = 9.5$ g/cm^3 ($\rho_c = 9.53$ g/cm^3). This represents an increase in density of 30 percent between the two phases, both evaluated at atmospheric pressure.

The oxygen atom occupies the position (0,0,0) and the two silver atoms are located at $\pm$ (1/3, 2/3, z) where $z = 0.25$. The transition from Ag_2O(I)-Ag_2O(II) is accompanied by a change in cation(anion) coordination from 2(4) to 3(6). The interatomic distances in Ag_2O(II) are Ag-O, 2.6 Å, and Ag-Ag, 2.86 Å.

8.2. CrO_2

CrO_2 is a transition metal oxide which is strongly ferromagnetic and magnetically ordered above room temperature. It can be prepared in the form of a crystalline powder at atmospheric pressure, but growth of large single crystals at atmospheric pressure has not been successful apparently due to metastability of CrO_2 at low pressures and the relatively high melting point of the oxide.

The first successful synthesis of CrO_2 single crystals was by Chamberlain [69]. Crystals as large as 1.5 mm $\times$ 0.3 mm were prepared in the range 900–1300 °C at a pressure 60–65 kbar. A number of flux techniques were tried to improve crystal growth but with no success. The Curie temperature was determined to be 125 °C and the resistivity to be $1.4–3.8 \times 10^{-4}$ ohm cm which is in the metallic range.

Porta et al. [196] synthesized single crystals of CrO_2 by flux techniques for the purpose of accurate x-ray examination. These crystals were prepared from a mixture of equimolar proportions of CrO_3 and Cr_2O_3 with five percent by weight KOH at 900 °C and 36 kbar.

The space group of CrO_2 is $P4_2/mnm$ with 2 molecules per unit cell which is isostructural with the rutile structure. The tetragonal lattice constants are $a = 4.419$ Å and $c = 2.915$ Å.

8.3. H_2O

H_2O forms more solid phases than any other substance except SiO_2. In addition to the liquid phase there are 9 crystalline phases accessible at pressures below 23 kbar so that the experimental problems are modest compared to many systems. The earliest significant investigation of the H_2O phase diagram was that of Tamman [251] in which he reported the existence of the phases H_2O(II) and H_2O(III).

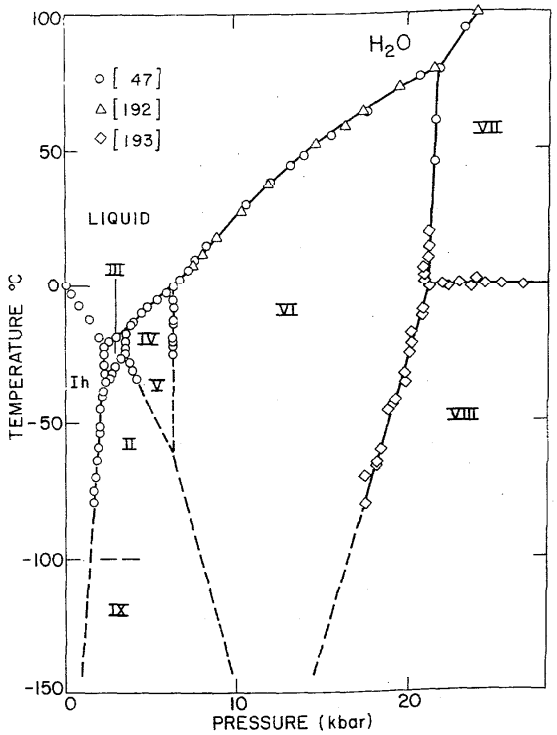

FIGURE 10. Phase diagram for H_2O.

Without doubt the most important single contribution was made by Bridgman [47] in his 1911 paper. In a careful study of the H_2O phases up to 20 kbar he discovered H_2O(V) and H_2O(VI). In this work he reported the determinations of the following phase boundaries: H_2O(L)-H_2O(I), H_2O(L)-H_2O(III), H_2O(L)-H_2O(V), H_2O(L)-H_2O(VI), H_2O(I)-H_2O(II), H_2O(I)-H_2O(III), H_2O(II)-H_2O(III), H_2O(III)-H_2O(IV), H_2O(II)-H_2O(V) and H_2O(V)-H_2O(VI). It is important to note that later investigations in the region up to 20 kbar are in excellent agreement with these results. The data for the phase boundaries are taken from various researchers as indicated in the phase diagram of figure 10.

In 1937 using improved apparatus Bridgman [50] discovered H_2O(VII). H_2O(VIII) and H_2O(IX) were discovered by Whalley et al. in 1966 [267] and 1968 [269], respectively. In 1935 Bridgman investigated the analogous phase diagram of D_2O and detected a new metastable phase D_2O(IV) in the stability field of D_2O(V). He was then able to confirm that this phase was also present in his H_2O data and designated it as H_2O(IV).

Pistorius et al. [192] determined the melting curve of H_2O(VII) up to 200 kbar and fit their data to a Simon equation. It is necessary to know P_0T_0 (the pressure and temperature of the triple point H_2O(L-VI-VII)) very accurately. The H_2O(VI-H_2O(VIII) transition at room temperature was determined as 21.845 by Bridgman and 21.416 kbar by Kennedy and LaMori [143] and consequently the pressures of Bridgman were lowered by 0.430 kbar. In a later work Pistorius et al. [193] made a determination of the H_2O(VI)-H_2O-(VII) phase boundary which at room temperature occurred

at lower pressures than Bridgman's values but agreed at the H_2O(L-VI-VII) triple point. As a result of this, Pistorius et al. [193] corrected their 1963 melting curve for H_2O(VII).

In the early work it was evident that some curvature existed in the H_2O(VI)-H_2O(VII) phase boundary. In a study of the dielectric properties of H_2O(VII), Whalley et al. [267] found that at 0 °C the dielectric constant abruptly decreased suggesting a new phase. Brown and Whalley [56] investigated the H_2O(VI)-H_2O(VII) phase boundary by volumetric techniques and detected a sharp break in the curve at 0 °C and 21 kbar. Pistorius et al. [193] were able to map the H_2O-(VII)-H_2O(VIII) phase boundary from the sharp DTA signals on both heating and cooling cycles.

The normal form of ice with which we are all familiar is ice Ih. For the purpose of this report we choose to designate phases by their chemical symbols instead of mineral names and therefore use the designation H_2O(Ih). H_2O(Ic), which occurs in the region of H_2O(Ih), always appears to be metastable to it. This phase was first reported by Konig [147].

The crystallography of the various H_2O solid phases is very complex. The presence of disordering in the hydrogen atoms complicates the structural determinations. A combination of probes are necessary to unambiguously determine structures. X-ray diffraction techniques primarily give information on oxygen positions. Infrared and Raman measurements are very important in detecting hydrogen bonding. Dielectric measurements tell something about the type of disorder that might be present. Transformation entropies are important sources of information on the relative configurational entropy which can also be related to relative disorder.

The normal form of ice H_2O(Ih) is hexagonal with space group symmetry $P6_3/mmc$. H_2O(Ic) is cubic with space group Fd3m. Both of these phases are disordered.

H_2O(III) is the most accessible of the high pressure phases. It is prepared by cooling the liquid phase at 3 kbar pressure, from room temperature down to − 40 °C at which point it is quenched in liquid nitrogen. H_2O(III) is the least dense of the high pressure phases of ice ($\rho_c = 1.16$ g/cm^3 at − 175 °C) and has a tetragonal structure (space group $P4_12_12_1$ $a = 6.73$ Å, $c = 6.83$ Å) involving a tetrahedrally linked hydrogen bond framework. The increase in density relative to H_2O(I) (0.94 g/cm^3) is accomplished by a distortion from ideal tetrahedral coordination [137]. There is no decrease in bond length or increase in nearest neighbor coordination, but instead a decrease in next nearest neighbor distance from about 4.5 Å in H_2O(I) to 3.64 Å in H_2O(III).

The hydrogen atoms are ordered in H_2O(II) whereas H_2O(III), H_2O(V), H_2O(VI), H_2O(VII) and H_2O(VIII) are disordered above − 40 °C. The absence of disorder in H_2O(II) is demonstrated from entropy measurements [269]. The crystal structure is rhombohedral $R\bar{3}$ with $a = 7.79$ Å, $\alpha = 113.1°$ and $Z = 12$.

At 6 kbar and − 6 °C H_2O(IV) has a density of 1.29 g/cm^3 but no structural data are available. In H_2O(V) there are two phases, a high-V and low-V which are disordered and partially ordered, respectively. Both are monoclinic A2/a. The H_2O(VI) structure was reported by Kamb [136,138] to be tetragonal $P4_2/nmc$ with $a = 6.17$ Å and $c = 5.70$ Å. This phase is disordered and there is also an orthorhombic low-VI partially ordered phase. The tetragonal structural is built up of hydrogen bonded chains of water molecules that are analogs of tectosilicate chains out of which the fibrous zeolites are constructed. The chains are linked laterally to one another to form an open zeolite like framework. The cavities in this framework are filled with a second framework identical with the first. The two frameworks interpenetrate but do not interconnect. This feature achieves high density in a tetrahedrally linked framework structure.

H_2O(VII) is cubic Pn3m with $a = 3.40$ Å and $Z = 2$. In this structure each oxygen alone is surrounded by eight instead of the normal four others at the typically H-bonded distance of 2.88 Å (at 25 kbar). Unless the nature of the bonding is greatly altered in this phase each water molecule can have only four hydrogen bonds with its neighbors in tetrahedral directions and, therefore, must be in non-bonded repulsive contact with the other four neighbors.

In H_2O(VIII) which is tetragonal, $I4_1/and$, an even more unusual situation occurs. Each oxygen atom has two oxygen neighbors at 2.80 Å, four at 2.96 Å, two at 3.15 Å and one at 3.19 Å. The four at 2.96 Å are H-bonded while the others are not. H_2(IX) is the ordered variant of H_2O(III) and is stable below − 100 °C.

The thermal conductivity for the nine solid phases of H_2O was measured by Ross et al. [205]. Kawai et al. [141] report the dielectric-metal transition in H_2O at a very high unspecified pressure. This was concluded from an abrupt drop in electrical resistance by more than 5 orders of magnitude, a result which has not been duplicated and is questioned by many workers in the high pressure field.

8.4. D_2O

In essential details the phase diagram of D_2O is identical to that of H_2O [49]. The most genral characterization is that the triple points in the D_2O diagram all occur at higher temperatures and the transition lines, except those which are approximately vertical, all occur at higher temperatures than in the H_2O diagram. These differences become less, however, at higher pressures.

Pistorius et al. [193] determined D_2O(L)-D_2O(VI), D_2O(L)-D_2O(VIII), D_2O(VI)-D_2O(VII) and the D_2O(VII)-D_2O(VIII) phase boundaries up to 40 kbar. In the region of overlap (i.e., D_2O(L)-D_2O(VI)) his work is in good agreement with that of Bridgman.

Neutron diffraction examination of D_2O polymorphs under helium pressure [5] confirm that the phases Ih, Ic, II, III and IX have the same crystal structures as the H_2O analogs. The presence of helium appears to have affected the locations of the D_2O(I)-D_2O(II) and the D_2O(I)-D_2O(III) phase boundaries.

8.5. GeO_2

At room temperature and atmospheric pressure GeO_2 can exist in two crystallographic forms, the hexagonal α-quartz an the tetragonal rutile structures. The α-quartz form of GeO_2 is a high temperature phase, but due to the sluggishness of the GeO_2 (α-quartz→rutile) transformation the α-quartz form is readily obtained at room temperature. The α-quartz form of GeO_2 readily converts to the rutile form when

subjected to high pressures. Sawamoto [215] reported that at high pressure GeO_2 transformed to the orthorhombic α-PbO_2-type structure. No crystal data is available yet. Liu et al. [160] reported the synthesis of a new hexagonal form of GeO_2 at high pressure from GeO_2 glass by heating with a YAG laser. The new phase has the Fe_2N-type structure (L'_3) with unit cell data $a = 2.729$ Å, $c = 4.312$ Å and $\rho_c = 6.24$ g/cm^3.

8.6. HfO_2

The monoclinic-tetragonal phase transformation in HfO_2 has been investigated at high temperatures by Baun [21] and reported to occur in the range 1500 to 1600 °C while the reverse transformation occurs in the range from 1550 to 1450 °C. Curtis et al. [84] and Boganov [40] both place this transition at approximately 1900 °C. Cubic HfO_2 has been obtained by heating pure HfO_2 about 2700 °C [27]. An additional orthorhombic phase was identified by Bendeliani [27]. The new phase was obtained under high pressure in the range 40 to 110 kbar at temperatures of 20 to 1700 °C. X-ray examination of quenched samples give the following crystal data: $a = 5.056$ Å, $b = 5.006$ Å, $c = 5.224$ Å $\rho_c = 10.58$ g/cm^3, and $z = 4$. The space group based on extinctions in the powder data is assumed to be $P2_12_12_1$. Bocquillon et al. [37] performed a DTA study of the phase boundaries in HfO_2. In HfO_2, the monoclinic phase, the tetragonal phase and the orthorhombic phase join in a triple point at approximately 1200 °C and 15 kbar. At present little is known about the tetragonal-cubic phase boundary (fig. 11).

8.7. MnO_2

Both amorphous and crystalline (rutile) forms of MnO_2 have been heated by a laser in diamond-anvil pressure cell by Liu [158] resulting in a new metastable high pressure modification. The new phase has been tentatively indexed as cubic with $a = 9.868$ Å. The samples were heated at pressures of 220 to 250 kbar. Clendenen and Drickamer [79] reported the relative volume of MnO_2 up to a pressure of 140 kbar where the MnO_2 underwent a first order phase transition which was not investigated.

8.8. PbO_2

Lead dioxide is known in two forms at atmospheric pressure, the common tetragonal rutile-type and the α-PbO_2 phse [270] which was first prepared under restricted current conditions on the anodes of storage batteries, but has since been prepared by chemical methods [270]. Zaslavskii et al. [277] reported an orthorhombic unit cell with $a = 4.938$ Å, $b = 5.939$ Å and $c = 5.489$ Å for α-PbO_2. α-PbO_2 can be prepared easily at high pressure in the region 13–15 kbar and 200–500 °C [249]. This region appears to be the true stability field of α-PbO_2.

Goldschmidt [249] predicted the PbO_2 and MnF_2 would be the most likely rutile-type substances to undergo a phase transformation to a fluorite-type structure since their radius ratios $r_{Pb}/r_O = 0.65 (r_{Mn}/r_O = 0.61)$ are very close to the critical value 0.752 for the fluorite structure derived from simple geometrical considerations.

The crystal structure of PbO_2(II) (α-PbO_2) is orthorhombic and similar to the columbite structure [277]. The

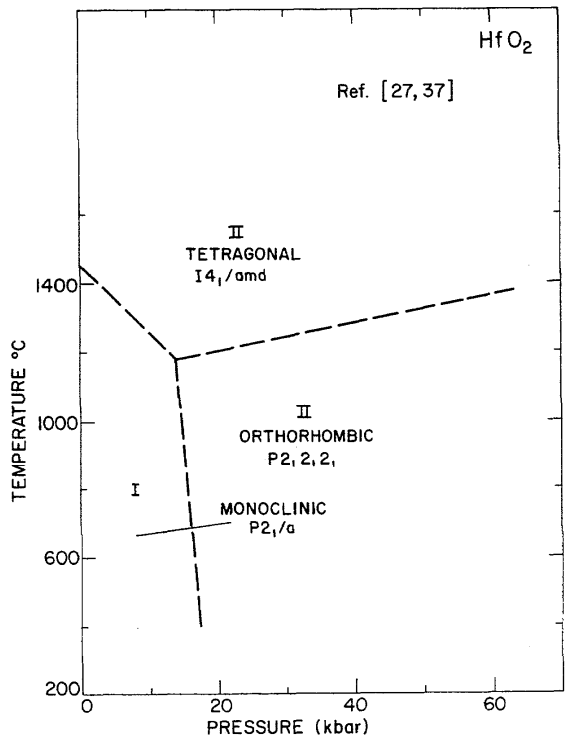

FIGURE 11. Phase diagram for HfO_2.

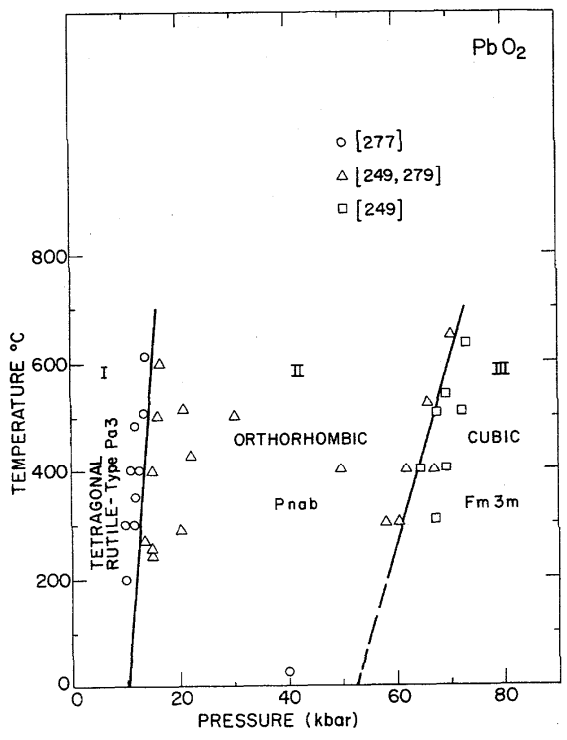

FIGURE 12. Phase diagram for PbO_2.

PbO_2(I)-PbO_2(II) transformation was shown to be reversible at high temperatures and the phases were confirmed by x-ray diffraction [270]. The high pressure form can be quenched to room temperature and shows no tendency to revert to the rutile phase. After heating at 100 °C for two weeks, a trace of PbO_2(I) appeared. The heat of transition for the PbO_2(II)-PbO_2(I) transition for the PbO_2(II)-PbO_2(I) transition was calculated to be 11 calories per mole and the change in free energy 322 calories per mole [249].

The fluorite-type polymorph of PbO_2 was formed at pressures above 60 kbar in the temperature range 300–600 °C [249]. The cubic cell parameter was determined to be 5.349 Å from x-ray diffraction data obtained from quenched samples at atmospheric pressure. The transformation to PbO_2(III) is very sluggish [249] and the quenched samples are quite metastable undergoing a retrograde transformation to PbO_2(II) at room temperature. A phase equilibrium boundary between PbO_2(II) and PbO_2(III) was determined as P(kbar) = 52.5 + 0.30 T(°C). The density of the fluorite form of PbO_2 is 8.2 percent greater than the rutile form. The phase diagram of PbO_2 is shown in figure 12.

8.9. PtO_2

A distorted rutile-type phase of PtO_2 was synthesized at 700 °C and 3000 bar pressure [233] from the hexagonal phase. High pressure PtO_2(II) is orthorhombic with $a = 4.487$ Å, $b = 4.536$ Å, $c = 3.137$ Å and $z = 2$. The space group is probably Pnn2 or Pnnm. This is the first example of an orthorhombic distortion among the rutile oxides. It does exist, however, for $CaCl_2$ and $CaBr_2$, which have similar unit cells, space group Pnnm. Sahl [211] has shown that perfect close packing of anions results in an orthorhombic distortion of the ritule structure.

8.10. RhO_2

The tetragonal rutile form of RhO_2 was synthesized from the hexagonal RhO_3 at 700 °C and 3000 bar oxygen pressure [223]. The lattice constants are $a = 4.486$ Å, $c = 3.088$ Å with $Z = 2$. Plotting unit cell volume against ionic radius for several rutile compounds places RhO_2 in the middle of the rutile stability region. Ordinarily, strictly high pressure phases lie at the edge of the stability field.

8.11. SiO_2

SiO_2 in its varied crystalline forms (fig. 13) plays an extremely important role in the crystal chemistry of the earth. The three principal crystalline forms of SiO_2 found in the earth's crust (quartz, tridymite, and cristobalite) have quite distinct crystal structures, each with a well defined field of stability under equilibrium conditions. The transformations from one to another are quite sluggish so the higher temperature forms, cristobalite and tridymite, can exist metastably below their transformation temperatures. Each of these minerals, quartz, metastable tridymite and metastable cristobalite have a low- and high-temperature modification designated α- and β-, respectively. All six crystal structures are built from SiO_4 tetrahedra which are linked by sharing corners with another tatrahedron in a three dimensional framework such that every silicon has four oxygens and every oxygen has 2 silicons as nearest neighbors. While the transformation from α- to β-forms of quartz, tridymite and cristobalite, involves minor atomic displacements, the transformations between quartz, tridymite and cristobalite are reconstructive.

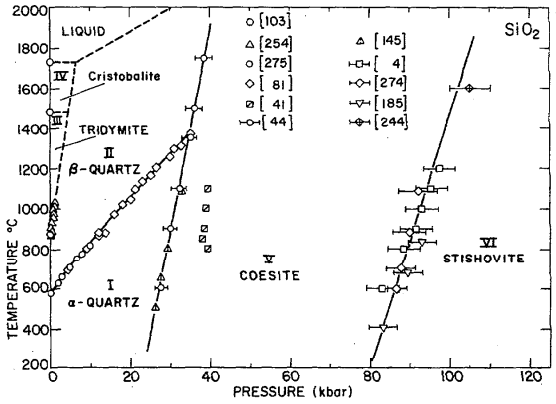

FIGURE 13. Phase diagram for SiO_2.

In addition to common SiO_2 minerals just mentioned there are at least five high pressure phases, keatite, coesite, stishovite, a hexagonal Fe_2N-type and a high pressure orthorhombic form. These and possibly other high pressure forms of SiO_2 are very important in the crystal chemistry of the earth in the region from the upper mantle to the lower mantle. Coesite and stishovite are the only high pressure modifications of SiO_2 which have been found in nature. Stoffler and Arndt [245] published an excellent summary of the research involving coesite and stishovite with a very complete list of referencs. Since the literature pertaining to the various SiO_2 phases is voluminous, this review will be principally concerned with those results which relate to the stability fields in the high pressure region and general information relating to the synthesis and structure of the high pressure phases.

Atmospheric Pressure Phase: For the three SiO_2 phases which occur at atmospheric pressure Fenner [103] determined the transformation temperatures plus the α-β- transformation temperatures for metastable tridymite and metastable cristobalite. In addition to an investigation of the thermodynamic properties of the crystalline forms of SiO_2 Mossman and Pitzer [177] calculated the pressure dependence of the tridymite, cristobalite and liquid SiO_2 phase boundaries a little beyond a kilobar. An analysis of the literature indicates the only high pressure measurements for this part of the SiO_2 phase diagram were the measurements of the tridymite-β-quartz boundary up to 1 kbar by Tuttle and Bowen [254].

The pressure dependence of the α-β quartz boundary was first investigated by Gibson [111] whose pressure data extends to 15 kbar. He states that above 3 kbar the α-β inverison temperatures are extrapolated and their reliability is not comparable to that of the other data. The work of Yoder [275] up to 10 kbar and kbar and that of Cohen and Klement [81] up to 35 kbar agree very well in the region of overlap. Gibson's point (643 °C) at 3 kbar lies 10 °C below that of

Yoder (653 °C). The combined curves of Yoder [275] and Cohen and Klement [81] represent the current best data for the pressure dependence of the quartz α-β inversion temperature.

SiO_2-High Pressure Phases: Coesite, a dense form of SiO_2 was discovered by Coes [80] at high pressures and high temperature. Since the form has a density of 3.01 g/cm^3, which is considerably greater than that of quartz, 2.65 g/cm^3, this discovery aroused considerable interest. There was some informal speculation that this phase might have six coordination although MacDonald [164] pointed out that this would require an even greater density. A summary of physical properties has been tabulated by Stoffler and Arndt [245] and Sclar et al. [217]. Ramsdell [199] demonstrated that coesite was monoclinic (Pseudo-hexagonal) with space group C2/c with unit cell data $a = 7.17$ Å, $b = 7.17$ Å, $c = 12.38$ Å, $\gamma = 120.0°$ and $Z = 16$. The crystal structure was solved by Zoltai and Buerger [278]. The first natural coesite was found in sheared sandstone samples collected from Meteor Crater, Arizona by Chao et al. [70].

At least 12 studies of the quartz-coesite transition have been reported since Coes [80] first synthesis. The agreement among the workers has not been good. MacDonald [164] reported on the first detailed study of the quartz-coesite stability field. MacDonald's boundary for the quartz-coesite transition was determined in a piston anvil device, for which it was assumed at that time that the pressure was relatively uniform across the anvil face. MacDonald's investigations cover the range 400–600 °C. Griggs and Kennedy [114] traced the quartz-coesite transition from 300–900 °C in apparatus similar to that used by MacDonald [164] and the results agreed with MacDonald's through the overlapping range.

A further study of the quartz-coesite transition in piston anvil apparatus was reported by Dachille and Roy [85] who examined the transition over almost the same ranges as MacDonald, 400–600 °C obtaining similar results.

Boyd and England [44] presented a very careful study of the quartz-coesite transition and their results contrast markedly with the results previously presented by MacDonald [164], Griggs and Kennedy [114] and Dachille and Roy [85]. Instead of a piston anvil device Boyd and England utilized the more hydrostatic piston cylinder apparatus.

Takahashi [250] also studied the quartz-coesite transition under pressure with a tetrahedral anvil apparatus. This apparatus was calibrated at room temperature without considering the pressure enhancement due to high temperatures. More recent data indicate that this correction may be as great as 1 kbar per 100 °C. Such a correction could easily bring Takahashi's data into agreeement with that of Boyd and England. To complicate matters, Boyd and England revised their data up-wards bringing it into fair agreement with Takahashi's uncorrected data. In order to resolved which result is correct Kitahara and Kennedy [145] made a detailed study of the phase boundary using piston cylinder and experimental procedures identical to those described by Boyd and England [44]. By correcting for friction these researchers obtained values for the quartz-coesite phase boundary which agree with the original data published by Boyd and England [44]. Furthermore, the uncorrected data of Kitahara and Kennedy agree well with Takahashi's published data.

Two further determinations of the quartz coesite boundary by Bell et al. [24] and Roy and Frushour [208] are in fair agreement with Kitahara and Kennedy [145] and Boyd and England [44]. A calculation of the phase boundary by Holm et al. [118] gives a curve which lies about 4 kbar higher than Takahashi's data. Naka et al. [182] examined the effects of shear on the quartz-coesite transition for wet and dry samples and observed a definite shift in the transition to lower pressures.

All the determinations of the quartz-coesite boundary discussed thus far were made with the "quench" method. Bohler and Arndt [41] made a determination of the transition over the temperature range 600°–1100° by in situ x-ray measurements with NaCl as an internal pressure standard. Pressure was determined from the change of the lattice parameter of NaCl by measuring the relative shifts of the strongest two diffraction lines (200) and (220) and by using compression data given by Decker [90] for selected temperatures. The presence of coesite was determined by the (040) and (200) diffraction lines. The authors estimate an accuracy in pressure of $\pm$ 1 kbar. As can be seen in the phase diagram, this boundary lies abut 8 kbar above the best previous results [44,145].

In evaluating the data for the quartz-coesite phase boundary, the best value appears to be a best fit of the data of Boyd and England [44], Kitahara and Kennedy [145], Bell et al. [24] and Roy and Frushour [208]. This covers a temperature range 350–1750 °C. The set of data (800–1100 °C) of Bohler and Arndt [41], however, cause some concern. The method is inherently superior but reviewers would like to see some independent data covering a larger range of temperature.

Stishovite was originally discovered by Stishov and Popova [242] at pressures in excess of 100 kbar. Stishovite has the rutile-type structure with unit cell data $a = 4.179$ Å, $c = 2.665$ Å, $Z = 2$ [242,243] and the density is 4.29 g/cm^3. This form represents a change in coordination from 4 of the coesite phase to 6. Stishovite was found to occur naturally in samples of Coconino Sandstone of Meteor Crater, Arizona [71]. A tabulation of its physical properties was published by Stoffler and Arndt [245] and Sclar et al. [218].

Since stishovite is accepted as a major constitute of the earth's mantle, there has been much interest in determining its properties and stability field. Wentorf [264], Sclar et al. [218], Ringwood and Seabrook [203], Bendeliani and Vereshchagin [26] and Minomura et al. [175] have described the synthesis of stishovite using different types of high pressure apparatus.

The first attempt to determine the coesite-stishovite transformation boundary was made by Stishov [244]. He derived the entroopy of stishovite from the entropy and density relations in the rutile-type oxides and estimated the transformation curve passing through an equilibrium point experimentally determined. Experimental determination of the transformation curve was performed by Ostrovskii [185,186] in the temperature range 410–830 °C with the aid of an opposed anvil type high pressure apparatus. His work was followed up by Akimoto and Syono [4] over the tem-

perature range 550–1200 °C using the tetrahedral anvil press. All the above determinations of the coesite-stishovite phase boundary were made with quenching experiments. Yagi and Akimoto [274] made an in situ determination of the phase boundary by means of x-ray diffraction techniques. Pressures were obtained through Decker's NaCl equation of state [90] using the (200) and (220) reflections. The authors estimate an accuracy in pressure measurements of $+2$ kbar at 100 kbar. The equation $P(\text{kbar}) = (80 \pm 2) + (0.011 \pm 0.003)T(°\text{C})$ was obtained for the coesite-stishovite equilibrium curve.

In the temperature interval 500–1200 °C, the determinations of Yagi and Akimoto [274] and Ostrovskii [185] fall within the experimental error flags of the data of Akimoto and Syono [4]. Also Stishov's [244] point at 1600 °C and 105 kbar in within the error flags of an extrapolation of Akimoto and Syono [4]. Stishov's calculated phase boundary also lies within this error flag of Akimoto and Syono [4].

Other high pressure phases of SiO_2 not observed in nature have been produced. Keatite [92] is a high pressure synthetic phase of SiO_2. It was prepared at 380–585 °C and 330–1200 bars. Its stability range is unknown.

German et al. [108,109] reported the preparation of an orthorhombic form of SiO_2 is shock wave experiments. This new dense phase was formed using a 350 kbar shock wave and has density of 4.435 g/cm^3. The unit cell dimensions of recovered samples are $a = 4.30$ Å, $b = 4.70$ Å and $c = 4.50$ Å. The crystal structure of this orthorhombic phase is unknown.

Liu et al. [160] produced a dense SiO_2 phase at high pressure by heating SiO_2 glass with a YAG laser. The structure is hexagonal Fe_2N type (L_3') with unit cell dimensions $a = 2.561$ Å and $c = 4.112$ Å. The room temperature 1 bar density is 4.26 g/cm^2.

8.12. SnO_2

SnO_2 has the tetragonal rutile structure common to many AB_2-type compounds. Suito et al. [248] and Liu [157] synthesized a new dense αPbO_2-type of SnO_2 in the region of 150 kbar and 800 °C. The phase boundry between SnO_2(II) and SnO_2(II) above 700 °C is represented by $P(\text{kbar}) = 140.0 + 0.022\ T(°\text{C})$. SnO_2(II) is orthorhombic with $a = 4.174$ Å, $b = 5.727$ Å, $c = 5.214$ Å, $\rho_c = 7.11$ g/cm^3 and $Z = 4$.

Clendenen and Drickamer [79] measured the room temperature compression of SnO_2 by x-ray techniques up to 250 kbar. At 250 kbar the SnO_2 underwent a first order transition which was investigated by optical techniques. There were no other phase transitions below 250 kbar.

Liu [159] reported the discovery of a new fluorite phase of SO_2 at very high pressures. The SnO_2 sample was compressed to about 250 kbar and heated by a continuous YAG laser. The cubit unit cell dimension $a = 4.925$ Å was determined at pressure. The density of the fluorite phase is approximately 15.5 percent greater than that of the rutile phase as a result of the coordination number increase from 6 to 8.

8.13. TeO_2

Tellurium dioxide has three known crystalline forms at standard temperature and pressure. Natural TeO_2 crystallizes in both the rutile and brookite structure of TiO_2 whereas all synthetically prepared TeO_2 forms in the paratellurite structure. Paratellurite can also be prepared by heating the tellurite phase above 600 °C. All the high pressure studies on this system have been devoted exclusively to paratellurite which has an interesting second order phase transition.

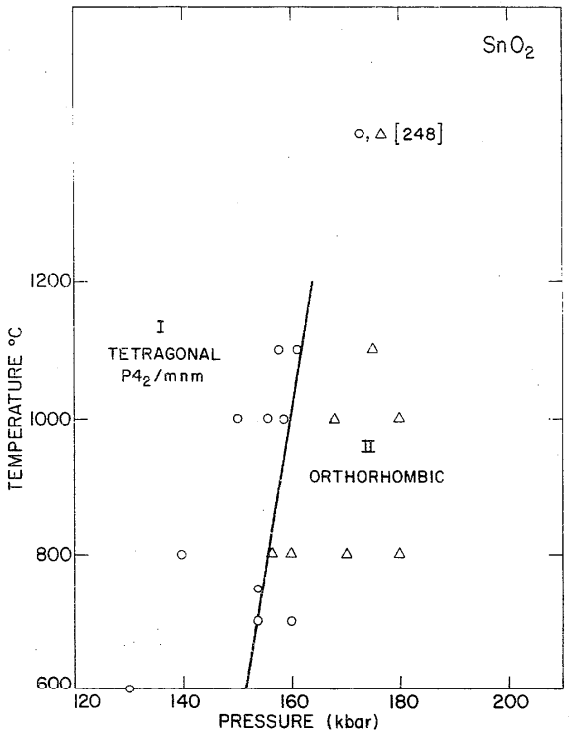

FIGURE 14. Phase diagram for SnO_2.

The paratellurite transition has been studied by a number of investigators and experimental techniques [170,190,191,234,272]. It was first reported by Peercy and Fritz [190] on the basis of Brillouin scattering experiments at pressure. The transition is driven by a pressure dependent transverse acoustic soft mode which decreases smoothly to zero velocity at approximately 9 kbar so it appears to be second order. The phase boundary is very steep with almost negligible temperature dependence. Paratellurite is tetragonal with space group $P4_12_12$ and lattice constants $a = 4.805$ Å, $c = 7.602$ Å and $Z = 4$. The high pressure phase TeO_2(IV) was studied by Worlton and Beyerlein [272] employing neutron diffraction techniques. TeO_2(IV) is orthorhombic with $a = 4.605$ Å, $b = 4.856$ Å, $c = 7.530$ Å and $Z = 4$ at 19.8 kbar. The space group is $P2_12_12_1$ with all atoms in general positions (4a). A phase diagram has not been drawn since the equilibrium relationships of the paratellurite phases to the rutile and brooksite phases is not known.

The best value for the paratellurite TeO_2(III)-TeO_2(IV) transition is 8.86 kbar from the work of Peercy et al. [190]. The relationship of these phases to the other phases of TeO_2 (i.e., TeO_2(I), TeO_2(II)) has not been investigated.

8.14. TiO_2

Titanium dioxide occurs in nature in three polymorphic forms as the minerals rutile, anatase, and brooksite. Rutile is usually considered to be the high temperature and high pressure phase relative to anatase whereas brookite is often considered to be of secondary origin. When subjected to high pressure all of these three phases transform to a crystallographic structure isomorphous to α-PbO_2 [27,86,183,232].

Several studies have been carried out on the TiO_2 polymorphism. Osborn [184] studied the conversion of anatase to rutile in the presence of water from temperatures of 375 to 660 °C and pressures of 1–3 kbar. He found that pressure lowered the transformation temperature. Dachille et al. [86] reported the existence of a new high pressure form of TiO_2 produced from anatase in the region 15–100 kbar and 25–500 °C which was retained metastably at atmospheric pressure. Bendeliani et al. [27] reported that rutile was converted to a high pressure phase with the α-PbO_2 structure at pressures 40–120 kbars and temperatures 700–1500 °C. Simons and Dachille [232] prepared TiO_2(II) from bookite and did a crystal structure analysis from powder x-ray data. McQueen et al. [168] studied the effect of shock waves on rutile and found the new phase after shocks of about 330 kbar. Later hugoniot measurements by Linde and DeCarli [154] give evidence of a phase transition commencing between 150 and 200 kbar. X-ray diffraction studies of recovered specimens showed the presence of an orthorhombic phase with α-PbO_2 structure.

Dachille et al. [86] made a fairly extensive investigation of the phase boundaries in the TiO_2 system. Runs were made using rutile, anatase, and brookite as starting materials. In this study no transitions of rutile to other phases were observed. Similarly, no conversion to brookite was observed when TiO_2(II) was the starting material. As a result of this difficulty and the slow reaction kinetics, these "phase" boundaries do not represent equilibrium conditions [86,87,124].

The crystal structures of the TiO_2 polymorphs are as follows [83]: rutile-tetragonal ($P4_2/mnm$), anastase-Tetragonal ($I4_1/amd$), brookite-orthorhombic (Pbca) and TiO_2(II)-orthorhombic (Pbcn) of the α-PbO_2-type. Crystallographically TiO_2(II) is very similar to brookite in that the b and c axes are nearly the same and $a_{II} = \frac{1}{2}a_{br}$. It should be noted that in both MnF_2 and ZnF_2 the α-PbO_2-type structure was retained upon the release of pressure. In these two compounds the α-PbO_2-type phase was not observed at high pressure but only in the quenched material at atmospheric pressure. Jamieson and Olinger [123] performed x-ray diffraction studies at high pressure and showed that the TiO_2(II) phase was the only one observed, therefore the α-PbO_2-type phase of TiO_2 apparently is a quenched form.

Natural ilmenite (Fe,Mg)TiO_2 has been found to transform to the perovskite structure at 140 kbar and then disproportionate to (Fe,Mg)O plus a cubic phase of TiO_2 at 250 kbar in the temperature range of 1400 to 1800 °C. The cubic TiO_2 can be indexed on the basis of space group Fm3m with $Z = 4$ and $a = 4.455$ Å at room temperature and 1 bar. According to the author's calculations the data fit a fluorite (CaF_2-type) structure best.

In an investigation of post rutile phases for TiO_2, Liu [159] discovered a new phase at approximately 250 kbar syn-

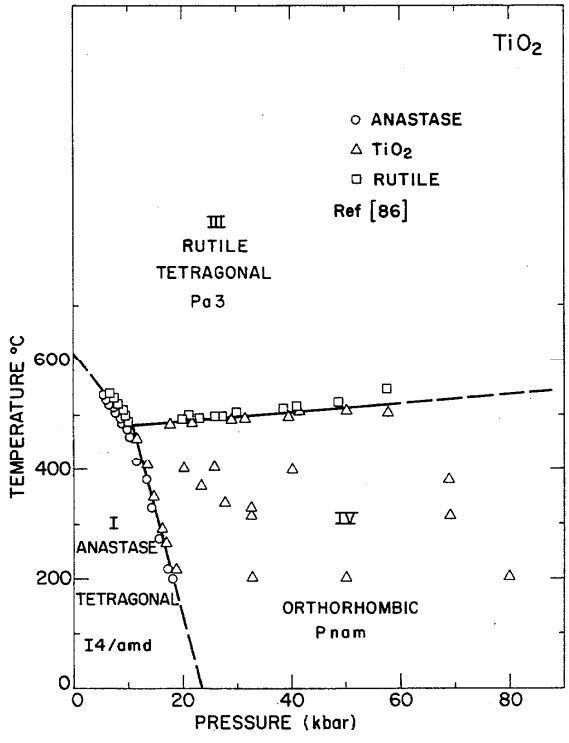

FIGURE 15. Phase diagram for TiO_2 (Anatase).

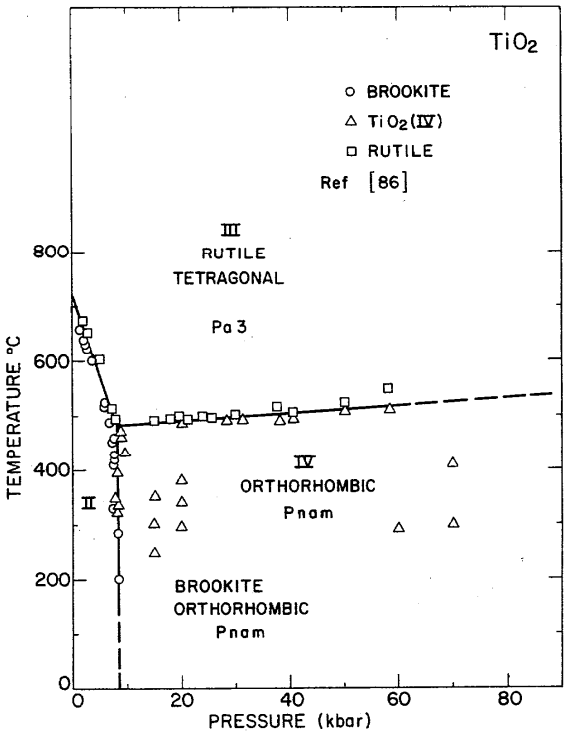

FIGURE 16. Phase diagram for TiO_2 (Brookite).

thesized by laser heating. The diffraction lines were indexed in the hexagonal system with unit cell dimensions $a = 9.22$ Å and $c = 5.685$ Å ($Z = 16$). No known structure can be yet be assigned to this phase. Its density is about 8.5 percent greater than that of the α-PbO_2 phase of TiO_2.

8.15. ZrO_2

The polymorphism of zirconia was first reported by Ruff and Ebert [209]. A reversible phase transformation from the monoclinic to the tetragonal crystal system was found at about 1000 °C. Lynch et al. [161] place the transition between 1193 °C and 1200 °C. Mumpton and Roy [178], using the differential thermal analysis and x-ray diffraction techniques, obtained a monoclinic-tetragonal transition temperature of 1170 °C. Baun [21] showed that the transition starts at 1000 °C and is complete at 1190–1200 °C. All investigators found a large temperature hysteresis in the reverse transformation from tetragonal to monoclinic.

A number of authors have reported observing the metastable retention of the tetragonal phase at room temperature. It is generally assumed that in these experiments the tetragonal phase was stabilized due to impurities. In high pressure experiments Vahldiek et al. [255] were able to retain the tetragonal phase as a mixture with the stable monoclinic phase at room temperature and atmospheric pressure. The tetragonal form of ZrO_2 was prepared at 15 to 20 kbar and 1200 to 1700 °C and retained after rapid quenching. The high pressure specimens when heated to 1200 °C in air reverted to the monoclinic form.

Whitney calculated the pressure-temperature phase boundary for the monoclinic tetragonal equilibrium transformation. The curve has a negative slope and intersects the pressure axis at 36 kbars. Kulcinski [150] studied this transition by x-ray techniques at room temperature. At 38 kbar a new phase attributed to tetragonal ZrO_2 started to appear which at 46 kbar had increased to 50 percent.

Smith and Cline [235] present some evidence for a cubic ZrO_2 phase at temperatures above the tetragonal phase. This is based on the indirect evidence that a cubic phase can be stabilized by such additives as MgO and CaO, and with solid solution series ZrO_2-ThO_2. This phase is assumed to have the fluorite structure.

Bendeliani et al. [27] prepared an orthorhombic phase of ZrO_2 in the interval 40 to 110 kbar and 20 to 1700 °C. The sample was examined after removal from the press and showed a presence of the monoclinic phase. The unit cell data are $a = 5.110$ Å, $b = 5.073$ Å, $c = 5.267$ Å, $\rho_c = 5.99$ g/cm^3, and $Z = 4$. Based upon the observed extinctions in the powder data the space group is assumed to be $P2_12_12_1$. Bendeliani et al. [27] present a tentative phase diagram for ZrO_2 in which the tetragonal, cubic and orthorhombic phases meet a triple point. Using DTA techniques Bocquillon and Susse [37] modify this picture somewhat. Their determinations of the tetragonal orthorhombic phase boundary indicate that it would intersect the monoclinic phase at approximately 600 °C. According to this result the transformation observed by Kulcinski must have been the monoclinic-orthorhombic transition.

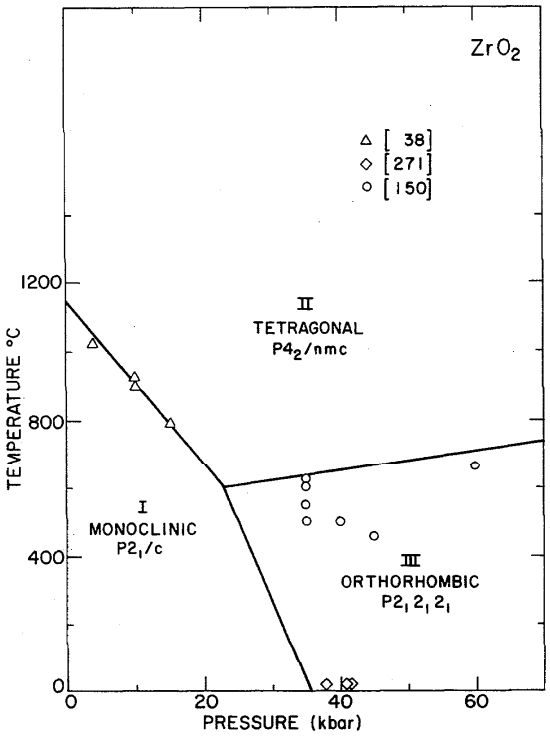

FIGURE 17. Phase diagram for ZrO_2.

8.16. $Zn(OH)_2$

Zinc hydroxide has several modifications at normal pressures, the most stable of which is the α-form whose crystal structure has been examined in detail. This form is orthorhombic with unit cell data $a = 8.53$ Å, $b = 5.16$ Å, $c = 4.92$ Å, $Z = 4$ and the space group is P222. Each Zn atom is surrounded by four OH groups in a distorted tetrahedron. The disposition of the tetrahedra in the structure is similar to that in various SiO_2 modifications with four-fold coordination, but differs in that the OH groups forming the tetrahedron are not in contact because the Zn atom is too large.

For the other modifications of $Zn(OH)_2$ there is only limited x-ray data without detailed analysis of their structures. Another orthorhombic form has the cell dimensions $a = 6.73$ Å, $b = 7.33$ Å and $c = 8.47$ Å with $Z = 8$. A hexagonal form has the dimensions $a = 3.11$ Å and $c = 7.80$ Å. Roy and Mumpton [205] prepared a high pressure form of what the consider to be $Zn(OH)_2$ but could not index the d-spacings to a crystal system.

Baneeva and Popova [11] reported the synthesis of a new CdI_2 form of $Zn(OH)_2$ at pressures of 110–120 kbar and a temperature of 400 °C from α-$Zn(OH)_2$. This transformation represents an increase in coordination from 4 to 6. This structure type is already known for mixed hydroxide $Zn(OH)_2 + Mg(OH)_2$, $Co(OH)_2$ and $Ni(OH)_2$. The hexagonal unit cell data for the new CdI_2-form of $Zn(OH)_2$ are $a = 3.19$ Å, $c = 4.714$ Å, $Z = 1$ and $\rho_c = 3.96$ g/cm^3. This represents an increase in density of 30% over the low pressure phase.

9. Phosphides

9.1. CoP_2

The marcasite and arsenopyrite type structures are exhibited by a large number of transition metal di-pnictides. The marcasite structure is most stable for the iron group dipnictides while the related arsenopyrite type structure has been found for all the cobalt group di-pnictides except CoP_2, $CoBi_2$, and $IrBi_2$. Donohue [93] prepared the arsenopyrite type CoP_2 with the reaction of Co + (Ge) + 2P (Ge used only as a flux) between 800 and 1200 °C at a pressure of 65kbar. The role of the flux in this reaction is not clear, however, without it the new phase could not be synthesized. The structure of the arsenopyrite unit cell is monoclinic with dimensions $a = 5.610$ Å, $b = 5.591$ Å, $c = 5.643$ Å and $\beta = 116.8$ ($Z = 4$).

9.2. GeP_2

In a study of polymorphism in the Ge-P system Osugi et al. [188] report the synthesis of a cubic phase of GeP_2 in the range 1000–1200 °C and 35–40 kbar. Comparison of the x-ray data of the cubic phase of GeP_2 with that for the pyrite phase of SiP_2 show essentially the same d-spacings but significant discrepancies in their relative intensities. In addition, the cubic cell dimension $a = 5.619$ Å for GeP_2 is smaller than that of SiP_2 ($a = 5.682$ Å). This latter phenomenon may be due to non-stoichiometry in GeP_2, however.

9.3. $NbP_{1.7}$

The atmospheric pressure phases in the Nb-P system are NbP and NbP_2. In the pressure range 35–55 kbar a new phase was prepared with the ordered defect PbFCl-type structure having the chemical formula $\sim NbP_{1.7}$ [126a].

The largest crystals of this new compounds were isolated from samples with Nb:P ratios between 2:3 and 1:2. The samples were heated to 1250 °C at a pressure under 55 kbar, held for 2 hours and quenched while still under pressure. Temperatures were measured with a Pt-Pt/Rh thermocouple placed at the surface of the cylindrical graphite heater enclosing the sample. Under ambient conditions $NbP_{1.7}$ can be kept several years without decomposing or oxidizing.

The chemical composition indicated by the synthesis lies between the mono- and diphosphide. Chemical analysis suggested a composition of $NbP_{1.7}$. Its measured density was 5.65 g/cm^3 which corresponds to $NbP_{1.69}$ assuming partial occupancy of P sites and full occupancy of the metal sites.

Initial identification based on powder x-ray patterns suggest unit cell with $a = 3.339$ Å and $c = 7.649$ Å. Precession photographs revealed a superstructure with an a-axis which is five times larger than the a-axis of the PbFCl subcell. All reflections were accounted for by Laue Symmetry 4/mmm and $a = 7.468$ Å, $c = 7.649$ Å.

9.4. SiP_2

Silicon diphosphide was synthesized successfully by halogen transport from the elements [94]. The crystal structure is pyrite-type, space group Pa3 with unit cell dimensions $a = 5.705$ Å, $Z = 4$ and $\rho_c = 3.22$ g/cm^3.

9.5. $VP_{1.75}$

The details of the preparation of the high pressure phase $VP_{1.75}$ are identical to those described for $Nb_{1.7}$. In the V-P system, the stoichiometric compounds VP and VP_2 are the only ones previously known to exist at atmospheric pressure [126a]. $VP_{1.75}$ crystals are black, brittle, and show metallic conductivity.

Powder x-ray diffraction data of the high pressure phase fits a tetragonal cell with $a = 3.162$ Å, $c = 7.267$ Å and $Z = 8$. The chemical formula $VP_{1.75}$ was determined from the crystal structure determination. From this data the calculated density was 4.80 g/cm^3 which is excellent agreement with the measured value of 4.87 g/cm^3.

$VP_{1.75}$ crystallizes with a RbFCl-type subshell space group $P\bar{4}m2$. The superstructure arises from the ordered arrangement of vacancies of the F site of the PbFCl subcell.

9.6. ZnP_2

A high pressure modification of ZnP_2 was prepared by Osugi and Tanaka [189] by the direct reaction of zinc with phosphorous and also through the polymorphic transitions from both the monoclinc and tetragonal ZnP_2 phases. Application of pressures above 20 kbar with temperatures above 150 °C is required for the synthesis. The new modification of ZnP_2 has a pseudo-cubic symmetry with a cell dimension $a = 5.322$ Å and measured density 3.55 g/cm^3.

10. Silicides

In a study of the effect of pressure and temperature on the disilicides MSi_2 of the divalent metals (M = Ca, Sr, Ba, Eu) new polymorphic modifications have been identified for $CaSi_2$ [89,169,230] $SrSi_2$ [101] and $BaSi_2$ [100]. The alkaline earth metals of calcium, strontium, barium and the divalent rare earth metal europium have two outer s-electrons in their atomic ground state. In many of their compounds similar properties and isotypic structures are found. At atmospheric pressure, however, all of the above disilicides crystallize in four different structure types which differ characteristically in their silicon sublattices.

10.1. $BaSi_2$

Barium disilicide at atmospheric pressure crystallizes in an orthorhombic structure, space group Pnma (or $Pna2_1$) with $a = 8.92$ Å, $b = 6.75$ Å, $c = 11.57$ Å and $Z = 8$. A high pressure modification, $BaSi_2$(II), was prepared by heating the normal phase of $BaSi_2$ to 1000 °C at a pressure of 40 kbar. On quenching to ambient conditions the high pressure modification could be stored in the absence of air and moisture for several months. Heating BaSi(II) to 400 °C at 1 bar pressure leads to its complete transformation to the original phase. The structure of the high pressure phase of $BaSi_2$ is rhombohedral, space group $P\bar{3}m1$ with $a = 4.047$ Å, $c = 5.330$ Å and $Z = 1$ [100].

10.2. $CaSi_2$

Calcium discilicide has a hexagonal layer type structure in which the silicon sublattice consists of corrugated layers, each silicon having three equidistance neighbors. $CaSi_2$(I)

has a rhombohedral structura, space group R3m with $a = 3.855$ Å, $c = 30.6$ Å, $Z = 6$ and $\rho_c = 2.46$ g/cm^3. This represents a volume reduction of 6.9 percent.

$CaSi_2$(II), a high pressure polymorph, was obtained from rhombohedral $CaSi_2$(I) in the region 17 to 87 kbar and 700 to 1800 °C. For complete conversion to the high pressure phase in short periods of time, pressures above 40 kbar and temperatures above 1000 °C are required simultaneously [101]. The structure of the high pressure phase is body centered tetragonal, α-$ThSi_2$-type, space group $I4_1/amd$ with $a = 4.283$ Å, $c = 13.54$ Å and a calculated density of 2.57 g/cm^3. $CaSi_2$(II) is superconducting at 1.58 ± 0.01 K [169].

10.3. $EuSi_2$

Europium disilicide crystallizes in the body center tetragonal structure [100] identical to those adopted by the high pressure forms of both $CaSi_2$ and $SrSi_2$. High pressure and high temperature treatment failed to yield any structure transformations in $EuSi_2$.

10.4. $SrSi_2$

Strontium disilicide ($SrSi_2$-type) is cubic ($a = 6.355$ Å) with silicon atoms forming a three dimensional network. All silicon atoms have three equidistant neighbors in flat trigonal pyramids but twisted against each other. The high pressure phase, $SrSi_2$(II), also has the α-$ThSi_2$-type structure identical to $CaSi_2$(II). The tetragonal unit cell dimensions are $a = 4.438$ Å, $c = 13.89$ Å with a calculated density of 3.51 g/cm^3. This represents a volume reduction by 1.9 percent [100].

11. Sulfides

11.1. Ag_2S

The phase diagram of Ag_2S contains four solid phases, three of which are known at atmospheric pressure and are listed in Table 1. High argentite, the high temperature form of Ag_2S, is stable above 596 °C up to the melting point at 825 °C. The argentite modification, which has a disordered b.c.c. structure, is stable between 177 and 596 °C. The room temperature form Ag_2S(II), known as acanthite, is stable below 177 °C. It crystallizes in a monoclinic unit cell with space group $P2_1/n$.

The first high pressure study on Ag_2S was a determination of Ag_2S(III) (acathite)-Ag_2S(IV) phase boundary between 82 and 200 °C [52]. The transition is associated with a very small volume change. The Ag_2S(II)-Ag_2S(III) solid-solid phase boundary was determined up to the triple point at approximately 12.3 kbar and 195 °C. From the triple point the Ag_2S(II)-Ag_2S(IV) boundary was extended up to 40 kbar [76]. Previously, the initial slope of the Ag_2S(II)-Ag_2S(III) had been determined up to 1.2 kbar with an initial slope of 4 °C/kbar which appears to be too high [207].

In the work of Clark and Rapoport [76] pressures were generated in a piston cylinder device and phase transitions were detected by means of differential thermal analysis with chromel-alumel thermocouples. Corrections were made for the effect of pressure on the thermocouples [116,117]. Each point on the phase boundary is based upon four separate determinations on different samples with precision of ± 2 °C. Corrected pressures are stated to be accurate to ± 0.5 kbar. Unfortunately, Bridgman's Ag_2S(III)-Ag_2S(IV) phase boundary does not extrapolate to the present triple point (see figure 18 for phase diagram of Ag_2S).

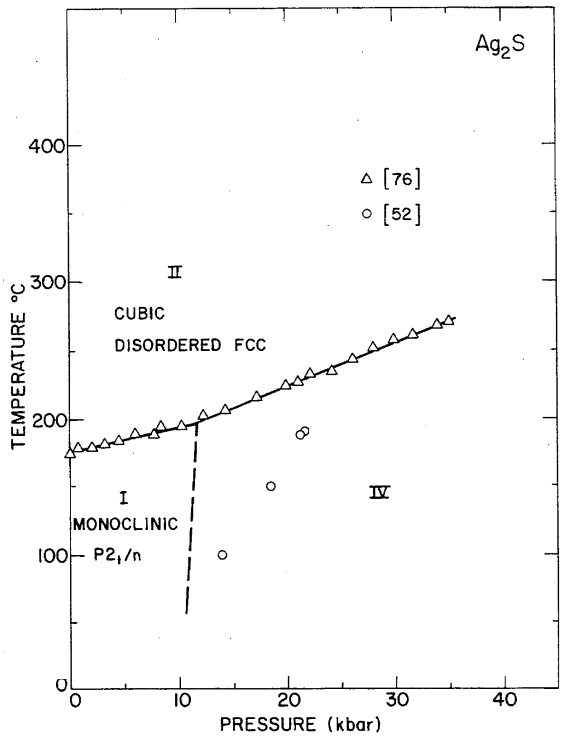

FIGURE 18. Phase diagram for Ag_2S.

11.2. BiS_2

The preparation of a new polymorph BiS_2 was reported by Silverman [230]. The new material was synthesized at 50 kbar and 1250 °C from a 4:11 atomic mixture of Bi and S, each a purity greater than 99%. The x-ray examination was inconclusive about the crystal system. The published d-values are 3.11 Å(100), 2.97 Å(60), 2.62 Å(65), 2.27 Å(60), 1.88 Å(70), 1.81 Å(70) and 1.504 Å(60).

11.3. CS_2

The earliest pressure studies of CS_2 were by Bridgman [53] who investigated the melting curve and compression up to 35 kbar. At temperatures of 175° or over and at pressures above 45 kbar, CS_2 is transformed slowly and irreversibly into a black solid which is retained under atmospheric conditions. Bridgman suggested that black CS_2 had a structure analagous to SiO_2. Whalley [266] did an infrared study of solid CS_2 prepared at 55 kbar and 185 °C and found a major absorption in this substance at 1063 ± 5 cm^{-1}. He assigned this to C = S stretching and suggested a linear polymetric structure containing $-\overset{S}{\overset{\|}{C}}-S$ units. Other absorptions were much weaker than the 1063 cm^{-1} bond. This conclusion was also confirmed by Silverman and Soulen [226].

More detailed examinations of the phase diagram by Butcher et al. [58,9] revealed that the formation of black CS_2 occurs over a wide range of pressure but over a relatively narrow range of temperature. Above this temperature it decomposes to carbon and sulfur. When heated at atmospheric pressure, black CS_2 softens at about 70 °C and decomposes to carbon and sulfur. It is also insoluble in normal laboratory solvents.

X-ray patterns of black CS_2 are broad and diffuse indicating little or no long range order. At room temperature this material has a very low electrical conductivity which increases rapidly with temperature giving an energy gap of 1.15 eV.

Two x-ray studies have been performed on single crystals of CS_2 grown from the melt. The structure determined by Baenziger and Duax [10] is based on an orthorhombic unit cell with space group Cmca and $Z = 4$ at 143 K. The unit cell constants at two different temperatures 158 K and 98 K are $a = 6.455$ Å(6.215 Å), $b = 5.596$ Å(5.404 Å) and $c = 8.939$ Å(9.208 Å). The melting point of CS_2 is 160 K. In this structure the CS_2 molecules are linear S-C-S.

Carbon disulfide freezes at 12.6 kbar at room temperature. The high pressure crystal structure was investigated by Weir et al. [263] and and is in agreement with that of Baenziger and Duax [10]. The unit cell dimensions of the orthorhombic cell are $a = 6.16$ Å, $b = 5.38$ Å, and $c = 8.53$ Å. It is of interest to note that with decreasing temperature at 1 bar pressure, c increases from 8.939 Å(158 K) to 9.280 Å(98 K). This value appears to decrease with pressure, however. Weir et al. [263] also reported observing an abrupt transition in a single crystal of CS_2 in the vicinity of 30 kbar and − 30 °C.

11.4. CdS_2

Pyrite-type CdS_2 [33] was prepared from the reaction of CdS or amorphous cadmium polysulfide and sulfur at 65 kbar and 400–600 °C. Investigation of the various powder samples by x-ray diffraction showed that all had the pyrite structure with the same unit cell size suggesting a uniform stoichiometry.

11.5. Cu_2S

The polymorphic behavior of Cu_2S is quite complex. In a study of the Cu-S system at high temperature the compounds Cu_2S, $Cu_{1.96}S$ and $Cu_{1.8}S$ (digenite) have been identified as the products of sintering. All three of these compounds undergo high temperature phase transitions at 1 bar. In Cu_2S the Cu_2S(IV)-Cu_2S(III) phase transition occurs at 103.5 °C. The initial slope of this phase boundary is 0.5 °C/kbar [76]. At about 10 kbar new DTA signals were obtained around 240 °C and a new transition line followed up to about 40 kbar. DTA signals from the original Cu_2S(IV)-Cu_2S(III) phase boundary disappeared just above 10 kbar. On decreasing pressure, this behavior is reversed and at 8 kbar the DTA signals from the upper transition disappear and those corresponding to the lower boundary reappear. The upper transition line varies only slightly with pressure and has a shallow maximum in the vicinity of 245 °C and 21 kbar.

Serebyanaya [222] reported that $Cu_{1.96}S$ could be prepared by heating Cu_2S to 900 °C. Clark and Rapoport [76],

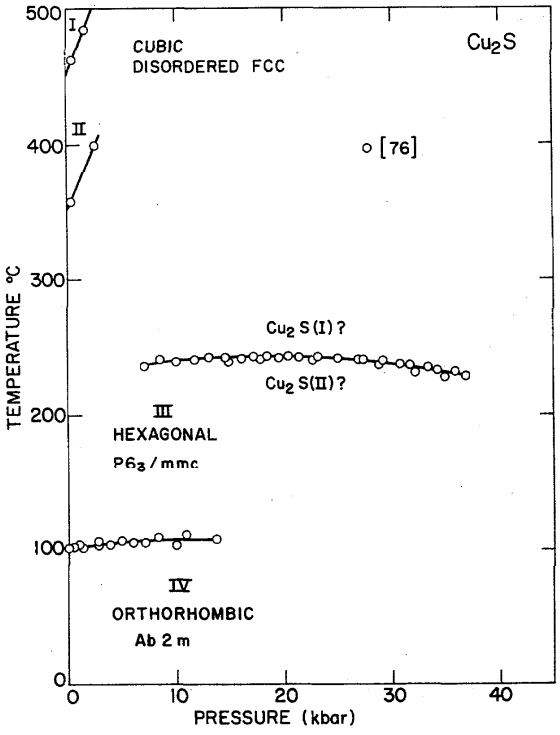

FIGURE 19. Phase diagram for Cu_2S.

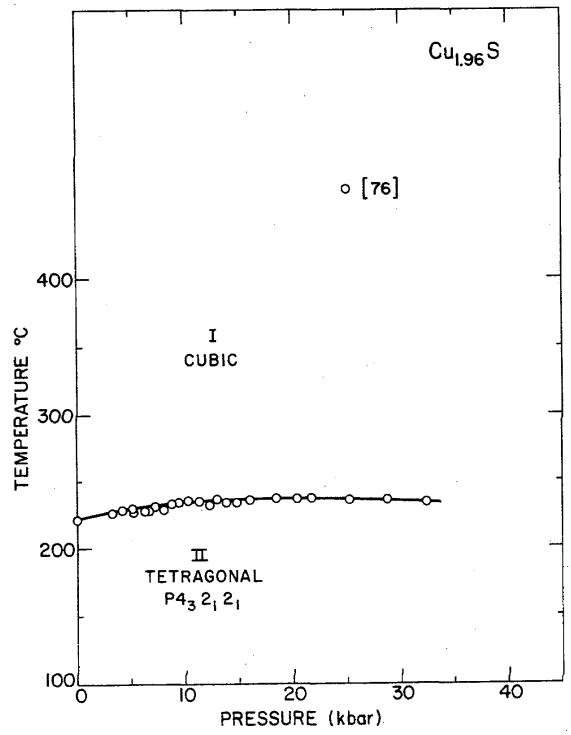

FIGURE 20. Phase diagram for $Cu_{1.96}S$.

therefore, heated their Cu_2S sample to approximately 850 °C and below 10 kbar there was no evidence of the transition around 103.5°, whereas in the region 220–230 °C DTA signals were obtained. Clark and Rapoport [76] reported that the upper transition results from the reversible formation of Cu_9S_5 (or Cu_7S_4) by a disproportionation reaction of Cu_2S (See figures 19 and 20 for the phase diagrams of Cu_2S and $Cu_{1.96}S$, respectively).

11.6. CuS_2

The synthesis of CuS_2 was carried out in a belt apparatus [178a] using a graphite heater and sodium chloride as the pressure transmitting medium. The cell was calibrated at the following fixed points: Bismuth (25.5 kbar; 27 kbar) and Barium (58 kbar). Temperatures were determined from a Pt-Pt10Rh thermocouple present during the runs.

The reaction was carried out with a mixture of CuS(covellite) and sulfur in a 1:1.2 mole ratio at high temperature and high pressure. Chemical analysis of the product, a dark purplish red material, indicated the composition $CuS_{1.9}$ and x-ray analysis confirmed that it had the cubic (NiS_2) pyrite structure with the unit cell dimension $a = 5.796$ Å. The calculated density is 4.44 g/cm^3 and the measured density is 4.24 g/cm^3. Bither et al. [32] reported $a = 5.790$ Å, $\rho_c = 4.368$ g/cm^3 and $\rho_{exp} = 4.354$ g/cm^3. Between 200–300 °C in an inert atmosphere CuS_2 decomposes to covellite, digenite, and sulfur. Between 400–475 °C the products further decompose to Cu_2S (chalcocite) and sulfur.

11.7. GeS_2

The synthesis of the tetragonal high pressure form of GeS_2 was investigated by Prewitt and Young [1981]. Single crystals were prepared from stoichiometric ratios of germanium and sulfur held at 1100 °C and 65 kbar for 2–3 hours and then temperature quenched. The tetragonal unit cell dimensions are $a = 5.480$ Å, $c = 9.143$ Å with $Z = 4$ and $\rho_c = 3.30$ g/cm^3 (space group-$I\bar{4}2d$).

The structure of GeS_2(II) is similar to SiS_2(II) and consists of GeS_4 tetrahedra which share vertices to form 3 dimensional networks. GeS_2(I) also has a structure in which the GeS_4 tetrahedra share vertices. Germanium atoms of GeS_2(II) are in positions 4a (0,0,0) while sulfur occupies positions 8d ($x = 0.238$; $y = 0.25$; $z = 0.125$).

11.8. H_2S

The atmospheric pressure phase transitions in H_2S were first observed by Giauque and Blue [112]. Their specific heat measurements indicated the following transitions: boiling point 212.8 K; melting point 187.6 K; H_2S(I)-H_2S(II) solid-solid transition at 126.2 K and the H_2S(II)-H_2S(III) solid-solid transition at 103.6 K. The measurements indicated a first order transition at 103.6 K and an anomaly occurs at 126.2 K, which is characteristic of a second order transition.

Pressure studies on the H_2S phase diagram were performed by Stevenson who employed volumetric techniques. This work extended to a maximum pressure of 10 kbar. Stevenson [240] detected two new high pressure phases H_2S(V) and H_2S(VI) in the region above 5 and 6 kbars, respectively. In a later study by Stewart [241] these latter two phases were not confirmed. Babb [9] measured the melting curve of H_2S and reported a new solid phase H_2S(IV) which meets H_2S(I) and H_2S(L) in a triple point at −26 °C and 3.6 kbar (see figure 21 for H_2S phase diagram).

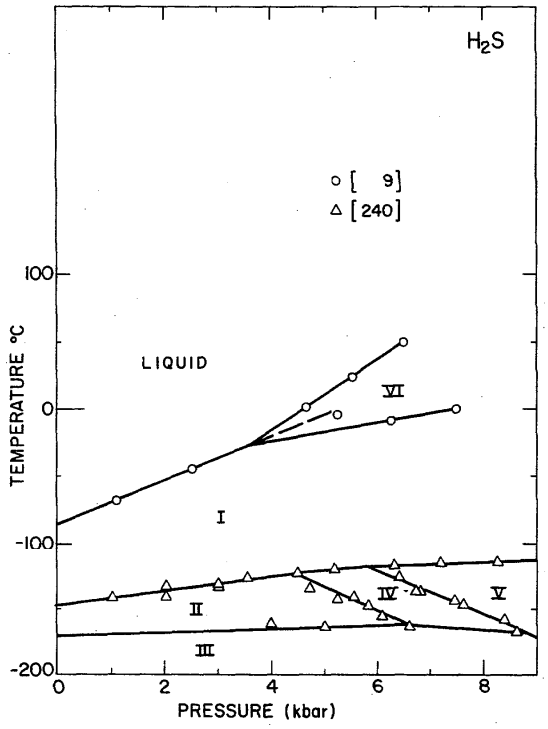

FIGURE 21. Phase diagram for H_2S.

The x-ray diffraction studies of Justi and Nitka [128] indicate that the sulfur atoms in all three phases occupy a face-centered cubic lattic which changes less than 1% in lattice constant between 20 and 150 K. The transitions apparently arise from the variation in the positions of the hydrogen atoms. H_2S(III) is ordered while H_2S(I) and H_2S(II) are disordered. The basic cubic structure is quite open so that rearrangements of hydrogen atoms are possible without appreciable changes in lattice constant. There is no crystallographic data for H_2S(IV) nor the questionable phases H_2S(V) and H_2S(VI).

11.9. IrS_2

At atmospheric pressure iridium is known to combine with sulfur to form iridium disulfide having the orthorhombic structure of iridium diselenide. The pyrite structure, space group Pa3, is in general a densely packed arrangement and tends to be favored when synthesis is attempted between transition metals and groups Va and VIa elements at high pressure. Munson [179] reported the synthesis of a new pyrite phase $IrS_{1.9}$ prepared from a 2:1 mole ratio of sulfur and iridium. The mixture was subjected to 1500 °C at a pressure of 60 kbar. The unit cell dimension of the pyrite-type cell of $IrS_{1.9}$ is $a = 5.68$ Å.

11.10. MoS_2

Bridgman [54] measured the electrical resistance of molybdenite MoS_2 at room temperature up to 100 kbar pressure. The sample, a cleaved single crystal specimen, exhibited reversible electrical resistance discontinuity (drop by a factor of 2.77) at approximately 20 kbar. This result is based upon one run. The crystal structure of MoS_2 is three layered rhombohedral, 3R-MoS_2.

11.11. NbS_2

Niobium disulfide forms two principal phases under normal conditions, one a two layered hexagonal and the other a three layered rhombohedral modification designated 2H-NbS_2 and 3R-NbS_2, respectively. The coordination number of Niobium is 6 but the locations of the sulfur atoms are the corners of a trigonal prism as opposed to octahedral coordination. High pressure synthesis [151] employed stoichiometric mixtures of the niobium and sulfur subjected to a pressure of 90 kbar and various temperatures up to a maximum of 1350 °C. Calibration of the pressure cell was based on the fixed points in bismuth taken at 25.4, 27, and 89 kbar; tin 113–115 kbar.

Below 600 °C there was no reaction, while between 600 and 800 °C a mixture of phases appeared of which the composition and structure could not be identified. In the range 800 to 1000 °C 3R-NbS_2 was formed and from 100 to 1200 °C both 3R-NbS_2 and 2H-NbS_2 were present in the samples. Above 1200 °C a new high pressure form designated NbS_2(II) was synthesized. On the basis of powder x-ray data NbS_2(II) is a new 4 layered hexagonal polytype indexed on the basis of 4H-$NbSe_2$ but with a different space group. The unit cell parameters are $a = 3.33$ Å, $c = 23.8$ Å ($c/a = 4.18$). On the basis of the intensity data, NbS_2(II) appears to be isostructural with 4H-$TaSe_2$ which has the space group $P6_3/mmc$. The atomic coordinates were refined by trial and error to a residual of 0.216. In contrast to trigonal prismatic coordination for the 3R- and 2H-polytypes of NbS_2, the high pressure polytype (4H-NbS_2) of NbS_2(II) has a mixed coordination scheme consisting of both trigonal prismatic and octahedral coordination. NbS_2(II) is stable in air but annealing in a vacuum for 10 hours produces a transformation to the 3R-polytype.

NbS_2(II) has a superconducting transition at 2.9 K. Each of the polytypes 2H-, 3R- and 4H- of NbS_2 exhibit superconductivity.

11.12. PbS_2

Silverman [231] reported the preparation of two high pressure phases of PbS_2. Only the monosulfide had been previously known. A hexagonal CdI_2-type PbS_2 was prepared by reacting PbS + S in the 1:2 ratio at 20 kbar and 1600–1800 °C. The only successful synthesis carried out was with excess sulfur present. The hexagonal CdI_2-type unit cell of PbS_2(I) has the dimensions $a = 3.89$ Å and $c = 5.91$ Å ($Z = 4$).

The other phase PbS_2(II) was prepared from a reaction of the Pb:3S elemental mixture at 45 kbar and 1500 °C held for 5 minutes. PbS_2(II) can be indexed as tetragonal with a KN_3-type structure. The unit cell dimensions are $a = 6.10$ Å and $c = 7.48$ Å ($Z = 4$).

11.13. PdS_4

An orthorhombic palladium disulfide may be prepared by heating palladium dichloride and an excess of sulfur in an evacuated quartz tube for 4 days. The structure of PdS_2 prepared in this manner is space group Pbca ($a = 5.46$ Å, $b = 5.54$ Å, $c = 7.53$ Å) and is closely related to the pyrite structure which places the cation in a nearly perfect octahedral environment. Munson and Kasper (180) prepared a second orthorhombic form of PdS_2 ($a = 5.51$ Å, $b = 5.56$ Å, $c = 7.16$ Å) by reacting a mixture of the elements of PdS_2(I) at 1450 °C and 63 kbar for 5 minutes. PdS_2(II) decomposes to PdS and sulfur at 250–300 °C.

The x-ray data of PdS_2 indicates that PdS_2(II) is very similar to PdS_2(I). Both are derived from the pyrite structure by an elongation of the c-axis. However, the elongation of PdS_2(II) is not as great as that of PdS_2(I). The measured and calculated density of PdS_2(II) is 4.92 g/cm^3 and 5.17 g/cm^3 respectively. PdS_2(II) is not superconducting as is PdS_2(I).

11.14. SiS_2

The synthesis of a high pressure polymorph of SiS_2 has been reported in two separate studies. The first synthesis reported by Silverman and Soulen [230] consisted of a 1Si:2.2S mixture which was subjected to a temperature of 1480 °C at 75 kbar for a duration of 2 minutes. On the basis of x-ray powder patterns SiS_2(II) was indexed in the tetragonal crystal system with $a = 5.43$ Å and $c = 8.67$ Å. Measured and calculated densities for SiS_2(II) are 2.23 g/cm^3 and 2.40 g/cm^3, respectively, compared with 2.05 g/cm^3 calculated for SiS_2(I). A contemporary study of the silicon-sulfur system by Prewitt and Young (198) reported the synthesis of single crystals of SiS_2(II). The structure of SiS_2(II) consists of SiS_4 tetrahedra which share vertices to form three dimensional networks as compared to SiS_2(I) which contains chains of SiS_4 tetrahedra in which the tetrahedra in each chain shares edges. In this work the unit cell dimensions are $a = 5.420$ Å, $c = 8.718$ Å and $Z = 4$. Measured and calculated densities are 2.40 and 2.37 g/cm^3, respectively. The space group of SiS_2(II) is $I\bar{4}2d$. Silicon atoms occupy position 4a (0,0,0) while sulfur occupies positions 8d ($x = 0.227$; $y = 0.25$; $z = 0.125$).

11.15. SrS_2

Polycrystalline SrS_2 was synthesized under normal pressure by Lutz [162,163] who only published d-values with no crystal or structural data. Single crystal SrS_2 was prepared by Kawada et al. [139] by heating a sulphur excess mixture of SrS and S up to 900 °C at a pressure of 20 kbar. SrS_2 is tetragonal (I4/mcm) with $a = 6.095$ Å, $c = 7.616$ Å, $Z = 4$ and $\rho_{exp} = 3.56$ g/cm^3. The structure is isotypic with that of the $CuAl_2$ group intermetallic compounds.

11.16. ZnS_2

Pyrite type ZnS_2 [33] mixed with some unreacted starting materials was obtained as a bright yellow microscopic

powder by the reaction of ZnS + S at 65 kbar for 4–6 hours at 400–600 °C followed by a rapid quench to room temperature. X-ray diffraction powder patterns of all the ZnS_2 compositions prepared showed all samples having the same unit cell size $a = 5.9542$ Å, indicative of ZnS_2 stoichiometry.

11.17. Rare Earth Sulfides

The rare earth disulfides series has been investigated by a number of researchers. Only the disulfides at the lower end of the series can be synthesized at atmospheric pressure. Bilitz [31] reported the synthesis of LaS_2 and CeS_2. Flahaut et al. [104] reported that the disulfides of La, Ce, Pr, Nd, and Sm all had the same "cubic" structure. They also reported the synthesis of the sulfides of Eu, Gd, Dy, and Y which were all nonstoichiometric and having the tetragonal structure. Ring and Tecotzky [202] reported the synthesis of the tetragonal disulfides of Tb, Ho, and Er.

The tetragonal disculfide has the LaS_2 type structure, space group P4/nmm and is related to the $ErSe_2$ subcell [206] by the relation $a(LaS_2) = 2a(ErSe_2)$ and $c = (LaS_2) = c(ErSe_2)$. The cubic rare earth disulfide structure was indexed on the basis of the close resemblance of its x-ray pattern to that of the tetragonal rare earth disulfide. Both of these structures are assumed to be composed of 4 $ErSe_2$-type subcells.

On the basis of single crystal data Marcon and Pascard [166] have shown that $CeSe_2$ and CeS_2 both have a monoclinic structure which is pseudotetragonal and can also be viewed as pseudocubic. It is composed of 2 Fe_2As-type subcells. This apparently bears close resemblance to the structure of the "cubic" LaS_2 which is based upon 4 $ErSe_2$ subcells since the $ErSe_2$ subcell has the same structure as Fe_2As.

With the use of high pressure techniques Webb and Hall [262] were able to synthesize rare earth disulfides for the heavier region of the series. Tetragonal rare earth disulfides (P4/nmm) were prepared for Tm, Yb, and Lu. New polymorphs having the apparent cubic "LaS_2"-type structure were prepared for Gd, Tb, Dy, Ho, Er, Tm, Yb, Lu, and Y. In this work the identification of the "cubic" and tetragonal phases was based solely upon powder x-ray diffraction data. A few of the weak superlattice reflections could not be indexed either on the basis of the subcell or supercell (figs. 22, 23, and 24).

Eliseev et al. [99] also synthesized the ytterbium disulfide at high pressure. X-ray examination confirmed the existence of two phases whose line positions were in good agreement with the work of Webb and Hall [262]. The phase of YbS_2 which Webb and Hall [262] indexed as cubic was indexed as tetragonal Fe_2As-type Eliseev et al. By refining atomic positions, using an absorption correction and assuming a definciency of sulfur, they were able to fit the data to $YbS_{1.7}$ with a least squares residual of 0.17 (powder data).

One important fact not mentioned in the literature in that the $ErSe_2$-type subcell is identical to the Fe_2As-type cell. In all the studies cited in reference to the "cubic" rare earth disulfides one (CeS_2) was based upon single crystal data. All structure determinations and attempts to index powder data were based upon the Fe_2As-type unit cell of subcell. Eliseev et al. did not publish their d-values but attempts to fit the

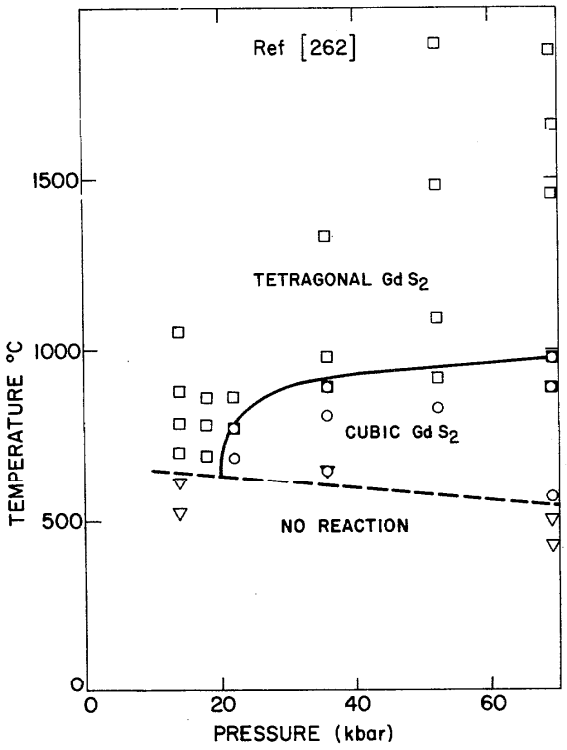

FIGURE 22. Reaction product diagram for Gd + 2S.

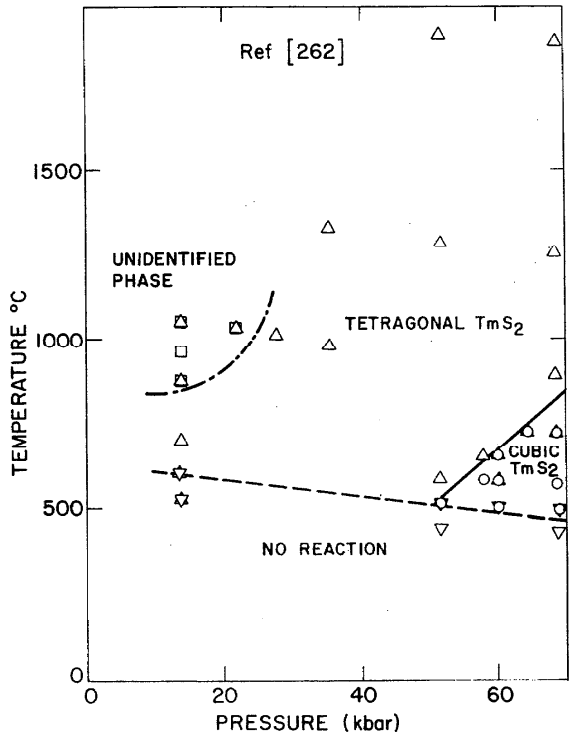

FIGURE 23. Reaction product diagram for Tm + 2S.

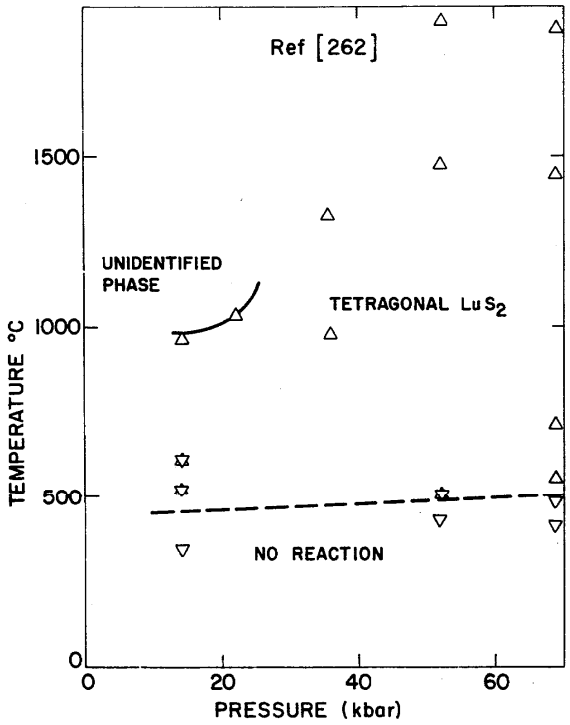

FIGURE 24. Reaction product diagram for Lu + 2S.

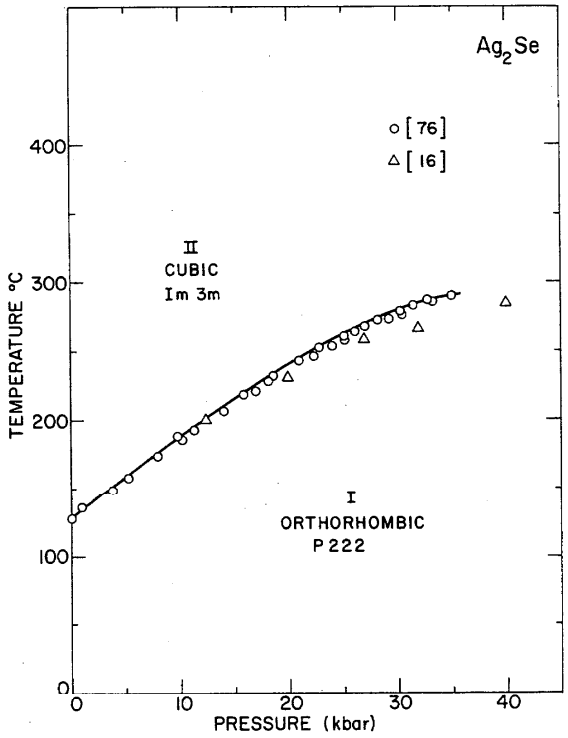

FIGURE 25. Phase diagram for Ag_2Se.

"cubic" data of Webb and Hall [262] with their lattice parameters left 5 of the cubic lines unindexed. In addition to these lines, Webb and Hall [262] mentioned that they were unable to index 3 lines in their "cubic" YbS_2 pattern. It is felt that the work of Eliseev is no more definitive than that of Webb and Hall [262] other than all data seem to point to the view that the Fe_2As-type subcell is basic to the true YbS_2 structure. Certainly further investigation is needed on these compounds.

12. Selenides

12.1. Ag_2Se

The Ag_2Se(I)-Ag_2Se(II) or commonly known α-β phase boundary has been investigated up to the region of 50 kbar and 300 °C. At atmospheric pressure a sharp change in resistivity occurs when Ag_2Se is transformed from the low temperature orthorhombic (α-Ag_2Se) to the high temperature body centered cubic form (β-Ag_2Se). This method was employed by Banus [16] to determine the pressure dependence of the phase boundary up to 47 kbar. The samples were polycrystalline and the pressure cells were calibrated with the Bi I-II (25.4 kbar) and the Tl I-II (37 kbar) transitions. The transition temperatures were taken on increasing temperature cycle. The type of thermocouple or information about any thermocouple correction and calibration was not discussed. Up to about 15 kbar the sign of the temperature coefficient of resistivity is negative for α-Ag_2Se and positive for β-Ag_2Se. Above 15 kbar the temperature coefficient of resistivity for both phases. Room temperature x-ray patterns showed no phase change up to 45 kbar.

The Ag_2Se (α-β) phase boundary was also studied by Clark and Rapoport [76] up to a pressure of 40 kbar and a temperature of 300 °C by differential thermal analysis. The agreement of this work with Banus (16) is good up to 20 kbars but beyond this, temperatures differ by as much as 15–20 °C. Banus noted temperature hysteresis as high as 15–25 °C while the maximum reported by Clark and Rapoport was 3 °C. As a result of better reproducibility and the additional temperature calibration details, the curve of Clark and Rapoport is considered more accurate (see fig. 25 for Ag_2Se phase diagram).

Using the value $dT/dP = 7.0$ °C/kbar reported by Roy et al., Banus [16] determined the heat of transformation as $\Delta H_t = 2.19$ kcal/mol. Taking the most recent value of $dT/dP = 6.02$ °C/kbar, then $\Delta H_t = 2.54$ kcal/mol. The calculated values of ΔH_t range from 1.61 to 2.54 kcal/mol. The high uncertainty arises from the uncertainty in ΔV_t and $dT/dP|_{p=0}$.

12.2. $BiSe_2$

Bismuth diselenide was prepared by the reaction of a 1:2.2 atomic ratio of Bi:Se at a pressure of 45 kbar and 1280 °C [229]. The $BiSe_2$ crystals were black and are stable in water, aqueous ammonia and HCl at room temperature but reacts vigorously with concentrated HNO_3. At 275 °C $BiSe_2$ converts to Bi_2Se_3. X-ray powder patterns of $BiSe_2$ contained over 60 lines and have not been indexed.

12.3. Cu_2Se

The atmospheric pressure high temperature phase transition in Cu_2Se was originally reported to occur at 110 °C

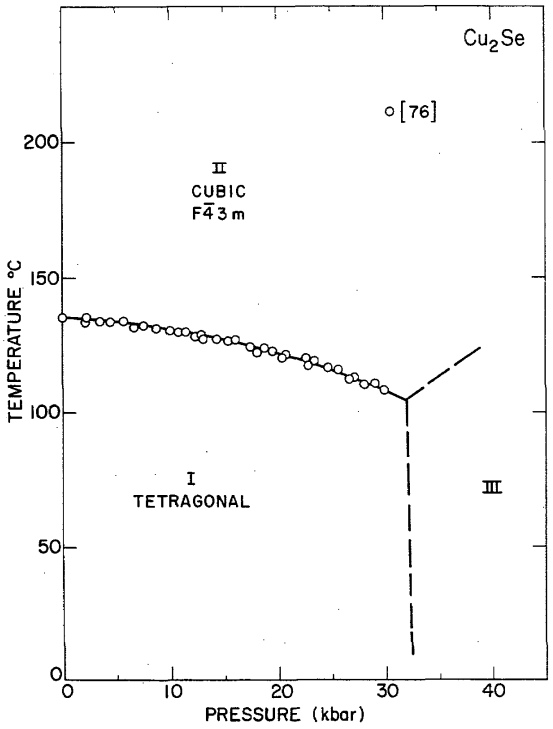

FIGURE 26. Phase diagram for Cu_2Se.

[107,142]. Data published by Clark and Rapoport [76] place the transition at 135 °C. This latter result is attributed to the high purity of the sample. Clark and Rapoport followed the Cu_2Se(I) Cu_2Se(II) phase boundary up to 30 kbar where the DTA signals disappeared completely. This behavior was reversible and repeated from run to run. A thorough search at pressures up to 41 kbar failed to give any indication of additional phase transitions. Clark and Rapoport postulate that in the 30 kbar region the Cu_2Se(I)-Cu_2Se(II) phase boundary has a negative slope with $dT/dP = -0.6$ °C/kbar (fig. 26).

It is impossible to prepare Cu_2Se of stoichiometric composition. The unit cell dimension of the cubic phase decreases considerably with copper deficiency.

Cu_2Se(II) which is the high temperature phase, has a disordered cubic structure with the unit cell dimension $a = 5.840$ Å at 170 °C. The room temperature phase is orthorhombic.

12.4. $MoSe_2$

A three-layer rhombohedral (3R) polytype of $MoSe_2$ isostructural with rhombohedral MoS_2 is formed from 2H-$MoSe_2$ at high pressures and high temperatures [253]. The region in which 3R-$MoSe_2$ is formed is above 30–40 kbar and above 1400 °C. The unit cell dimensions of 3R-$MoSe_2$ are $a = 3.292$ Å and $c = 19.392$ Å.

12.5. $NbSe_2$

Niobium diselenide forms three principal phases under normal conditions, a two layered hexagonal structure (2H-$NbSe_2$), a three layered rhombohedral structure (3H-$NbSe_2$) and a four layered hexagonal structure ($4H_p$-$NbSe_2$). The cation coordination is all a six fold trigonal prismatic type as previously discussed for NbS_2. Synthesis conditions are the same as discussed for NbS_2.

The following reaction products were formed [151]: (a) below 600 °C there was no reaction, (b) between 600 and 1000 °C $NbSe_4$ + Nb was formed, (c) between 1000 and 1200 °C 2H-$NbSe_2$ was synthesized and (d) above 1200 °C $NbSe_2$(II), a high pressure phase was obtained. $NbSe_2$(II) consists of a hexagonal 4 layered cell ($4H_0$-$NbSe_2$) isostructural to NbS_2(II). It should be noted that there are now two 4H-polytypes in $NbSe_2$. For the $4H_p$-$NbSe_2$ polytype the cation coordination is of trigonal prismatic type while the $4H_0$-$NbSe_2$ polytype has octahedral cation coordination. The hexagonal unit cell dimensions are $a = 3.46$ Å, $c = 24.8$ Å, $c/a = 4.18$. The space group is $P6_3/mmc$ with the atoms in the positions: 2Nb(1) in 2(a), 2Nb(2) in 2(b), 4Se(1) in 4(f) and 4Se(2) in 4(f). All four modifications of $NbSe_2$ are superconducting with the indicated critical superconducting transition temperatures.

2H-$NbSe_2$	7.0 K
3R-$NbSe_2$	
$4H_p$-$NbSe_2$	6.3 K
$4H_0$-$NbSe_2$	3.5 K

12.6. $PbSe_2$

$PbSe_2$ which previously had not been prepared in crystalline form was synthesized by Silverman [231]. Thus successful synthesis employed a mixture of PbSe + 2Se with excess selenium which was subjected to temperatures between 600 and 2400 °C at pressures from 20–70 kbar. This crystalline form of $PbSe_2$ has the tetragonal KN_3-type structure with unit cell dimensions $a = 6.36$ Å and $c = 7.63$ Å. Electrical resistance measurements with increasing pressure from 10–70 kbar showed no significant change.

12.7. PbSSe

The mixed lead dichalcogenide PbSSe which was previously unknown in crystalline form was synthesized by high pressure techniques [231]. The tetragonal KN_3-type structure was prepared by reacting PbS + PbSe + 2S + 2Se at temperatures between 600 and 2400 °C and pressures in the range 20–70 kbar. The unit cell dimensions of KN_3-type PbSSe are $a = 6.27$ Å and $c = 7.57$ Å with $Z = 4$ and $\rho_c = 7.15$ g/cm^3.

12.8. $SmSe_2$

$SmSe_2$ was prepared from a stoichiometric ratio of the elements at a pressure of 80 kbar in the temperature range 1200 to 2000 °C. The $SmSe_2$ sample gave a single phase x-ray powder pattern which indexed to a tetragonal structure with $a = 4.100$ Å and $c = 8.275$ Å. The density calculated from these unit cell dimensions is 7.32 g/cm^3 and the measured density is 7.23 g/cm^3 [13].

12.9. Transition Metal Selenides

Transition metal dichalcogenides of Mn, Fe, Co, Ni, Cd, and Cu have been reported to occur in CdI_2, marcasite,

or pyrite type structures. For a specific composition the density of the transition metal dichalcogenide increases in the order CdI_2 < marcasite < pyrite. Several of these MX_2 compounds do not occur normally with the pyrite type structure. Since the pyrite modification is the most dense structure-type, then one would expect that high pressure and high temperature would induce the transformation marcasite of CdI_2→pyrite.

Bither et al. [32,33,34] reported the synthesis of three series of compounds: CuSSe, $CuSe_2$; $FeSe_2$; and $CdSe_2$, $ZnSe_2$ all with the pyrite structure. These compounds were prepared from stoichiometric ratios of the elements reacted at 65 kbar and 1000–1200 °C for 1–3 hours. This was followed by a slow cool to 400 °C and a quench to room temperature.

The copper dichalcogenides with one unpaired d-electron show metallic conductivity and superconductivity with critical temperatures ranging from 1.3 to 2.4 K. $FeSe_2$ is a semiconductor.

12.10. Rare Earth Selenides

The rare earth diselenides of the elements from lanthanum through gadolinium with the exception of Eu were synthesized by Benacerraf et al. [25]. Wang and Steinfink [260] synthesized the compounds of La, Ce, Nd, Gd, Dy, Ho, and Er and attempted the synthesis of $YbSe_2$. Kafalas and Finn [134] reported the synthesis of Samarium polyselenide of varying composition ($SmSe_{1.9}$ to $SmSe_{2.03}$) at 40 kbar and 600 °C.

Webb and Hall [261] reported the synthesis of $TmSe_2$, $YbSe_2$, and $LuSe_2$ in the pressure range 14–70 kbar and temperature range of 400–1900 °C. These compounds crystallize in the $ErSe_2$ ($LaTe_2$-type) structure (fig. 27).

Several different studies have been made of the x-ray crystallography. Eliseev and Kuznetsov [98] reported that $NdSe_{1.9}$ was isostructural with $LaTe_2$ which has the tetragonal space group P4/nmm. Wang and Steinfink [260] studied $ErSe_2$ and found it to have a tetragonal subcell of the P4/nmm space group from the strong reflections, but a number of weak reflections which were not observed for $LaSe_2$ and $CeSe_2$. The indexing of these reflections was accomplished on the basis of an orthorhombic supercell composed of 24 tetragonal subcells. Refinement of the structure was accomplished for the subcell but could not be achieved for the supercell. Marcom and Pascarel [166] reported that $CeSe_2$ is monoclinic with the $P2_1/a$ space group and a pseudo tetragonal structure. Due to the lack of refinement for the supercell of $ErSe_2$ and the lack of weak supercell reflections in $CeSe_2$, the high pressure phases $TmSe_2$, $YbSe_2$ and $LuSe_2$ have been indexed on the basis of the tetragonal subcell. A number of weak lines consequently do not fit in this indexing scheme.

13. Tellurides

13.1. Ag_2Te

The pressure-temperature phase diagram of Ag_2Te (fig. 28) is fairly complicated and has at least three known atmospheric pressure solid phases from room temperature up to the melting point. The high pressure-high temperature region of Ag_2Te was first investigated by Banus and Finn [17] in the range up to 25 kbar and 250 °C. They employed a combination of techniques: electrical resistivity, differential

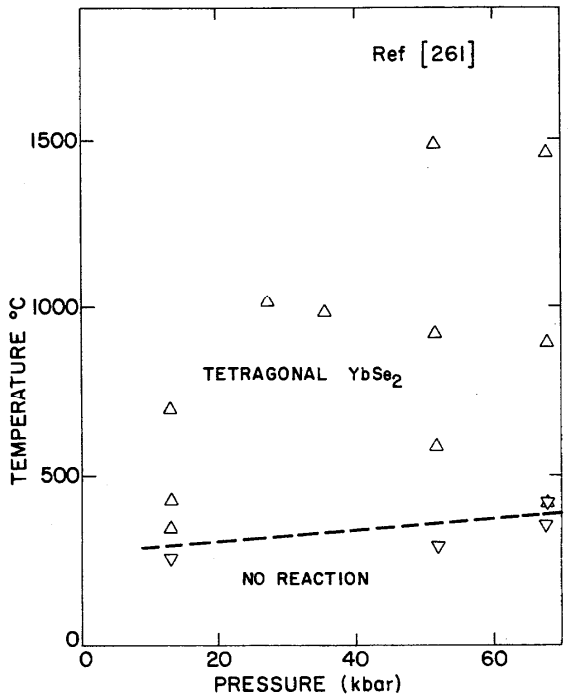

FIGURE 27. Phase diagram for $YbSe_2$.

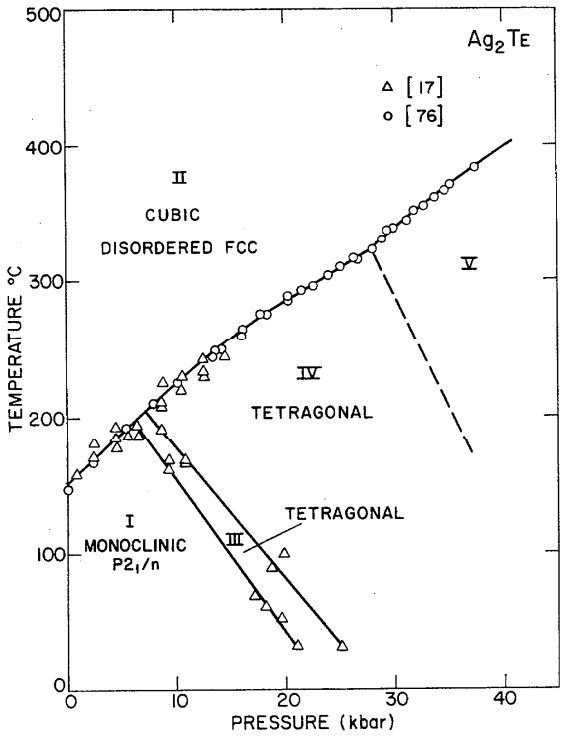

FIGURE 28. Phase diagram for Ag_2Te.

thermal analysis and x-ray diffraction analysis at high pressure.

The Ag_2Te(II)-Ag_2Te(III) boundary was determined by a combination of electrical resistivity and DTA measurements. In the electrical resistivity measurements at approximately 8 kbar an abrupt increase in the slope of the phase boundary was noted which suggested the presence of a triple point. Room temperature resistivity measurements confirmed the new phase boundary at a pressure of 22–25 kbar. The resistivity pressure trace showed a sharp increase at 22.5 kbar and an abrupt drop at 25 kbar confirming the existence of two separate but closely spaced polymorphic transitions. Quasi hydrostatic resistance measurements to 90 kbar duplicated the resistivity trace at 22.5 and 25 kbar. Above 26 kbar the resistivity increased slowly by about 15 percent to a maximum between 44 and 48 kbar and gradually decreased by approximately 20 percent to 90 kbar. The high pressure phases were both indexed as tetragonal on the basis of in situ powder x-ray diffraction data. The proposed unit cells appear to be identical based upon the cell parameters but relative intensities of corresponding lines in the two x-ray patterns do not agree.

Clark and Rapoport [76] extended the study of Banus and Finn [17] up to 40 kbar and 400 °C. In the region of 30 kbar and 325 °C there was a slight upward change in the curvature of the phase boundary which is an indication of a new triple point and a new high temperature high pressure phase region. In these measurements the temperature hysteresis was 4 °C between Ag_2Te(II)-Ag_2Te(III). Along the Ag_2Te(II)-Ag_2Te(V) boundary the hysteresis increased to 20 °C and along the proposed Ag_2Te(II)-Ag_2Te(VI) boundary it reduced to about 12 °C. This behavior is no doubt characteristic of the different phase regions. In the region where the measurements overlap, the data of Clark and Rapoport [76] are considered more accurate due to the significantly lower hysteresis.

13.2. $AuTe_2$

$AuTe_2$ exists in nature in two different crystallographic forms, the monoclinic mineral calaverite and the orthorhombic mineral krennerite. Adams and Davis [2] reported a pressure induced polymorphic transition in calaverite at 20 $\pm$ 2 kbar. The x-ray data were collected at high pressure resulting in only 4 diffraction peaks. The authors reported two different possible tetragonal unit cells of density 9.94 and 10.74.

The associated unit cell dimensions are $a = 5.25$ Å, $c = 5.48$ Å and $a = 6.13$ Å, $c = 3.72$ Å, respectively. Correlation with a known structure type was not successful and it is recommended that this transition be re-examined in a diamond anvil pressure cell.

13.3. Transition Metal Tellurides

Transition metal dichalcogenides of Mn, Fe, Co, Ni, and Cu have been reported to occur in CdI_2, marcasite, or pyrite structures. Several of these compounds do not normally occur with the pyrite type structure. Since the pyrite modification is the most dense structure-type then one would expect that high pressure and high temperature would induce the transformation from marcasite or CdI_2 to pyrite.

Bither et al. [32,33] reported the synthesis of two series of compounds: CuSeTe, $CuTe_2$ and $FeTe_2$, $CoTe_2$, $NiTe_2$ all with the pyrite structure. These compounds were prepared from stoichiometric ratios of the elements reacted at 65 kbar and 1000–1200 °C for 1–3 hours. This was followed by a slow cool to 400 °C and a quench to room temperature.

The copper dichalcogenides with one unpaired d-electron show metallic conductivity and superconductivity with critical temperatures ranging from 1.3 to 2.4 K. $FeTe_2$ ($a = 6.29$ Å), $CoTe_2$ ($a = 6.310$ Å), and $NiTe_2$ ($a = 6.374$ Å) are all metallic.

13.4. Rare Earth Tellurides

Compounds of the type RTE_{2-x} ($0 \leqslant x \leqslant 0.3$) have been reported for the rare earth component R = La, Ce, Pr, Nd, Sm, Gd, Tb, Dy, and Yb. These RTe_{2-x} compounds are isomorphous having a tetragonal structure with space group P4/nmm. Since the Te is more compressible than R, high pressure should favor the synthesis of RTe_{2-x} for the smaller end of the series where R = Ho, Er, Rm, and Lu.

Cannon and Hall [60] reported the successful synthesis of these RTe_{2-x} (R = Y, Ho, Er, Tm, Lu) compounds with maximum pressures ranging from 3 to 26 kbar. Increasing pressure is required with increasing atomic number of the rare earth component to form the polymorphs. Synthesis occurred over a fairly broad range of temperature from 450 up to 1500 °C (fig. 29).

Each of the RTe_{2-x} compounds is silver in appearance and unstable. X-ray data showed no decomposition in 15 days but complete decomposition after 80 days. When heat-

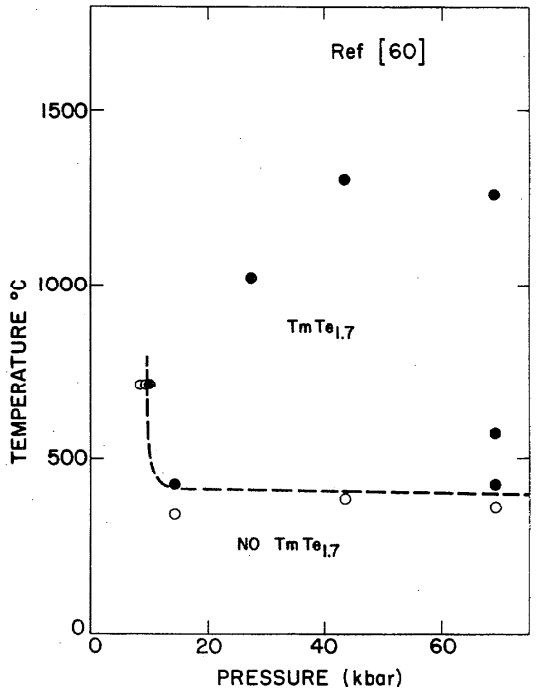

FIGURE 29. Reaction Product diagram for Tm + 1.7Te.

ed in a vacuum $HoTe_{2-x}$ remained stable to 260 °C but decomposed at 340 °C. X-ray studies have shown that these new compounds are isostructural to their lower molecular weight analogs.

14. Mixed Cation Transition Metal Dichalcogenides

Numerous ternary mixed cation transition metal dichalcogenides of the composition $M_xM'_{1-x}Y_2$ (M,M' = Zn, Cd, Cu, Ni, Mn, Fe) with the pyrite structure have been synthesized by Birther et al. [34].

14.1. $Zn_xMn_{1-x}Y_2$

Pyrite-type phases were prepared for $Zn_xMn_{1-x}Y_2$ for $x = 0.35$, 0.53, and 0.70. Reactants of the following molar ratios were used: 0.5ZnS/1.5MnS/2.5S, ZnS/MnS/2.5S, and 1.5ZnS/0.5MnS/2.5S, respectively. The reactions were carried out at 65 kbar and 100 °C for 1 hour followed by a 5 hour cool to 875 °C and quenched to room temperature. The products obtained from these reactions were dark red single crystals with the approximate formula $Zn_{0.7}Mn_{0.3}S_2$.

Black crystals of $Zn_{0.5}Mn_{0.5}Se_2$ having the pyrite-type structure were prepared from a reaction of 0.5Zn/0.5Mn/2.2Se at 65 kbar and 800 °C for 1 hour followed by a 2 hour cool to 700 °C and quenched to room temperature. In the telluride system, $Zn_{0.5}Mn_{0.5}Te_2$ was synthesized from 0.5Zn/0.5Mn/2Te at 65 kbar and 800 °C for 2 hours. The product was a mixture comprising red crystals of ZnTe adjoined by silver crystals. X-ray examination confirmed the pyrite-type structure for the silver crystalline material.

The $Zn_xMn_{1-x}Y_2$ compounds are semiconductors with low activation energies. As x ranges from 0 to 1, the unit cell dimension decreases and the crystals range in magnetic properties from antiferromagnetic to diamagnetic.

14.2. $Cd_xMn_{1-x}Y_2$

The phase relations involved in the formation of the pyrite-type Cd-Mn dichalcogenide appear to be more complex than those of the analogous Zn-Mn systems and only the selenide was obtained in single crystal form suitable for characterization. Synthesis of the Cd-Mn sulfides gave a mixture of phases that comprise (a) pyrite-type $Cd_{0.35}Mn_{0.65}S_2$ ($a = 6.176$ Å), (b) a rock salt type $Cd_{0.5}Mn_{0.5}S$ ($a = 5.340$ Å) and (c) a wurtzite type $Cd_{0.5}Mn_{0.5}S$ ($a = 4.07$ Å, $c = 6.62$ Å). With the same starting materials and slightly different reaction conditions the product contained pyrite-type $Cd_{0.6}Mn_{0.4}S_2$ ($a = 6.228$ Å) as the main phase mixed with α-MnS and (Mn,Cd)S products as previously described. In the Cd-Mn selenide system high pressure synthesis also resulted in a mixture of phases in the product containing red-brown crystals of wurtzite (Cd,Mn)Se ($a = 4.21$ Å, $c = 6.94$ Å) and black crystals having the pyrite-type structure with composition $Cd_{0.45}Mn_{0.55}Se_2$. Excess Se was also present. Reaction of (Cd,Mn)Te at high pressure gave a product comprising (a) the pyrite-type and (b) sphalerite-type (Cd,Mn)Te plus unreacted Te. The phases could not be separated for characterization.

14.3. $Zn_xCd_{1-x}Y_2$

Reaction of equimolar amounts of ZnS/CdS plus excess sulfur at 65 kbar gave a phase mixture comprising (a) pyrite-type $Zn_xCd_{1-x}S_2$, with (b) unreacted ZnS and CdS. By varying the reaction temperature, cooling rate and quench temperature compositions ranging from $x = 0.5$ to $x = 0.71$ were analyzed. Comparable reactions of Zn/Cd/4Se at 65 kbar gave a microcrystalline product consisting of a mixture of phases comprising (a) ZnSe, (b) CdSe, (c) unreacted Se and (c) $Zn_xCd_{1-x}Se_2$ (with x ranging from 0.32 to 0.45). The pyrite-type phases had very high electrical resistances in agreement with the semiconducting properties of their end members.

14.4. $Zn_xCu_{1-x}Y_2$

High pressure synthesis of the Zn-Cu disulfides and diselenides have been achieved over the entire range $x = 0$ to $x = 1$. The $Zn_xCu_{1-x}Y_2$ compounds are metallic and those with $x < 0.2$ are superconductors.

14.5. $Cd_xCu_{1-x}Y_2$

Reaction of 0.1 CdS_x (amorphous)/0.9CdS/S at 65 kbar and 700 °C yields a purple microcrystalline product of the pyrite type structure for which $x = 0.04$. Similar reactions for the selenide system result in composition for which $x = 0.04$ to 0.06.

14.6. $Mn_xCu_{1-x}Y_2$

Pyrite type $Mn_xCu_{1-x}S_2$ compounds were obtained with compositions ranging from $x = 0.01$–0.08. In the selenide and telluride systems the compounds $Mn_{0.55}Cu_{0.45}Se_2$ and $Mn_{0.65}Cu_{0.35}Te_2$, respectively, were synthesized at 65 kbar and 800 °C. The $Mn_xCu_{1-x}Y_2$ compounds are metallic.

14.7. $Cu_xFe_{1-x}S_2$

Pyrite-type compounds of $Cu_xFe_{1-x}S_2$ were synthesized for a narrow range in composition ($x = 0.73$–0.84) suggesting an approximate composition Cu_3FeS_8. On the basis of microcrystalline samples, qualitative measurements indicated metallic conductivity. A broad superconducting transition was observed to occur below 1.7 K.

14.8. $Ni_xFe_{1-x}Y_2$

$(Ni,Fe)S_2$ has been prepared at high pressure with $x = 0.76$ ($x = 5.702$ Å). The analogous pyrite-type diselenides have been prepared with compositions $x = 0.4$–0.6 ($a = 5.525$ Å–5.890 Å). These Ni-Fe dichalcogenides are metallic conductors.

14.9. $Cr_xCo_{1-x}S_2$

The pyrite-type compound CoS_2 is ferromagnetic. Solid solutions of CoS_2, FeS_2, and NiS_2 have been prepared at atmospheric pressure but CrS_2 was unknown. By the use of high pressure-high temperature reactions Donohue et al. [92a] found that it was possible to replace some of the Co in CoS_2 with Cr so as to produce pyrite-type solid solutions

$Cr_xCo_{1-x}S_2$. The new pyrite phases $Cr_xCo_{1-x}S_2$ ($0 < x < 0.4$) were prepared at 65 kbar and 1100–1200 °C held for about 2 hours. Magnetic measurements indicate that the saturation magnetization decreases while the Curie temperature increases dramatically with increasing x. T_c reaches a maximum above temperature at $x \sim 0.30$. The cubic (pyrite-type) unit cell dimension varies from 5.535 Å for $x = 0$ to 5.558 for $x = 0.39$.

15. Alloy and Intermetallic Compounds

15.1. AuX_2 (X = Al,Ga,In)

Gold forms intermetallic compounds of the AB_2 type with Al, Ga, and In having the cubic fluorite structure. Upon melting, these compounds undergo a volume contraction, which is an indication of a negative slope in the fusion curve. In the region of the melting curve minimum one should, therefore, find a triple point and at least one high pressure modification (figs. 30, 31 and 32).

The melting curves for $AuAl_2$, $AuGa_2$ and $AuIn_2$ were measured by differential thermal analysis by Storm et al. [246] in the range up to 50 kbar. The experiments were carried out in the belt press and piston-cylinder type apparatus. Either Chromel alumel (Cr-Al) or Pt, Pt-Rh thermocouples were used depending on the temperature range being covered; however, no correction was made for the pressure effect on the thermal emf. The belt apparatus was calibrated to the transitions in Bi(I-II) at 25.4 kbar, Tl(II-III) at 37 kbar and Ba(I-II) at 58.4 kbar at room temperature as standards.

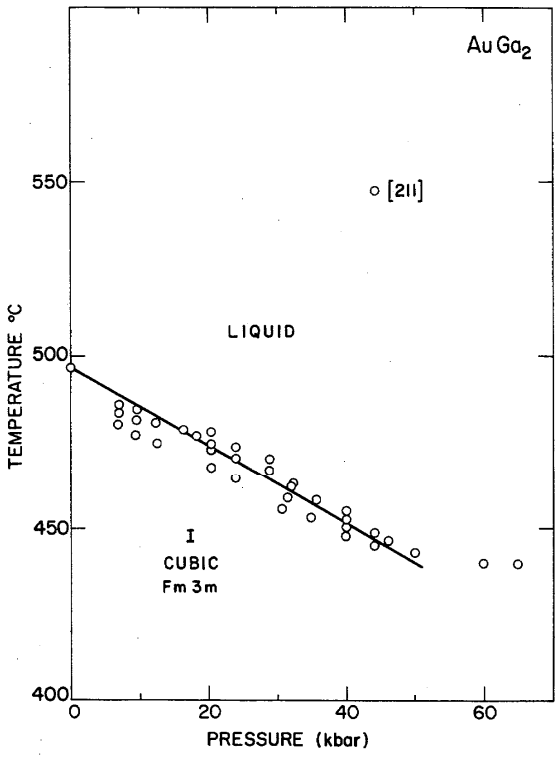

FIGURE 31. Melting curve for $AuGa_2$.

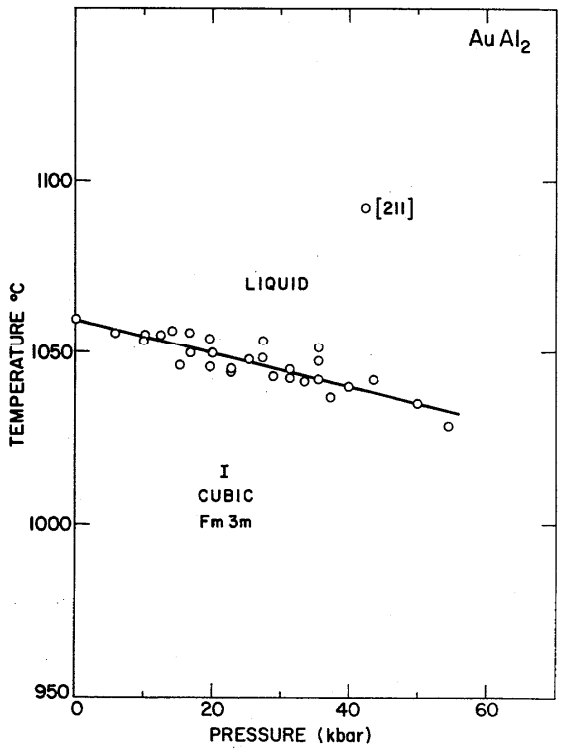

FIGURE 30. Melting curve for $AuAl_2$.

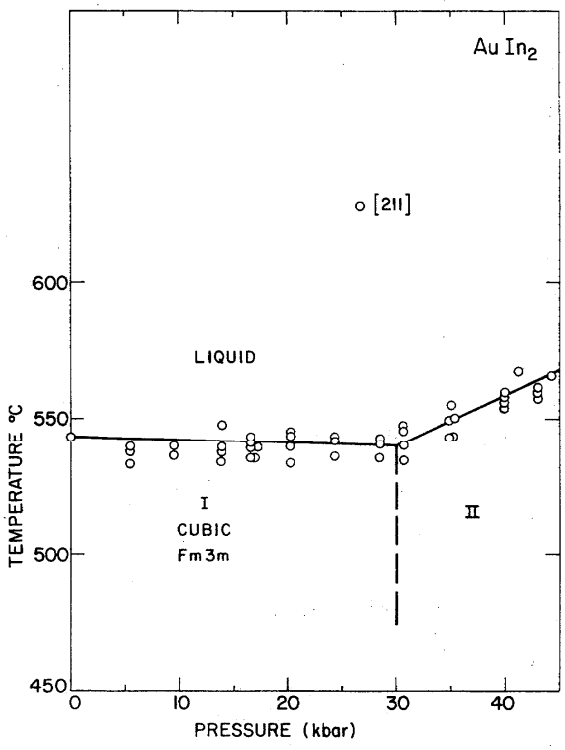

FIGURE 32. Melting curve for $AuIn_2$.

No correction was made for effect of high temperature on the internal pressure on the sample. The stated accuracies are ± 2 kbar up to 40 kbar, ± 3 kbar above 40 kbar for pressures and ± 2 °C for temperature. These values are overly optimistic since the spread of the data points has an average range of 17 °C for $AuAl_2$ and 12 °C for $AuGa_2$ and $AuIn_2$. Due to the scatter of the data the best fit will be assumed to follow the central tendency of the data points.

The melting curves all initially decrease with increasing pressure but only one, $AuIn_2$, shows a triple point at the minimum at about 30 kbar and 542 °C. Above 30 kbar the melting curve has a positive slope. There have been no reported attempts to determine the $AuIn_2$(I)-$AuIn_2$(II) phase boundary or determine the $AuIn_2$(II) crystal system.

15.2. $LaCo_2$

The rare earth cobalt RCo_2 series of compounds crystallize in the face centered cubic $MgCu_2$-type structure. Attempts to synthesize $LaCo_2$ at atmospheric pressure were unsuccessful. Using high pressure techniques Robertson et al. [204] were able to synthesize $LaCo_2$ in the range from 10 to 65 kbar and 1050 to 1350 °C. By x-ray diffraction techniques it was verified that $LaCo_2$ produced at high pressure and high temperature has the cubic $MgCu_2$-type structure with a unit cell parameter $a = 7.449$ Å.

15.3. Magnesium Compounds

The dimagnesium compounds Mg_2X (X = Si, Ge, Sn) crystallize in the cubic antifluorite structure when prepared at atmospheric pressure conditions [73]. Several researchers have studied various aspects of these compounds at high pressure. Cannon and Conlin [67] reported the existence of a new high pressure modification in each of these compounds. The new high pressure polymorphs Mg_2Si(II) and Mg_2Ge(II) were indexed as hexagonal with unit cell dimensions $a = 7.20$ Å, $= 8.12$ Å; and $a = 7.2$ Å, $c = 8.24$ Å, respectively, while Mg_2Sn was indexed as a different hexagonal cell with $a = 13.09$ Å and $c = 13.44$ Å. These investigators were unable to assign any structure to these new polymorphs.

The next important investigation was that of Seifert [219]. In this work the metastable high pressure phases for Mg_2X (X = Si, Ge, Sn) were synthesized at 65 kbar and 600–1000 °C. They were indexed in the orthorhombic system with a suggested Ni_2Si-type (anti $PbCl_2$-type) structure. The range of the a/b ratio is 0.755 to 0.772 and c/b ratio is 1.384 to 1.462 for the new polymorphs. This is in very good agreement with $a/b = 0.746$ and $c/b = 1.412$ for the Ni_2Si structure suggesting that this is a plausible structure and that the high pressure phases are probably isostructural to one another.

Dyuzheva et al. [95a] also examined the structure of Mg_2Sn(II) and demonstrated that the high pressure phase produced at room temperature and 30 kbar is identically the same as the metastable quenched product which was produced at simultaneous high pressure and high temperature.

Dyuzheva et al. [95a] obtained substantially better quality x-ray patterns for Mg_2Sn(II) than the previous investigators and noted that some of their intensities did not agree with the Ni_2-Si-type structure. It was noted that some of the discrepancies were the absence of extinctions required by space group Pnma and the presence of extra reflections not allowed. The structure proposed by Dyuzheva et al. [95a] is a distortion of the Ni_2Si-type structure indexed as hexagonal with $a = 13.18$ Å and $c = 6.99$ Å with $Z = 15$. The authors stated that the experimentally measured density of Mg_2Sn(II) was 4.1 g/cm^3 and upon this basis determined the number of molecules per unit cell as 15. The calculated density for the proposed hexagonal unit cell of Mg_2Sn(II) is 6.19 g/cm^3 if it contains 15 molecular units which represents a 72 percent increase in the density over that of the atmospheric pressure phase. If one were to select the number of molecules based upon the calculated density and retain the hexagonal indexing, then $Z = 9$ would yield a density of 3.71 g/cm^3 and $Z = 12$ gives a density of 4.95 g/cm^3 which amounts to a 3 percent and 37 percent density increase, respectively, over the atmospheric pressure phase. Neither of these values is in good agreeement with the measured density. For the present report the orthorhombic Ni_2Si-type cell of Seifert [219] is considered the best selection for the structures of Ng_2Si(II), Mg_2Ge(II), and Mg_2Sn(II) on the basis of currently available experimental data. The x-ray data for these structures need to be re-examined by an independent investigator.

15.4. Rare Earth Iron Compounds

The lanthanide compounds with the formula RFe_2 has been studied by a number of investigators. The known compounds in this series are isomorphic with the $MgCu_2$-type structure, $Z = 8$, space group Fd3m. In this series attempts to synthesize $LaFe_2$, $PrFe_2$, $NdFe_2$, $EuFe_2$ and $YbFe_2$ by high temperature methods alone have been unsuccessful. Of this group, $PrFe_2$, $NdFe_2$ and $YbFe_2$ were successfully synthesized in the $MgCu_2$-type by Cannon et al., [61] at high pressure. Pressures and temperatures of 90 kbar and 1350 °C failed to produce a similar reaction in La-Fe.

This work indicates that increasing pressure is required for a successful synthesis as the size of the lanthanide component increases suggesting that the size effect is primarily responsible for the previous failures in preparing $PrFe_2$, $NdFe_2$ and $LaFe_2$. Gschneidner and others have suggested that the failure to form certain lanthanide compounds is due to 4f bonding effects. The compounds $LaFe_2$, $PrFe_2$, and $NdFe_2$ have the largest 4f bonding contribution of any of these compounds. However, it is also postulated that pressure increases 4f character and on this basis would tend to impede the function of these compounds contrary to what is observed. It is evident that this behavior is more complex than can be attributed to size effect alone but in this case and several others already discussed the size effect appears to be the major factor.

15.5. Rare Earth Manganese Compounds

The rare earth dimanganese compounds undergo a change in crystal structure as the size of the rare earth component varies. At atmospheric pressure both the light and heavy rare earths form RMn_2 compounds in the $MgZn_2$ (C14) Laves structure while the intermediate rare earths form RMn_2 compounds in the $MgCu_2$ (C15) Laves structure.

By application of high pressure simultaneously with

high temperature Eatough and Hall [97a] prepared the $MgZn_2$-type structure for the dimanganides of Gd, Tb, Dy, Ho, and Y which were previously known only in the $MgCu_2$-type structure. $YbMn_2$ which was previously unknown was also synthesized. Synthesis of the $MgZn_2$-type rare earth dimanganide phases were carried out in the range 1300 to 1400 °C and at pressures ranging from 20 to 50 kbar for the series of compounds $HoMn_2$ through $SmMn_2$, respectively. Of interest was the synthesis of $SmNn_2$ which had reportedly been synthesized in both phases at atmospheric pressure but required a minimum pressure of 50 kbar in this work [97a].

Laves phases of AB_2-type compounds are known with radius ratios $r(A)/r(B)$ varying from 1.05 to 1.68. Since all rare earth dimanganides fall within this range, the existence of structural transitions from hexagonal ($MgZn_2$-type) to cubic ($MgCu_2$-type) and back to hexagonal as the size of the rare earth element decreases is indicative that other effects besides radius ratios must be more important in the determination of which Laves structure is stable in this series [97a].

15.6. $MnAu_2$

The intermetallic compound $MnAu_2$ has a body centered tetragonal unit cell with the CaC_2 (C11) type structure with $a = 3.363$ Å, $c = 8.592$ Å, $Z = 2$ and $\rho_c = 15.33$ g/cm^3. Neutron diffraction investigations have established that the distribution of magnetic moments in $MnAu_2$ is helicoidal. These atoms lie in planes perpendicular to the c-axis of the tetragonal unit cell. Ferromagnetic ordering is observed within such planes. A magnetic field above a threshold value H_c destroys the helicoidal arrangement and produces ferromagnetic ordering. Grazhdankina and Rodinov [113] investigated the electrical and galvanomagnetic properties of this compound over a wide range of pressures. They determined the pressure dependence of the magnetic transition temperature $dT/dP = 0.68°$/kbar and that the critical threshold value H_c decreased linearly with increasing pressure. In an extension of this work Adiatullin and Fakidov [3] found that at 12.5 kbar and 296 K (11.5 kbar at 77 K) the threshold value of the field decreased rapidly to zero. Thus at 12.5 kbar $MnAu_2$ undergoes a transition to the ferromagnetic state at zero field. The transition varies little with temperature. The pressure induced zero field transition in $MnAu_2$ was also confirmed by a sudden drop in the electrical resistance trace at high pressure.

15.7. $NdRu_2$

Synthesis of the hexagonal $MgZn_2$-type structure of $NdRu_2$ at high pressures and high temperatures was reported by Cannon et al. [62]. Powdered samples of Nd:Ru in the ratio of 1:2 were reacted at 1300 °C and 88 kbar. Below 78 kbar the cubic $MgCu_2$-type structure could be prepared while between 78 and 88 kbar both the cubic $MgCu_2$- and hexagonal $MgZn_2$-type phases were formed. Above 88 kbar only the hexagonal phase is synthesized.

15.8. $SmRu_2$

The di-ruthenum compound $SmRu_2$ crystallizes in the cubic $MgCu_2$-type structure when prepared at atmospheric pressure. In the rare earth di-ruthenium series, compounds involving the lowest atomic number rare earth elements crystallize in the $MgCu_2$-type structure while those with the higher atomic number rare earth adopt the hexagonal $MgZn_2$-type structure. Since the rare earth element is more compressible than ruthenium, pressure should cause the radius ratio $r(Sm)/r(Ru)$ to decrease and cause samarium and ruthenium to behave more like the higher members of the series.

The hexagonal $MgZn_2$ form of $SmRu_2$ was prepared by Cannon et al. [62] under the conditions 1230 °C and 65 kbar. The product was synthesized from the reaction of a mixture of powdered Sm:Ru in the ratio 1:2.

15.9. ROs_2 (R = La,Ce,Pr)

Both $CeOs_2$ and $LaOs_2$ exist in the cubic $MgCu_2$-type structure. Cannon et al. [63] have shown that under a pressure of 70 kbars and temperature of 1000 °C, these compounds transform to the hexagonal $MgZn_2$-type structure. These synthesis were carried out in the tetrahedral anvil apparatus and x-ray identification was based upon powder samples. Experiments confirmed that the hexagonal form of $CeOs_2$ and $LaOs_2$ could be prepared at pressure as low as 6 kbar but could not be prepared at temperature above 1100 °C at any pressure. $PrOs_2$ can be prepared in either the cubic or hexagonal forms without the aid or pressure.

16. References

[1] Abel, W. R., and Samara, G. A., Bull. Am. Phys. Soc. **15**, 266 (1970).
[2] Adams, L. H., and Davis, B. L., Am. J. Sci. **263**, 359–383 (1965).
[3] Adiatullin, R., and Fakidov, I. G., Fiz. Tverd. Tela **12**, 3152–3154 (1970).
[4] Akimoto, S., and Syono, Y., J. Geophys. Res. **74**, 1643–1659 (1969).
[5] Arnold, G. P., Wenzel, R. G., Rabideau, S. W., Nereson, N. G., and Bowman, A. L., J. Chem. Phys. **55**, 589–595 (1971).
[6] Azzaria, L. M., and Dachille, F., J. Phys. Chem. **65**, 889–890 (1961).
[7] Austin, A. E., J. Phys. Chem. Solids **30**, 1282–1285 (1969).
[8] Babb, S. E., J. Chem. Phys. **50**, 5271 (1969).
[9] Babb, S. E., J. Chem. Phys. **51**, 847–848 (1969).
[10] Baenziger, V. C., and Duax, W. L., J. Chem. Phys. **48**, 2914–2981 (1968).
[11] Baneeva, M. I., and Popova, S. V., Geokhimiya, No. 8, 1014–1016 (1969).
[12] Baneeva, M. I., and Bendeliani, N. A., Geokhimiya, No. 7, 1106–1108 (1973).
[13] Banus, M. D., Hanneman, R. E., and Kafalas, J. A., Solid State Res. **1**, 25–27 (1963).
[14] Banus, M. D., Science **147**, 732–722 (1965).
[15] Banus, M. D., and Levine, M. C., Mat. Res. Bull. **1**, 3–12 (1966).
[16] Banus, M. D., and Finn, M. C., Solid State Res. **4**, 24–26 (1966).
[17] Banus, M. D., and Finn, M. C., J. Electrochem. Soc. **116**, 91–94 (1969).
[18] Bardoll, B., and Todheide, K., High Temp. High Pressures **7**, 341–349 (1975).
[19] Bardoll, B., and Todheide, K., Berr. Bunsenges. Phys. Chem. **79**, 490–497 (1975).
[20] Bassett, W. A., and Barnett, J. D., Phys. Earth Planet. Interiors **3**, 54–60 (1970).
[21] Baun, W. L., Science **140**, 1330–1331 (1963).
[22] Bautista, R. G., and Margrave, J. L., High Temp. High Pressures **1**, 437–438 (1969).
[23] Beck, H. P., Z. Naturforsch. B: Anorg. Chem. Org. Chem. **31B**, 1548–1549 (1976).
[24] Bell, P. M., Simmons, G., and Hays, J. F., Carnegie Inst. Wash. Yearbook **64**, 141–144 (1965).
[25] Benaennaf, A., Domange, L., and Fluhaut, J., Compte Rendu **248**, 1672–1675 (1959).

[26] Bendeliani, N. A., and Vereshchagin, L. F., Dokl. Akad. Nauk SSSR **158**, 819–820 (1964).
[27] Bendeliani, N. A., Popova, S. V., and Vereshchagin, L. F., Geokhimiya, No. 5, 499–501 (1966).
[28] Bendeliani, N. A., and Vereshchagin, L. F., Dokl. Akad. Nauk SSSR **9**, 870–871 (1965).
[29] Bendeliani, N. A., Popova, S. V., and Vereshchagin, L. F., Geokhimiya, No. 6, 677–683 (1967).
[30] Bendeliani, N. A., Baneeva, M. I., and Poryukin, D. S., Geokhimiya, No. 7, 871–873 (1972).
[31] Bilitz, W., Z. Electrochem. **17**, 668 (1911).
[32] Bither, T. A., Prewitt, C. T., Gillson, J. L., Gierstedt, P. E., Flippen, R. B., and Young, H. S., Solid State Commun. **4**, 533–535 (1966).
[33] Bither, T. A., Bouchard, R. J., Cloud, W. H., Donohue, P. C., and Siemons, W. J., Inorg. Chem. **7**, 2208 (1968).
[34] Bither, T. A., Donohue, P. C., Cloud, W. H., Gierstedt, P. E., and Young, H. S., Solid State Chem. **1**, 526–533 (1970).
[35] Bither, T. A., Donohue, P. C., and Young, H. S., J. Solid State Chem. **3**, 300–307 (1971).
[36] Block, S., Weir, C. W., and Piermarini, G. J., Science **148**, 947–948 (1965).
[37] Bocquillon, G., Susse, C., and Vodar, B., Rev. Int. High Temp. Refract. **5**, 247–251 (1968).
[38] Bocquillon, G., and Susse, C., Rev. Int. High Temp. Refract. **6**, 263–266 (1969).
[39] Bodnar, R. E., and Steinfink, H., Inorg. Chem. **6**, 327–330 (1967).
[40] Boganov, A. G., Makarov, L. P., and Rudenko, V. S., Dokl. Akad. Nauk SSSR **16**, 332–335 (1965).
[41] Bohler, R., and Arndt, J., Contrib. Mineral. Petrol. **48**, 149–152 (1974).
[42] Boiko, L. G., and Popova, S. V., Pis'ma Zh. Eksp. Teor. Fiz., 12, 101 (1970); English Trans; JETP Lett. **12**, 70 (1970).
[43] Boldrini, P., and Loopstra, B. O., Acta Crystallogr. **22**, 744–745 (1967).
[44] Boyd, F. R., and England, J. L., J. Geophys. Res. **65**, 749–756 (1960).
[45] Brasch, J. W., Melveger, A. J., and Lippincott, E. R., Chem. Phys. Lett. **2**, 99–100 (1968).
[46] Bredig, M. A., J. Am. Ceram. Soc. **43**, 493 (1960).
[47] Bridgman, P. W., Proc. Am. Acad. Arts Sci. **47**, 441–558 (1911).
[48] Bridgman, P. W., Proc. Am. Acad. Arts Sci. **51**, 55–124 (1915).
[49] Bridgman, P. W., J. Chem. Phys. **3**, 597–05 (1935).
[50] Bridgman, P. W., J. Chem. Phys. **5**, 946–966 (1937).
[51] Bridgman, P. W., Proc. Nat. Acad. Sci. **23**, 202–205 (1937).
[52] Bridgman, P. W., Proc. Am. Arts Scie. **72**, 45–136 (1937).
[53] Bridgman, P. W., Proc. Am. Acad. Arts Sci. **74**, 399–424 (1942).
[54] Bridgman, P. W., Proc. Am. Acad. Arts Sci. **81**, 167–251 (1952).
[55] Brixner, L. H., and Ferretti, A., J. Solid State Chem. **18**, 111–116 (1976).
[56] Brown, A. J., and Whalley, E., J. Chem. Phys. **45**, 4360–4361 (1966).
[57] Brown, A. J., and Whalley, E., Inorg. Chem. **7**, 125–1255 (1968).
[58] Butcher, E. G., Alsop, M., Weston, J. A., and Gebbie, H. A., Nature **199**, 756–58 (1963).
[59] Butcher, E. G., Weston, J. A., and Gebbie, H. A., J. Chem. Phys. **41**, 2554–2555 (1964).
[60] Cannon, J. F., and Hall, H. T., Inorg. Chem. **9**, 1639–1643 (1970).
[61] Cannon, J. F., Robertson, D. L., and Hall, H. T., Mat. Res. Bull. **7**, 5–12 (1972).
[62] Cannon, J. F., Robertson, D. L., and Hall, H. T., J. Less-Common Metals **29**, 141–146 (1972).
[63] Cannon, J. F., Robertson, D. L., and Hall, H. T., J. Less-Common Metals **31**, 174–176 (1973).
[64] Cannon, J. F., J. Phys. Chem. Ref. Data **3**, 781–824 (1974).
[65] Cannon, J. F., Cannon, D. M., and Hall, H. T., J. Less-Common Metals **56**, 83–90 (1970).
[66] Cannon, J. F., Private Communication (1978).
[67] Cannon, P., and Conlin, E. T., Science **145**, 487–489 (1964).
[68] Cervinka, L., and Hruby, A., Acta Crystallogr. **B26**, 457–458 (1970).
[69] Chamberland, B. L., Mat. Res. Bull. **2**, 827–835 (1967).
[70] Chao, E. C. T., Shoemaker, E. M., and Madsen, B. M., Science **132**, 220–222 (1960).
[71] Chao, E. C. T., Fahey, J. J., and Littler, J., J. Geophys. Res., 419–421 (1962).
[72] Chou, C. L., and Plushken, Z. G., Kristallographiya, No. 7, 66–71 (1962).
[73] Chenavas, J., Capponi, J. J., Joubert, J. C., and Marezio, M., J. Solid State Chem. **6**, 1–15 (1973).
[74] Christensen, A. N., Gronbaek, R., and Rasmussen, S. E., Acta Chem. Scand. **18**, 1261–1266 (1964).
[75] Christensen, A. N., Mat. Res. Bull. **6**, 691–698 (1971).
[76] Clark, J. B., and Rapoport, E., J. Phys. Chem. Solids **31**, 247–254 (1970).
[77] Clark, J. B., and Pistorius, C. W. F. T., High Temp. High Pressures **5**, 319–326 (1973).
[78] Clausius, K., and Weigand, K., Z. Phys. Chem. (Leipzig) **B46**, 1 (1940).
[79] Clendenen, R. L., and Drickamer, H. G., J. Chem. Phys. **44**, 4223–3228 (1966).
[80] Coes, L., Science **118**, 131–132 (1953).
[81] Cohen, L. H., and Klemnt, W., J. Geophys. Res. **72**, 4245–4251 (1967).
[82] Conn, J. B., and Taylor, R. C., J. Electrochem. Soc. **107**, 977–982 (1960).
[83] Cromer, D. T., and Herrington, K., J. Am. Chem. Soc. **77**, 4708–4709 (1955).
[84] Curtis, C. E., Doney, L. M., and Johnson, J. R., J. Am. Ceram. Soc. **37**, No. 10 (1954).
[85] Dachille, F., and Roy, R., Z. Krist. **111**, 452–461 (1959).
[86] Dachille, F., Simons, P. Y., and Roy, R., Am. Mineral. **53**, 1929–1939 (1968).
[87] Dachille, F., Simons, P. Y., and Roy, R., Am. Mineral. **54**, 1482 (1969).
[88] Darnell, A. J., and McCollum, W. A., J. Chem. Phys. **55**, 116–122 (1971).
[89] Dandekar, D. P., and Jamieson, J. C., Trans. Am. Cryst. Assoc. **5**, 19–27 (1969).
[90] Decker, D. L., J. Appl. Phys. **42**, 3239–3244 (1971).
[91] Decker, D. L., Bassett, W. A., Merrill, L., Hall, H. T., and Barnett, J. D., J. Phys. Chem. Ref. Data **1**, 773–836 (1972).
[92] Deer, W. A., Howie, R. A., and Zussman, J., An Introduction to Rock Forming Minerals, 528 pp., J. Wiley, New York, 1966 (p. 341).
[92a] Donohue, P. C., Bither, T. A., Cloud, W. H., and Grederick, C. G., Mat. Res. Bull. **6**, 231–238 (1971).
[93] Donohue, P. C., Mat. Res. Bull. **7**, 943–948 (1972).
[94] Donohue, P. C., Siemons, W. J., and Gillson, J. L., J. Phys. Chem. Solids **29**, 807–813 (1968).
[95] Donnay, J. D. H., and Ondik, H. M., Crystall Determiniative Tables, third Edition, Vol. II, Inorg. Compounds, Published Jointly by U.S. Department of Commerce, NBS, and joint Committee on Powder Diffraction Standards (1973).
[95a] Dyuzheva, T. I., Kabalkina, S. S., and Vereshchagin, L. F., Kristallografiya **17**, 804–811 (1972).
[96] Eatough, N. L., and Hall, H. T., Inorg. Chem. **8**, 1439–1445 (1969).
[97] Eatough, N. L., and Hall, H. T., Inorg. Chem. **9**, 416–471 (1970).
[97a] Eatough, N. L., and Hall, H. T., Inorg. Chem. **11**, 2608–2609 (1972).
[98] Eliseev, A. A., and Kuznetsov, V. G., Izv. Akad. Nauk SSSR, Neorg. Mater. **2**, 1157 (1966).
[99] Eliseev, A. A., Kyz'micheva, G. M., Evdokimova, V. V., and Novokshonov, V. I., Zh. Neorg. Khim. **2**, 2900–2903 (1976).
[99a] Elliot, R. P., Proc. Conf. Rare Earth Res. **4**, 215–245 (1964).
[100] Evers, J., Oehlinger, G., and Weiss, A., Angew. Chem. Int. Ed. Engl. **16**, 659–666 (1977).
[101] Evers, J., Oehlinger, G., and Weiss, A., J. Solid State Chem. **20**, 173–181 (1977).
[102] Evers, J., Oehlinger, G., and Weiss, A., Z. Naturforsch., B: Anorg. Chem., Org. Chem. **32B**, 1352–1353 (1977).
[103] Fenner, C. N., Am. J. Sci. **186**, 331–384 (1913).
[104] Fluhaut, J., Guittard, M., and Patrie, M., Bull. Soc. Chim. France, No. 302, 1917–1922 (1959).
[105] Frindt, R. F., Murray, R. B., Pitts, G. D., and Yoffee, A. D., J. Phys. C: Solid State Phys. **5**, L154–L156 (1972).
[106] Fritz, I. J., and Peercy, P. S., Solid State Commun. **16**, 197–1200 (1975).
[107] Gattow, G., and Schneider, A., Z. Znorg. Chem. **286**, 296 (1956).
[108] German, V. N., Podrets, M. A., Trunin, R. F., Zh. Eksp. Teor. Fiz. **64**, 205–206 (1973).
[109] German, V. N., Orlova, N. N., Tarasova, L. A., Trunin, R. F., Izv. Akad. Nauk SSSR, Phys. Solid Earth **11**, 431–434 (1975).
[110] German, V. N., Orlova, N. N., Pavlovskii, M. N., Tarasova, L. A., and Trunin, R. F., Izv. Akad. Nauk SSSR, Phys. Solid Earth **11**, 487–490 (1975).
[111] Gibson, R. E., J. Phys. Chem. **32**, 1197–1205 (1928).
[112] Giauque, W. F., and Blue, R. W., J. Am. Chem. Soc. **58**, 831–837 (1936).
[113] Grazhdankina, N. P., and Rodinov, K. P., Zh. Eksp. Teor. Fiz. **43**, 2024–2027 (1963).

[114] Griggs, D. T., and Kennedy, G. C., Am. J. Sci. **254**, 722–735 (1956).
[115] Hahn, H., and Klinger, W., Naturwissenschaften **52**, 494 (1965).
[116] Hanneman, R. E., and Strong, H. M., J. Appl. Phys. **36**, 523–528 (1965).
[117] Hanneman, R. E., and Strong, H. M., J. Appl. Phys. **37**, 612–614 (1966).
[118] Holm, J. L., Kleppa, O. J., and Westrum, E. F., Geochim. Cosmochim. Acta **31**, 2289–2307 (1967).
[119] Holzapfel, W. B., High Temp. High Pressures **1**, 675–677 (1969).
[120] Hulliger, F., Nature **201**, 381–382 (1964).
[121] Hulliger, F., Nature **204**, 644–646 (1964).
[122] Ida, Y., Syono, Y., and Akimoto, S., Earth Planet. Sci. Lett. **3**, 216–218 (1967).
[123] Jamieson, J. C., and Olinger, B., Science **161**, 893–895 (1968).
[124] Jamieson, J. C., and Olinger, B., Am. Mineral. **54**, 1477–1481 (1969).
[125] Jamieson, J. C., and Wu, A. Y., J. Appl. Phys. **48**, 4573–4575 (1977).
[126] Jetischko, W., and Johnson, V., Acta Crystallogr. **B28**, 1971–1973 (1972).
[126a] Jeitschko, W., Donohue, P. C., and Johnson, V., Acta Crystallogr. **B32**, 1499–1505 (1976).
[127] Johnson, Q, Inorg. Chem. **10**, 2089–2090 (1971).
[128] Justi, E., and Nitka, H., Physik. Z. **37**, 435–438 (1936).
[129] Kabalkina, S. S., and Popova, S. V., Dokl. Akad. Nauk SSSR **153**, 1310–1312 (1963).
[130] Kabalkina, S. S., Popova, S. V., Serebryananya, N. R., and Vereschchagin, L. F., Soviet Phys. Kokl. **8**, 972–974 (1963).
[131] Kabalkina, S. S., Vereshchagin, L. F., and Lityagina, L. M., Soviet Phys. Dokl. **12**, 946–949 (1968).
[132] Kabalkina, S. S., Vereshchagin, L. F., and Lityagina, L. M., Soviet Phys. Solid State **11**, 847–848 (1969).
[133] Kabalkina, S. S., Vereshchagin, L. F., and Lityagina, L. M., Soviet Phys. JETP **29**, 803–806 (1969).
[134] Kafalas, A. A., and Finn, M. C., Solid State Res. **3**, 26 (1963).
[135] Kalliomaki, M. S., and Meisalo, V. P. J., Paper presented at the 12th Annual Meeting of the European High Pressure Group Morburg/Lahn (1974).
[136] Kamb, B., Science **150**, 205–209 (1965).
[137] Kamb, B., and Prakash, A., Acta Crystallogr. **B24**, 1317–1326 (1968).
[138] Kamb, B., Am. Cryst. Assoc., Bull. **5**, 61 (1969).
[139] Kawada, I., Kato, K., and Yamaoka, S., Acta Crystallogr. **B32**, 3110–3111 (1976).
[140] Kawai, N., Mishima, O., Togaya, M., and LeNeindre, B., Proc. Japan Academy **51**, 627–629 (1975).
[141] Kawai, N., Mishima, O., Togaya, M., and LeNeindre, B., Proc. Japan Academy **51**, 627–629 (1975).
[142] Kelley, K. K., Bureau of Mines Bull., No. 584 (1960).
[143] Kennedy, G. C., and LaMori, P. N., J. Geophys. Res. **67**, 851–856 (1962).
[144] Kessler, J. R., Monberg, E., and Nicol, M., J. Chem. Phys. **60**, 5057–5065 (1974).
[145] Kitahara, S., and Kennedy, G. C., J. Geophys. Res. **69**, 5395–5400 (1964).
[146] Kodaira, K., Iwasaki, Y., and Matsushita, T., J. Am. Ceram. Soc. **59**, 183–184 (1976).
[147] Konig, H., Z. Krist. **105**, 297 (1943).
[148] Korenstein, R., Henry, R. L., and Wold, A., Inorg. Chem. **15**, 3031–3034 (1976).
[149] Kripka, M. C., Krikorian, N. H., and Wallace, T. C., Paper presented at Seventh Rare Earth Res. Conf. (1968).
[150] Kulcinski, G. L., J. Am. Ceram. Soc. **51**, 582–584 (1968).
[151] Larchev, V. I., and Popova, S. V., Neorg. Mater. **13**, 419–422 (1977).
[152] Lehman, M. S., F. K., Pulsen, F. R., Christensen, A. N., and Rasmussen, S. E., Acta Chem. Scand. **24**, 1662–1670 (1970).
[153] Lihl, F., Sci. Rept. #7, Contr. No. F-61(052)-609, AD614462 38 p. (1964)
[154] Linde, R. K., and DeCarli, P. S., J. Chem. Phys. **50**, 319–325 (1969).
[155] Liu, L. G., Phys. Earth. Planet. Inter. **9**, 338–343 (1974).
[156] Liu, L. G., Phys. Earth. Planet. Inter. **10**, 168–176 (1975).
[157] Liu, L. G., Phys. Earth. Planet. Inter. **10**, 344–347 (1975).
[158] Liu, L. G., Earth Planet. Sci. Lett. **29**, 104–106 (1976).
[159] Liu, L. G., Science **199**, 422–425 (1978).
[160] Liu, L. G., Bassett, W. A., and Sharry, J., J. Geophys. Res., **83**, 2301–2305 (1978).
[161] Lynch, C. T., Vahldiek, F. W., and Robinson, L. B., J. Am. Ceram. Soc. **44**, 147–148 (1961).
[162] Lutz, H. D., Z. Anorg. Allgem. Chem. **339**, 308–312 (1965).
[163] Lutz, H. D., Z. Anorg. Allgem. Chem. **342**, 151–155 (1966).
[164] MacDonald, G. J. F., Am. J. Sci. **254**, 713–721 (1956).
[165] Mahajan, V. K., Chang, P. T., and Margrasve, J. L., High Temp. High Pressures **7**, 326–329 (1975).
[166] Marcon, J. A., and Pascard, R., Compt. Red. **C266**, 270 (1968).
[167] McCarron, E., Korenstein, R., and Wold, A., Mat. Res. Bull. **11**, 1457–1462 (1976).
[168] McQueen, R. G., Jamieson, J. C., and Marsh, S. P., Science **155**, 1401–1404 (1967).
[169] McWhan, D. B., Jamieson, J. C., Silverman, M. S., and Soulen, J. R., J. Less-Common Metals **12**, 75–76 (1967).
[170] McWhan, D. B., Birgeneau, R. J., Bonner, W. A., Taub, H., and Axe, J. D., J. Phys. C: Solid State Phys. **8**, L81–L85 (1975).
[171] Meisalo, V., and Kalliomaki, M., High Temp. High Pressures **7**, 419–423 (1975).
[172] Merrill, L., J. Phys. Chem. Ref. Data **6**, 1205–1252 (1977).
[173] Miller, H., Monatsch. Chem. **103**, 110–115 (1972).
[174] Minomura, S., and Drickamer, H. G., J. Chem. Phys. **34**, 670–671 (1961).
[175] Minomura, S., and Okai, B., Am. Soc. Mech. Engr., Publ. 64 WA/PT-6 (1964).
[176] Mirwald, P. W., Contrib. Mineral. Petrol. **59**, 33–40 (1976).
[176a] Moller, H. S., Z. Phys. **212**, 107–121 (1968).
[177] Mossman, M. A., and Pitzer, K. S., Am. Chem. Soc. J. **63**, 2348–2356 (1941).
[178] Mumpton, F. A., and Roy, R., J. Am. Ceram. Soc. **43**, 234, 240 (1960).
[178a] Minson, R. A., Inorg. Chem. **5**, 1296 (1966).
[179] Munson, R. A., Inorg. Chem. **7**, 389 (1968).
[180] Munson, R. A., and Kasper, J. S., Inorg. Chem. **8**, 1198–1199 (1969).
[181] Nagel, L., and O'Keefe, M., Mat. Res. Bull. **6**, 1317–1320 (1971).
[182] Naka, S., Ito, S., and Inagaki, M., J. Am. Ceram. Soc. **55**, 323–324 (1972).
[183a] Olcese, G. L., Atti Accad. Nazl. Lincei, Rend., Classe Sci. Fis., Matt. Nat. **40**. 629–634 (1966).
[184] Osborn, E. F., J. Am. Ceram. Soc. **36**, 5 (1953).
[185] Ostrovskii, I. A., Izv. Akad. Nauk SSSR, Ser. Geol. **10**, 132–135 (1965).
[186] Ostrovskii, I. A., Geol. J. **5**, 321–328 (1967).
[187] Osugi, J., Murikawa, R., and Tanaka, Y., Nippon, Kagaku Zasshi **87**, 1169–1173 (1966).
[188] Osugi, J., Namikawa, R., and Tanaka, Y., Rev. Phys. Chem. Jpn. **37**, 81–93 (1967).
[189] Osugi, J., and Tanaka, Y., Nippon Kagaku Zasshi **90**, 618–625 (1969).
[189a] Oswald, H. R., Helv. Chem. Acta **43**, 77–88 (1960).
[190] Peercy, P. S., and Fritz, I. J., Phys. Rev. Lett. **32**, 466–469 (1974).
[191] Peercy, P. S., Fritz, I. J., and Samara, G. A., J. Phys. Chem. Solids **36**, 1105–1122 (1975).
[191a] Pistorius, C. W. F. T., Z. Phys. Chem. Neue Folge **31**, 155–160 (1962).
[192] Pistorius, C. W. F. T., Pistorius, M. C., Blakey, J. P., and Admiraal, L. J., J. Chem. Phys. **38**, 600–602 (1963).
[193] Pistorius, C. W. F. T., Rapoport, E., and Clark, J. B., J. Chem. Phys. **48**, 5509–5514 (1968).
[194] Pistorius, C. W. F. T., and Clark, J. B., High Temp. High Pressures **7**, 561–570 (1969).
[195] Pistorius, C. W. F. T., J. Less-Common Metals **31**, 119–124 (1973).
[196] Porta, P., Marezio, M., Remeika, J. P., and Dermier, P. D., Mat. Res. Bull. **7**, 157–162 (1972).
[197] Preisinger, A., Naturwissenschaften **49**, 345–346 (1962).
[198] Prewitt, C. T., and Young, H. S., Science **149**, 535–537 (1965).
[199] Ramsdell, L. S., Am. Mineral. **40**, 975–982 (1955).
[200] Range, K. J., Engert, G., and Weiss, A., Z. Naturforsch. **B25**, 1187 (1970).
[201] Richter, P. W., Pistorius, C. W. F. T., J. Solid State Chem. **3**, 197–205 (1971).
[202] Ring, S., Tecotzky, M., Inorg. Chem. **3**, 182–185 (1964).
[203] Ringwood, A. E., and Seabrook, M., Nature **196**, 883–884 (1962).
[204] Robertson, D. L., Cannon, J. F., and Hall, H. T., Mat. Res. Bull., **7**, 977–982 (1972).
[204a] Ross, R. G., Andersson, P., and Backstrom, G., High Temp. High Pressures **9**, 87–96 (1977).
[205] Roy, D. M., and Mumpton, F. A., Econ. Geol. **51**, 432–443 (1956).
[206] Roy, R., Majumdar, A. J., and Hulbe, C. W., Econ. Geol. **54**, 1278–1280 (1959).

[208] Roy, R., and Frushour, R. H., J. Am. Ceram. Soc. **54**, 589–590 (1971).
[209] Ruff, O., Ebert, F., and Woitineck, H., Z. Anorg. Allgem. Chem. **180**, 252–256 (1929).
[210] Ring, S. A., and Tecotzky, M. Inorg. Chem. **3**, 182–185 (1964).
[211] Sahl, V. K., Acta Crystallogr. **19**, 1027–1030 (1965).
[212] Samara, G. A., Phys. Rev. B **2**, 4194–4198 (1970).
[213] Samara, G. A., Phys. Rev. B **13**, 4529–4544 (1976).
[214] Sarver, J. F., and Hummel, F. A., J. Am. Ceram. Soc. **43**, 336 (1960).
[215] Sawamoto, H., Proc. Annual Fall Mtg. of Japan Seismological Soc. **2**, 108 (1976).
[216] Schmidt, E. D. D., and Vedam, K., J. Phys. Chem. Solids **27**, 1563–1566 (1966).
[217] Sclar, C. B., and Carrison, L. C., Am. Mineral **47**, 1292–1301 (1962).
[218] Sclar, C. B., Young, A. P., Carrison, L. C., and Schwarrz, C. M., J. Geophys. Res. **67**, 4049–4054 (1962).
[219] Seifert, K. F., Fortschr. Mineral. **45**, 214–280 (1968).
[220] Seifert, K. F., and Kirfel, Z., Acta, Crystallogr. **A25**, 53 (1969).
[221] Senko, M. E., Dunn, H. M., Weidenborner, J., and Cole, H., Acta Crystallogr. **12**, 76 (1959).
[222] Serebryanaya, N. R., Geokhimiya, No. 7, 866 (1966).
[223] Shannon, R. D., Solid State Commun. **6**, 139–143 (1968).
[224] Shannon, R. D., Solid State Commun. **7**, 257 (1969).
[225] Sharma, S. K., and Malhotsa, G. L., Phys. Lett. **9**, 218–219 (1964).
[226] Silverman, M. S., and Soulen, J. R., J. Chem. Phys. **38**, 2584 (1963).
[227] Silverman, M. S., and Soulen, J. R., J. Phys. Chem. **67**, 1919 (1963).
[228] Silverman, M. S., Inorg. Chem. **3**, 1041 (1964).
[229] Silverman, M. S., Inorg. Chem. **4**, 587 (1965).
[230] Silverman, M. S., and Soulen, J. R., Inorg. Chem. **4**, 129–130 (1965).
[231] Silverman, M. S., Tech. Tept. No. 51, Office of Naval Research, Contract Nomr. 2687 (1966).
[232] Simons, P. Y., and Dachille, F., Am. Mineral. **55**, 403–415 (1970).
[233] Simons, P. Y., and Dachille, F., Acta Crystallogr. **23**, 334–336 (1967).
[234] Skelton, E. F., Feldman, J. L., Liu, C. Y., and Spain, I. I., Phys. Rev. **B13**, 2605–2613 (1976).
[235] Smith, D. K., and Cline, C. F., J. Am. Ceram. Soc. **45**, 249 (1962).
[236] Smith, H. I., and Chen, J. H., Bull. Am. Phys. Soc. **11**, 44 (1966).
[237] Spedding, F. H., Geschneidner, K., and Daane, A. H., J. Am. Chem. Soc. **80**, 4499–4503 (1958).
[238] Spedding, F. H., Geschneidner, K. and Daane, A. H., Trans. AIME **215**, 192–199 (1959).
[239] Stevenson, R., J. Chem. Phys. **27**, 673 (1957).
[240] Stevenson, R., J. Chem. Phys. **27**, 147–150 (1957).
[241] Stewart, J. W., J. Chem. Phys. **33**, 128–133 (1960).
[242] Stishov, S. M., Popova, S. V., Geokhimiya, No. 10, 837–839 (1961).
[243] Stishov, S. M., and Belov, N. V., Dokl. Akad. Nauk SSSR **143**, 951–954 (1962).
[244] Stishov, S. M., Dokl. Akad. Nauk. SSSR **148**, 1186–1188 (1963).
[245] Stoffler, D., and Arndt, J., Naturwissenschaften **56**, 100–109 (1969).
[246] Storm, A. R., Wernick, J. H., and Jayaraman, A., J. Phys. Chem. Solids. **27**, 1227–1232 (1966).
[247] Strong, H. M., and Hanneman, R. E., J. Chem. Phys. **46**, 3668–3676(1967).
[248] Suito, K., and Kawai, N., Mat. Res. Bull. **10**, 677–680 (1975).
[249] Syono, Y., and Akimoto, S., Mat. Res. Bull. **3**, 153–158 (1968).
[250] Takahashi, T., High Pressure Measurement, A. A. Giardini, E. C. Lloyd, Ed., pp. 240–244, Butterworths, Washington, D.C., (1963).
[251] Tammann, G., Ann. Phys. **2**, 1 (1900).
[252] Tonkov, E. D., and Tikhomirova, N. A., Soviet Phys. Crystallography **15**, 945–946 (1971).
[253] Towle, L. C., Oberbeck, V., Brown, B. E., and Stajdohar, R. E., Science **154**, 895–896 (1966).
[254] Tuttle, O. F., and Bowen, N. L., Geol. Soc. Am. Memoir **74**, 28–31 (1958).
[255] Vahldiek, F. W., Robinson, L. B., and Lynch, C. T., Science **142**, 1059–1060 (1963).
[256] Vereshchagin, L. F., Kabalkina, S. S., and Kotilevets, A. A., Soviet Phys. JETP **22**, 1181–1184 (1966).
[257] Vettier, C., and Yelon, W. B., J. Phys. Chem. Solids. **36**, 401–405 (1975).
[258] Vogel, R., and Klose, K., Z. Metallk **45**, 633 (1954).
[259] Walters, L. S., Science **147**, 1029–1032 (1965).
[260] Wang, R., Steinfink, H., Inorg. Chem. **6**, 1685–1692 (1967).
[261] Webb, A. W., and Hall, H. T., Inorg. Chem. **9**, 843–847 (1970).
[262] Webb, A. W., and Hall, H. T., Inorg. Chem. **9**, 1084–1090 (1970).
[263] Weir, C. E., Piermarini, G. J., and Block, S., J. Chem. Phys. **50**, 2089–2093 (1969).
[264] Wentorf, R. H., J. Geophys. Res. **9**, 3648 (1962).
[264a] Wernick, J. H., and Geller, S., Trans. Am. Inst. Mining, Metall. Petrol. Engr. **218**, 866–868 (1960).
[265] Whalley, E., and Davidson, D. W., J. Chem. Phys. **43**, 2148–2149 (1965).
[266] Whalley, E., Can. J. Chem. **38**, 2105–2108 (1960).
[267] Whalley, E., Davidson, E. W., and Health, F. B. R., J. Chem. Phys. **45**, 3976–3982 (1966).
[268] Whalley, E., Developments in Appl. Spectrosc. **6**, 277–296 (1967).
[269] Whalley, E., Proc. 3rd Int. Symposium, Physics of Ice, 19–43 (1968).
[270] White, W. B., Bachille, F., and Roy, R., J. Am. Ceram. Soc. **44**, 170–174 (1961).
[271] Whitney, E. D., J. Am. Ceram. Soc. **45**, 612–613 (1962).
[272] Worlton, T. G., and Beyerlein, R. A., Phys. Rev. B **12**, 1899–1907 (1975).
[273] Wyckoff, R. W. G., Crystal Structures, 2nd Ed., Vol. , 469 pp., Interscience, New York (1963).
[274] Yagi, T., and Akimoto S., Tectonophysics **35**, 259–270 (1976).
[275] Yoder, H. S., Trans. Am. Geophys. Union **31**, 827–835 (1950).
[276] Zahner, J. C., and Drickamer, H. G., J. Phys. Chem. Solids **11**, 92–96 (1959).
[277] Zaslovskii, A. I., Kondrashov, Y. D., and Tolkachov, S. S., Dokl. Akad. Nauk SSSR **72**, 559 (1950).
[278] Zoltai, T., and Buerger, M. J., Z. Kristallogr. Ed. **111**, 130–141 (1959).